

## Advances in Conjugated Microporous Polymers

Jet-Sing M. Lee and Andrew I. Cooper\*

Cite This: *Chem. Rev.* 2020, 120, 2171–2214

Read Online

ACCESS |



Metrics &amp; More



Article Recommendations



Supporting Information

**ABSTRACT:** Conjugated microporous polymers (CMPs) are a unique class of materials that combine extended  $\pi$ -conjugation with a permanently microporous skeleton. Since their discovery in 2007, CMPs have become established as an important subclass of porous materials. A wide range of synthetic building blocks and network-forming reactions offers an enormous variety of CMPs with different properties and structures. This has allowed CMPs to be developed for gas adsorption and separations, chemical adsorption and encapsulation, heterogeneous catalysis, photoredox catalysis, light emittance, sensing, energy storage, biological applications, and solar fuels production. Here we review the progress of CMP research since its beginnings and offer an outlook for where these materials might be headed in the future. We also compare the prospect for CMPs against the growing range of conjugated crystalline covalent organic frameworks (COFs).



## CONTENTS

1. Introduction	2171	3.8.1. Biosensing	2192
1.1. Historical Development and Selected Advances	2173	3.8.2. Drug Delivery and Bioimaging	2193
2. Design and Synthesis Routes	2176	3.8.3. Singlet Oxygen Production	2193
2.1. Sonogashira-Hagihara Coupling	2176	3.8.4. Antibacterial Materials	2193
2.2. Suzuki-Miyaura Coupling	2176	3.8.5. Phototherapy	2193
2.3. Yamamoto Coupling	2176	3.9. Photocatalytic Hydrogen Evolution	2194
2.4. Heck Coupling	2177	4. Outlooks and Conclusion	2205
2.5. Cyclotrimerization Reactions	2177	4.1. Photoorganocatalysis/Organocatalysis	2206
2.6. Phenazine Ring Fusion	2177	4.2. Heterojunction Semiconductor Composites	2206
2.7. Schiff-Base Condensations	2177	4.3. Batteries and Energy Storage	2206
2.8. Heterocycle Linkages	2177	4.4. CMP Biohybrids	2207
2.9. Alkyne Metathesis	2177	Associated Content	2207
2.10. Oxidative Coupling	2177	Supporting Information	2207
2.11. Buchwald-Hartwig Amination	2177	Author Information	2207
2.12. Electropolymerization	2177	Corresponding Author	2207
2.13. Hypercrosslinking Linear Conjugated Polymers	2178	Author	2207
2.14. Synthesis Parameters Affecting Functionality	2178	Notes	2207
2.15. Unconventional Synthesis Methods and Composites	2178	Biographies	2207
3. Applications of CMPs	2179	Acknowledgments	2207
3.1. Gas Storage and Separation	2179	References	2207
3.2. Adsorption and Encapsulation of Chemicals	2180		
3.3. Heterogeneous Catalysis	2180		
3.4. Photoredox Catalysis	2181		
3.5. Light Emittance	2183		
3.6. Chemosensors	2185		
3.7. Energy Storage	2187		
3.7.1. Supercapacitors	2187		
3.7.2. Batteries	2190		
3.8. Biological Applications	2192		

## 1. INTRODUCTION

Porosity an old concept: it has existed in nature for millennia in structures such as rock, biological tissues, and charcoal. The word “porous” is typically used to describe a material that possesses permanent voids that may be interconnected and are permeable to liquids or gases; that is, it usually has a practical

Received: July 11, 2019

Published: January 28, 2020

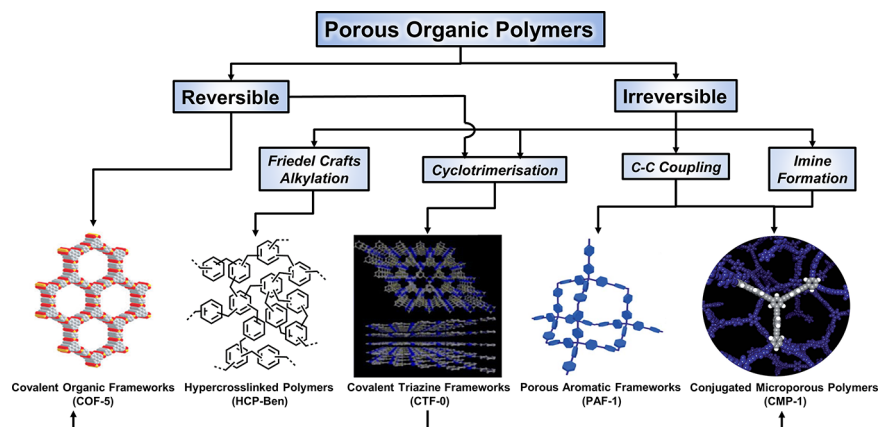


**Figure 1.** Types of porous organic polymer frameworks and their coupling chemistries. Porous polymers from left to right: covalent organic frameworks (COFs),<sup>12</sup> hypercrosslinked polymers (HCPs),<sup>28</sup> covalent triazine frameworks (CTFs),<sup>21</sup> porous aromatic frameworks (PAFs),<sup>24</sup> and conjugated microporous polymers (CMPs).<sup>25</sup> Note that these classifications can overlap somewhat; for example, some COFs are also conjugated, and not all COFs reported are particularly crystalline.

connotation. In modern times, porous materials are important in many fields of science and technology and there has been an explosion in the number of new advanced porous functional materials over the last 20 years. The International Union of Pure and Applied Chemistry (IUPAC) classified porous materials into three types based on the diameter ( $d$ ) of their pore sizes: microporous ( $d < 2$  nm), mesoporous ( $2$  nm  $< d < 50$  nm), and macroporous ( $d > 50$  nm).<sup>1</sup> Many different synthetic porous materials have been produced. Zeolites are inorganic porous frameworks that are a staple product in society, having a large global market with uses that range from detergents to the removal of radioactive particles from nuclear waste. Another class of inorganic-containing porous solids are hybrid metal–organic frameworks (MOFs, also known as porous coordination polymers, PCPs).<sup>2–5</sup> MOFs are extended, typically crystalline frameworks constructed with metal ions or clusters that provide directional bonding to the organic ligand through the preferential geometry and coordination number of the metal, forming voids within the structure giving rise to porosity.

Zeolites and MOFs both incorporate metals, but there is also a range of purely organic porous materials. In porous MOFs, metal ions coordinated to organic linkers, which are usually aromatic, imparts both rigidity and directionality. Porous organic materials also tend to be rigid and the bonding somewhat directional in order to prevent collapse of the porous structure. This can be achieved by careful choice of the molecular building blocks. Not all porous materials need to be extended networks. For example, porous organic cages (POCs) are discrete porous molecules where the molecular cage is synthesized first and then assembled in the solid state in a separate step.<sup>6–8</sup> POCs are a unique class of solution-processable molecular materials where porosity arises via interconnection of intrinsic cavities, which can be modified by changing the solid state packing of the cage molecules. Polymers of intrinsic microporosity (PIMs) are a rare example of porosity in a one-dimensional polymer, achieved through inefficient packing of the twisted polymer backbone.<sup>9–11</sup>

A wide range of porous organic polymer networks have been introduced in the past two decades (Figure 1), such as crystalline covalent organic frameworks (COFs)<sup>12–14</sup> and various amorphous networks, such as hypercrosslinked polymers (HCPs),<sup>15–18</sup> covalent triazine frameworks

(CTFs),<sup>19–21</sup> porous aromatic frameworks (PAFs),<sup>22–24</sup> and conjugated microporous polymers (CMPs).<sup>25–27</sup> Each subclass of material generally favors particular network formation reactions. Except for COFs and a small number of CTFs, which are synthesized under thermodynamic control, the other porous polymer networks are usually amorphous, disordered materials. While these various materials are structurally different, they are united by their high porosity, their lightweight elements, and their strong, covalently bonded 2- or 3D structures.

When first discovered, CMPs were unique among porous materials because they possessed extended  $\pi$ -conjugation throughout the porous 3D network. PAFs,<sup>22–24</sup> which are closely related to CMPs and formed using similar coupling chemistries, do not possess extended  $\pi$ -conjugation because they are linked by tetrahedral tetraphenylmethane nodes. Porous polymer networks (PPNs) is another term used to describe PAFs;<sup>29</sup> they are essentially the same materials. Element-organic frameworks (EOFs) are silane-containing analogues of PAFs and are formed using organo-metallic coupling routes.<sup>30</sup> CTFs<sup>19–21</sup> might also be considered to be a subclass of CMPs because they are microporous and have extended  $\pi$ -conjugation, although they were developed separately and their formation chemistry was initially quite different.<sup>19</sup>

In 2007, we reported the synthesis of microporous poly(aryleneethynylene) networks; these were the first examples of what have since come to be known as CMPs.<sup>25</sup> Since their discovery, many scientists across the world have contributed to the field of CMP chemistry, leading to a strong growth in publications over the last 10 years (Figure 2). A little more than a decade after their discovery, it is now timely to reassess the standing of CMPs. In this review, we present an up-to-date overview of the field of CMPs, starting with an initial historical look at their origins and a list of selected key advances. The diverse range of synthesis routes available for CMPs is surveyed, since this is a feature that makes them a key platform for the development of new organic porous materials. We discuss the functional design of CMPs that gives access to a range of potential applications, with focus on the exploitation of optoelectronic properties for photoredox catalysis, light emittance, energy storage, biological, and photocatalytic  $H_2$  evolution. Finally, we give an outlook of where CMP research

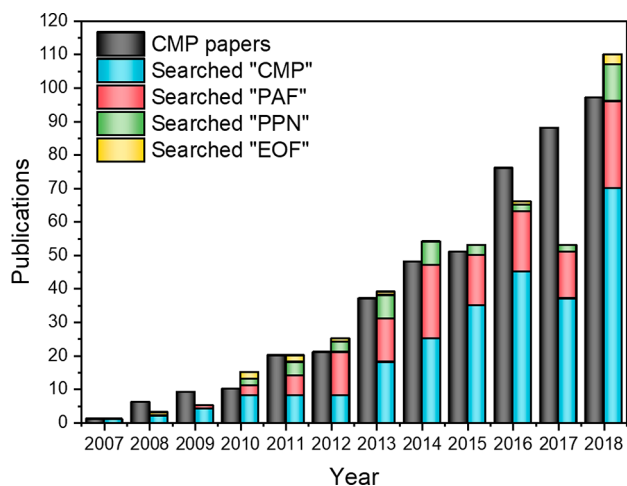


**Figure 2.** Annual publications on CMPs and related materials since their discovery (assessed 4th January 2019). “CMP papers” (black) were found by searching for CMP-specific papers that cite back to key classic CMP studies. Only papers that relate directly to CMP research are included; that is, no papers that give general background references in introduction sections, etc. Searched terms are from the title search with Web of Science, Thomson Reuters database. The full list of “CMP papers” (464 papers in total) can be found in the [Supporting Information](#), including papers that are not referred directly in this review.

might lead us in the future and draw some comparisons with conjugated COFs. Given the volume of literature (Figure 2), this review does not attempt to be exhaustive, but it is rather a personal selection of papers to illustrate the scope of the science that has been explored with these materials.

### 1.1. Historical Development and Selected Advances

Davankov et al. reported the first example of hypercrosslinked polymers<sup>31</sup> in 1969, before either of the coauthors of this review were born. These materials became industrially important with Purolite International Ltd. (UK, USA) producing them as Hypersol-Macronet, 25 years later. Hypercrosslinked polymers (HCPs) were developed initially using linear polystyrene as a precursor and using different cross-linkers such as divinylbenzene,<sup>32</sup> *p*-xylylenedichloride,<sup>33</sup> and chloromethyl methyl ether,<sup>34</sup> yielding apparent Brunauer–Emmett–Teller (BET) surface areas of up to 1106 m<sup>2</sup> g<sup>-1</sup>.<sup>35</sup> The cross-linkers react with the phenyl rings to form a network via a Friedel–Crafts alkylation reaction.<sup>36</sup> Covalent bridges formed from the cross-linker create a relatively rigid structure, which is capable of swelling but incapable of completely collapsing without inducing a great deal of strain. This strain prevents complete collapse upon solvent removal and provides permanent porosity. Recently, a HCP with a BET surface area as high as 3002 m<sup>2</sup> g<sup>-1</sup> was reported through an approach that gives layered, exfoliable materials.<sup>37</sup> An important early paper was published in 1992 by Webster et al., who reported an HCP that used similar bonding principles to later CMPs, although in that case, the conjugation between the aromatic rings was broken by a carbinol center;<sup>38</sup> in that sense, those materials were more akin to PAFs.

In 2004, McKeown and Budd reported the first PIMs.<sup>9</sup> The porous properties of these polymers are derived from their high rigidity, combined with the contorted shapes in the one-dimensional polymer backbone, which does not allow the chains to pack efficiently. The porosity of these polymers arises

from poor packing of a linear polymer chain, rather than a 3D network, and this allows PIMs to be solution processable, which is still a rare feature among porous solids.

COFs were first reported in 2005 by Yaghi et al., and they are built using reversible covalent bonds, which allows the formation of an ordered, crystalline porous framework.<sup>12</sup> COFs are effectively the covalent analogue of MOFs. There has been rapid growth in the field of COFs since their initial discovery, with a number of new synthetic routes developed to include also conjugated COFs. BET surface areas as high as 4210 m<sup>2</sup> g<sup>-1</sup> were reported for COF-103,<sup>39</sup> although this material most likely has marginal stability. Certain imine-based COFs might also be thought of as crystalline CMPs, since the imine linkages provide conjugation. Likewise, CMPs are, in a sense, amorphous analogues of COFs; this is discussed in the final section of the review.

CMPs are 3D semiconducting polymers in which rigid aromatic groups are linked together, either directly or via double or triple bonds, to afford  $\pi$ -conjugated microporous networks.<sup>26</sup> Conjugation arises from the alternation of single and double-/triple-bonds throughout the extended network, which offers useful electronic properties, as exploited in a number of applications that are described here. In almost all examples so far, covalent bonds in CMPs are formed irreversibly and the polymerization proceeds via a kinetic route; hence, all CMPs (excluding any conjugated COFs) are amorphous. The large variety of molecular building blocks that can be coupled in this way allows the control of functionality and structure in CMPs, and this structural diversity, perhaps more than anything else, has led to a rapid growth of interest in these materials since their discovery (Figure 3).

The first CMPs were reported in 2007: they were conjugated microporous poly(aryleneethynylene) networks with BET surface areas up to 834 m<sup>2</sup> g<sup>-1</sup>, formed by Sonogashira-Hagihara cross-coupling of alkynyl arene monomers with halogen-bearing aromatics.<sup>25</sup> We chose alkyne struts both to impart conjugation and because they constitute almost optimally lightweight linkers for the creation of low-density porous materials, as later adopted for MOFs.<sup>57–59</sup> In the following year, CMPs with surface areas exceeding 1000 m<sup>2</sup> g<sup>-1</sup> were produced by tuning the monomer strut length.<sup>60</sup> Homocoupling routes to CMPs were also reported in 2008, producing amorphous butadiyne containing networks,<sup>40</sup> later reported to exhibit water splitting activity.<sup>53</sup> These CMPs were found to have micro/mesoporous hybrid characteristics, as compared to the first CMPs, which were almost entirely microporous.<sup>40</sup> Also in 2008, Weber and Thomas found that poly(*p*-phenylene) CMP networks exhibited photoluminescence properties, making them potentially useful in organic light-emitting-diode (OLED) applications:<sup>41</sup> this was the first study that investigated the optoelectronic properties of CMPs in any detail. In the same year, EOF-1, a silane analogue of what were later to be termed PAFs, was reported.<sup>30</sup> This synthesis used an organolithium alkylation route, rather than the transition metal coupling routes favored for CMPs, to produce networks with BET surface areas of up to 1046 m<sup>2</sup> g<sup>-1</sup> that were highly hydrophobic in nature.<sup>30</sup> Also in 2008, Kuhn et al. introduced the ionothermal cyclotrimerization of nitrile monomers at high temperatures (400 °C) to produce conjugated (semi)-crystalline CTFs.<sup>19</sup> Somewhat later, our group reported the use of trifluoromethanesulfonic acid as a strong Brønsted acid to catalyze the synthesis of amorphous CTFs, both under room temperature and microwave-assisted



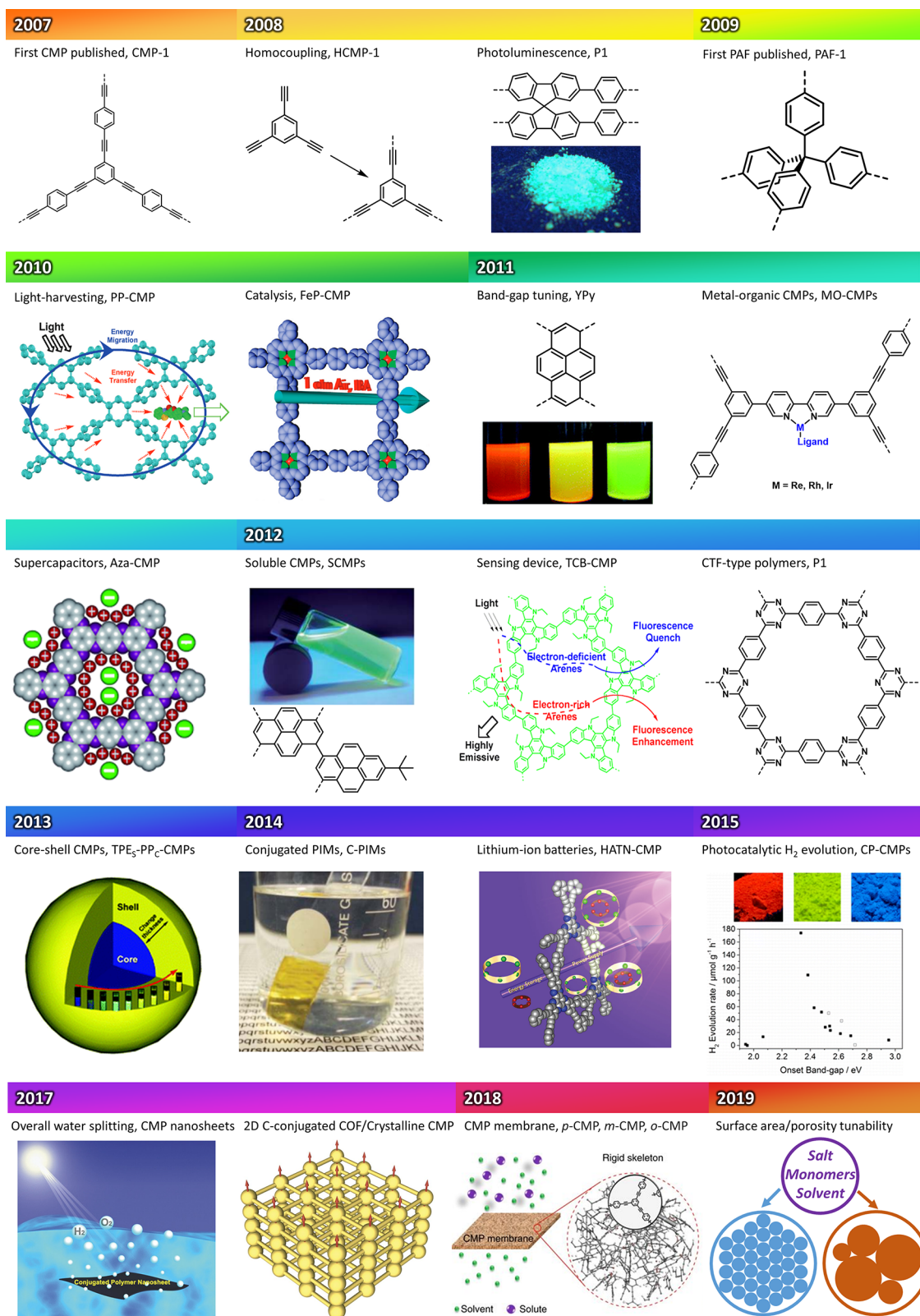


**Figure 3.** A timeline for the development of CMPs and related materials. From top left: 2007, first reported CMP, CMP-1;<sup>25</sup> 2008, homocoupled CMP, HCMP-1;<sup>40</sup> photoluminescence, P1;<sup>41</sup> 2009, first reported PAF, PAF-1;<sup>22</sup> 2010, light harvesting, PP-CMP;<sup>42</sup> catalysis, FeP-CMP;<sup>43</sup> 2011, band gap tuning, YPy;<sup>44</sup> metal-organic CMPs, MO-CMPs;<sup>45</sup> supercapacitors, aza-CMP;<sup>46</sup> 2012, soluble CMPs, SCMPs;<sup>47</sup> sensing devices, TCB-CMP;<sup>48</sup> CTF-type polymers, P1;<sup>20</sup> 2013, core-shell CMPs, TPE<sub>s</sub>-PP<sub>c</sub>-CMPs;<sup>49</sup> 2014, conjugated PIMs, C-PIMs;<sup>50</sup> lithium-ion batteries, HATN-CMP;<sup>51</sup> 2015, photocatalytic H<sub>2</sub> evolution; CP-CMPs;<sup>52</sup> 2017, a report suggests overall water splitting in CMPs,<sup>53</sup> 2D conjugated COF/2D CMP;<sup>54</sup> 2018, CMP membrane,<sup>55</sup> and 2019, tunable surface area and porosity.<sup>56</sup>



conditions.<sup>20</sup> These CTFs possessed BET surface areas up to 1152 m<sup>2</sup> g<sup>-1</sup> and showed tunable absorption and photoluminescence properties, depending on the choice of monomers.<sup>20</sup>

In 2009, Ben et al. reported the first porous aromatic framework, or PAF. The synthesis used metal-catalyzed reactions, similar to those used for CMPs. The resultant material, PAF-1, lacked extended  $\pi$ -conjugation but exhibited an extremely high surface area of 5640 m<sup>2</sup> g<sup>-1</sup>.<sup>22</sup> This stems from the rigid tetrahedral monomer building block, and the resulting network is essentially isostructural with silica.<sup>61</sup> The PAF family developed strongly over the years alongside their closely related CMP analogues (Figure 2), and in terms of surface areas, at least, the offspring have eclipsed the parents: a silica-containing analogue of PAF-1, PPN-4, was reported with the highest recorded apparent BET surface area for a wholly organic material of 6461 m<sup>2</sup> g<sup>-1</sup>.<sup>62</sup>

In 2010, the Jiang group demonstrated the first example of light-harvesting using polyphenylene-based CMPs as antennas, with the micropores confining Coumarin 6 as an energy-accepting molecule.<sup>42</sup> In the same year, this group also demonstrated the use of a porphyrin-containing CMP as a heterogeneous catalyst to convert sulfide to sulfoxide through activation of molecular oxygen.<sup>43</sup> This material showed high efficiency with conversions and selectivities of up to 99% and turnover numbers (TONs) close to 100,000. In the following year, our group reported strongly fluorescent CMPs based on the Yamamoto coupling of tetrabromopyrene with varying amounts of dibromobenzene and dibromophenyl comonomers, allowing fine band gap and emission color tuning.<sup>44</sup> These materials have potential in organic electronics, optoelectronics, sensing technologies, and photoredox catalysis, and laid the foundation of recently discovered CMPs for photochemical H<sub>2</sub> evolution.<sup>52</sup>

In 2011, a bridge was developed between the worlds of CMPs and MOFs, although this concept has yet to be exploited more widely. "Metal-organic CMPs" were produced,<sup>45</sup> either through post-treating bipyridine-functionalized CMPs with metal complexes or through the direct, one-pot Sonogashira-Hagihara cross-coupling metal-organic monomers. Rhenium, rhodium, and iridium examples were given that combined conjugation in the framework with metal-organic functionality, and it was shown that the metals could be catalytically active.<sup>45</sup> Also in 2011, the Jiang group reported the use of an aza-fused CMP for supercapacitive energy storage. This synthesis required high temperatures of 300–500 °C and yielded a black powder that functions as a supercapacitor electrode due to the N-containing, conducting, microporous nature of the material.<sup>46</sup>

CMPs are generally completely insoluble because of their highly conjugated and rigid network structure. In 2012, our group addressed this issue by synthesizing hyperbranched CMPs by introducing *tert*-butyl-functionalized groups, which both reduce the molecular weight of the material and incorporate solubilizing alkyl groups.<sup>47</sup> That year, the Jiang group also developed luminescent carbazole-based CMPs as molecular sensing devices.<sup>48</sup> These CMPs showed enhanced detection selectivity compared with linear nonporous polymer analogues.

In 2013, a core-shell strategy was shown to allow the tuning of light emission over a wide wavelength range.<sup>49</sup> By fixing the size of the core but changing the shell thickness, the light emission was controlled, giving a series of colors from deep

blue to sky blue, near white, green, light yellow, and deep yellow.<sup>49</sup>

The following year, our group reported the preparation of conjugated PIMs, or C-PIMs, which combined the electronic properties of CMPs with the solution processability of linear PIMs.<sup>50</sup> Of the 18 polymers reported in this study, 16 were found to be permanently microporous with BET surface areas as high as 728 m<sup>2</sup> g<sup>-1</sup> and molecular weights close to 2 000 000 g/mol in some cases. Around the same time, Jiang et al. reported the synthesis of a hexaazatrinaphthalene CMP, which contained redox-active sites for use in lithium-ion batteries.<sup>51</sup> This material possessed a BET surface area of 616 m<sup>2</sup> g<sup>-1</sup> and exhibited capacities as high as 147 mA h g<sup>-1</sup>, attributed to the hierarchical structure of the CMP which facilitates access of the electrolyte ions to the redox-active sites of the CMP.

The optical band gap in CMPs allows opportunities in photocatalysis.<sup>44,63,64</sup> In 2015, our group reported a series of CMP networks that exhibit photocatalytic H<sub>2</sub> evolution from water, in the presence of a sacrificial electron donor, without any additional metal catalysts.<sup>52</sup> The optical gap in these networks could be tuned over a wide range in continuous fashion by varying the monomer composition. These CMPs are potentially advantageous in comparison to linear conjugated polymers, which are often poorly active in visible light, and graphitic carbon nitrides, where it is challenging to tune the optical gap.<sup>65,66</sup>

Development of CMP networks active for water splitting over a wide optical gap range is a current hot topic in CMP chemistry. In 2017, Wang et al. reported that it was possible for CMPs to directly split water into H<sub>2</sub> and O<sub>2</sub> under visible light,<sup>53</sup> though the mechanism for this is unclear, and as yet there are no further examples of this. In one case, this remarkable behavior was found for a diyne CMI<sup>40</sup> that had been reported previously but not investigated for water splitting. In the same year, the Jiang group reported the first 2D *sp*<sup>2</sup> carbon-conjugated COF, which might also be considered as crystalline CMPs.<sup>54</sup> The 2D lattice extends in both *x* and *y* directions to produce a layered framework which can align spins unidirectionally across the material.

Although various CMPs have been reported for uses as membranes for filtration, the difficulty in producing thin films require them to be templated which needs to be removed or synthesized with defects. In 2018, Liang and co-workers showed that by first polymerizing CMP membranes on a bromobenzene-functionalized surface and then transferring them to porous supports, this can form large-area and defect-free CMP membranes for organic-solvent nanofiltration.<sup>55</sup> The engineered CMPs showed exceptionally high performance, outperforming all state-of-the-art polymer membranes, likely resparking interest in this area.

CMPs in general are microporous but may be accompanied by high levels of mesoporosity. Additionally, products with low porosity may also result even when using general CMP-forming chemistry. Recently, control of surface area and porosity formation in N-containing CMPs was demonstrated by Faul et al.<sup>56</sup> They tuned the Buchwald-Hartwig cross-coupling reaction with the use of salts with different-sized cations or anions, yielding CMPs with 20 times higher surface area than the standard reaction. The group proposed that the salts optimized the Hansen solubility parameters of solvents for the growing polymer, resulting in phase separation of the polymer at a later stage.

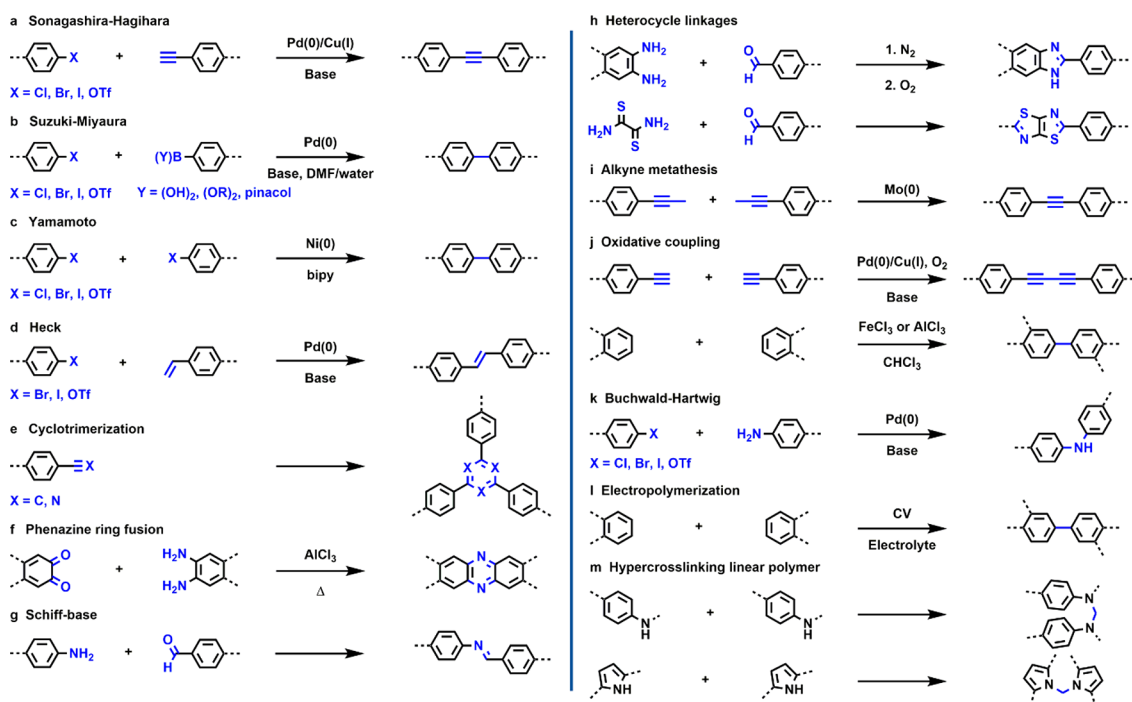


**Figure 4.** Reaction schemes for the synthesis of CMPs. (a) Sonogashira-Hagihara, (b) Suzuki-Miyaura, (c) Yamamoto, (d) Heck, (e) cyclotrimerization, (f) phenazine ring fusion, (g) Schiff-base, (h) heterocycle linkages, (i) alkyne metathesis, (j) oxidative coupling, (k) Buchwald-Hartwig, (l) electropolymerization, and (m) hypercrosslinking linear polymers.

## 2. DESIGN AND SYNTHESIS ROUTES

CMP networks can be formed through the reaction of two or more different monomers or, in some cases, by homocoupling of a single monomer. The most common approach so far is the combination of a “core” of  $C_3$  symmetry with a “linker” with  $C_2$  symmetry, as put forward in the first CMPs.<sup>25</sup> Homocoupling of trifunctional or polyfunctional monomers can also result in 3D porous networks, with the most well-known example being PAFs, which are formed from the homocoupling of tetrafunctional, tetrahedral monomers.<sup>22</sup> 2D monomers afford 3D polymers due to free rotation of the core-linker bond during reaction, and subsequent reactions may not form the complete 2D pore. The absence of reversibility in these kinetic couplings mean the structure cannot be corrected to a more thermodynamically stable product (*cf.*, COFs). Many 3D building blocks, such as the tetrahedral monomers used in PAFs, cannot be used to synthesize CMPs because the tetrahedral node breaks the extended  $\pi$ -conjugation. There are, however, strategies to avoid this, such as the use of spirobifluorene linkers (Figure 3).<sup>41,67,68</sup>

As for MOFs, the scope for customization of CMPs is almost limitless. There are extensive options for tuning pore structure, morphology, and optoelectronics by varying the monomer geometry or by incorporating different heteroatoms or metals; it is also possible to postsynthetically modify CMPs.<sup>69,70</sup> A wide range of reactive coupling groups has been used for CMP synthesis, including halogens, boronic acids, alkynes, alkenes, nitriles, amine, aldehydes, and activated phenol-substituted aromatic monomers; more are sure to be discovered in the future. The most common reaction methods used to synthesize CMPs are summarized in Figure 4.

### 2.1. Sonogashira-Hagihara Coupling

The first CMPs were prepared using Sonogashira-Hagihara cross-couplings,<sup>25</sup> not because this reaction is uniquely

effective but because we wanted to introduce lightweight alkyne struts. This reaction couples an aryl halide with an alkyne-containing monomer using a palladium catalyst and a copper cocatalyst, often tetrakis(triphenylphosphine)palladium and copper iodide, in the presence of an amine base. The presence of a Cu cocatalyst is used in the coupling due to the improved reactivity,<sup>71</sup> although copper-free Sonogashira-Hagihara reactions are also known.<sup>72</sup> Four solvents were studied initially for this chemistry: *N,N*-dimethylformamide (DMF), 1,4-dioxane, tetrahydrofuran (THF), and toluene. In general, it was found that CMPs formed in DMF had the highest surface areas and levels of microporosity.<sup>73</sup> The Sonogashira-Hagihara reaction can also be used for homocoupling reactions.<sup>40</sup> This should be remembered when carrying out cross-couplings, since alkyne-containing monomers may instead homocouple in the presence of oxygen.<sup>74</sup> Hence, rigorous anaerobic and anhydrous conditions should be employed.

### 2.2. Suzuki-Miyaura Coupling

The Suzuki-Miyaura cross-coupling reaction was discovered as a method to link aryl groups in 1979.<sup>75,76</sup> The reaction uses a Pd(0) catalyst, such as tetrakis(triphenylphosphine)-palladium(0), to couple an aryl-boron monomer with an aryl halide or sulfonate in the presence of a mild base, such as  $K_2CO_3$  in DMF/water.<sup>42</sup> This method has various advantages including commercial availability of boronic acids, wide functional group compatibility, and mild reaction conditions, and hence the potential for scale-up. A downside is that Suzuki-Miyaura cross-couplings are oxygen sensitive, which leads to homocoupling and deboronated byproducts. To tackle this, reactions should be thoroughly degassed.<sup>77</sup>

### 2.3. Yamamoto Coupling

In Yamamoto coupling, aryl halides with at least 3 reactive sites are coupled together with bis(cyclooctadiene)nickel(0) (Ni-

(cod)<sub>2</sub>).<sup>78</sup> The advantage of this coupling method is that only a single, halogen-functionalized monomer is required, leading to a simple reaction procedure. There are a diverse range of aryl halide monomers, therefore many porous networks can be designed through Yamamoto couplings, including CMPs.<sup>44,78</sup> When using 3D monomers, Yamamoto reactions can induce very inefficient packing to give remarkably high surface areas and porosity, as with the case in PAF-1.<sup>22</sup> A drawback of this route that may preclude scale up is the high sensitivity to water, which often necessitates reactions to be done in glovebox.

## 2.4. Heck Coupling

The Heck reaction, also known as the Mizoroki-Heck reaction, forms a C=C bond between two units by coupling an unsaturated halide with a primary alkene in the presence of a Pd catalyst and base. CMPs produced from this reaction commonly use Pd(Ph<sub>3</sub>)<sub>4</sub>, K<sub>2</sub>CO<sub>3</sub> base, and DMF solvent under anaerobic conditions.<sup>79</sup> Suzuki-Heck one-pot reactions have also been utilized to form similar CMP products.<sup>80</sup> The method utilizes aryl halides as the monomer where some are substituted with an alkene functional group via Suzuki-Miyaura and then reacts with the remaining aryl halide via Heck reaction.

## 2.5. Cyclotrimerization Reactions

Cyclotrimerizations typically form aromatic 6-membered rings: for example, from three alkyne monomers, which further link to form an extended network.<sup>81</sup> Similarly, the use of cyano-functionalized monomers generates C<sub>3</sub>N<sub>3</sub> *s*-triazine rings. Nitrile cyclotrimerizations can be carried out under ionothermal conditions in molten ZnCl<sub>2</sub> at temperatures of over 400 °C.<sup>19,21,82</sup> However, such harsh conditions rules out the use of all but the most stable monomers, and a degree of carbonization can occur. The use of Brønsted acid-catalyzed trimerizations was also developed, which allows the reaction to proceed at room temperature or at modest temperatures under microwave heating.<sup>20</sup> This method uses trifluoromethanesulfonic acid with CHCl<sub>3</sub> as the solvent, or it can occur by microwave synthesis without the use of any solvent. Microwave-assisted reactions allow much shorter reaction times to tens of minutes at microwave outputs of 120–460 W. A recent report allowed the formation of triazines through a low-temperature polycondensation approach.<sup>83</sup> Trimerizations using different groups to cyano-functionalized monomers have also been reported. Amide groups have been shown to trimerize in the presence of P<sub>2</sub>O<sub>5</sub> as a catalyst at temperatures between 350 and 550 °C.<sup>84</sup> A nontraditional, covalent quinazoline network which is fully aromatic and contains tricycloquinazoline cores was synthesized with *o*-aminonitrile monomers under ionothermal conditions with ZnCl<sub>2</sub>.<sup>85</sup>

## 2.6. Phenazine Ring Fusion

Ladder-type polymers have been produced since 1966 via phenazine ring fusions.<sup>86,87</sup> The reaction links between aryl diamines and aryl diketones at temperatures of 250 °C in specific, high-boiling solvents, such *N,N*-dimethylacetamide hexamethylphosphoramide and 116% polyphosphoric acid. More recently, phenazine ring fusion has been used to produce Aza-CMPs.<sup>46</sup> The reported method uses C<sub>2</sub> + C<sub>6</sub> monomers to create a 3D ladder CMP network in the presence of AlCl<sub>3</sub> at high temperatures (300–500 °C) in an evacuated ampule. Recently, a mild solvothermal method was developed to

prepare Aza-CMPs by refluxing the monomers in a 1:4 mixture of dioxane and acetic acid.<sup>88</sup>

## 2.7. Schiff-Base Condensations

Schiff-base reactions have been used to synthesize both CMPs and imine-based COFs.<sup>13</sup> The reaction is metal free, reducing cost and avoiding any trapped metal residues in the CMP network. The reaction forms an imine bond from amine and aldehyde-functionalized monomers.<sup>89</sup> A benefit of Schiff-base reactions is that they produce N-containing CMPs, which are favored in applications such as selective CO<sub>2</sub> adsorption.<sup>90,91</sup>

## 2.8. Heterocycle Linkages

Using similar monomers to those used for Schiff-base condensations, ortho diamines can be used to form benzimidazole linkages in the presence of an aldehyde.<sup>92</sup> Rabbani and El-Kaderi performed this reaction in DMF under inert conditions and then flushed with air to react further and produce a porous polymer. Thiazolothiazole-linked CMPs can be synthesized with dithiooxamide and an aldehyde monomer. The reaction can be performed under conventional reflux conditions with DMF or nitrobenzene at 150 °C,<sup>93</sup> or solvothermally in DMF at 160 °C.<sup>94</sup>

## 2.9. Alkyne Metathesis

In 1968, Bailey et al. reported the first alkyne metathesis reaction using catalytic tungsten oxide on silica at 350 °C.<sup>95</sup> The method was used to produce CMPs using a Mo(VI)-based catalyst in CHCl<sub>3</sub> at mild temperatures.<sup>96</sup> Although the reaction is reversible, the CMP produced was reported to be semicrystalline. This reaction is different to homocoupling terminal alkynes in that only one alkyne group is present in the product, rather than a diyne, between the two linked monomers.

## 2.10. Oxidative Coupling

Terminal alkynes can be coupled together using Sonogashira-Hagihara conditions (Pd(II)/Cu(I), Et<sub>3</sub>N, solvent) in the presence of O<sub>2</sub>.<sup>40</sup> In addition, CMPs can be produced by oxidative Scholl reactions of electron-rich aromatics using a Lewis acid catalyst, commonly FeCl<sub>3</sub> or AlCl<sub>3</sub> in CHCl<sub>3</sub> solvent.<sup>97,98</sup> This method, which was first observed by Friedel and Crafts over a hundred years ago,<sup>99</sup> uses relatively inexpensive catalysts, which simplifies production and reduces costs.

## 2.11. Buchwald-Hartwig Amination

Carbon–nitrogen bonds can be formed in a facile synthesis using a Pd catalyst and base. This was recently utilized to produce N-rich CMPs with an aryl halide and aryl amine in the presence of bis(dibenzylideneacetone)palladium(0) (Pd(dba)<sub>2</sub>), 2-dicyclohexylphosphino-2',4',6'-triisopropylbiphenyl (XPhos), and sodium tert-butoxide (NaOtBu) in toluene at 110 °C.<sup>100,101</sup>

## 2.12. Electropolymerization

Oxidative coupling can also be performed via an electrochemical route using cyclic voltammetry (CV) to yield CMP films.<sup>102–105</sup> Ma et al. reported the first synthesis of electropolymerized CMPs using a carbazole functionalized monomer with Bu<sub>4</sub>NPF<sub>6</sub> in acetonitrile/CH<sub>2</sub>Cl<sub>2</sub> electrolyte by multicycling CV in at the potential range of –0.8 to 0.97 V at a scan rate of 50 mV s<sup>–1</sup>. The onset oxidative potential of the monomer could be observed at 0.93 V, which was attributed to the oxidation of the carbazole groups. A new peak was later observed at a lower potential with increasing scan cycles due to



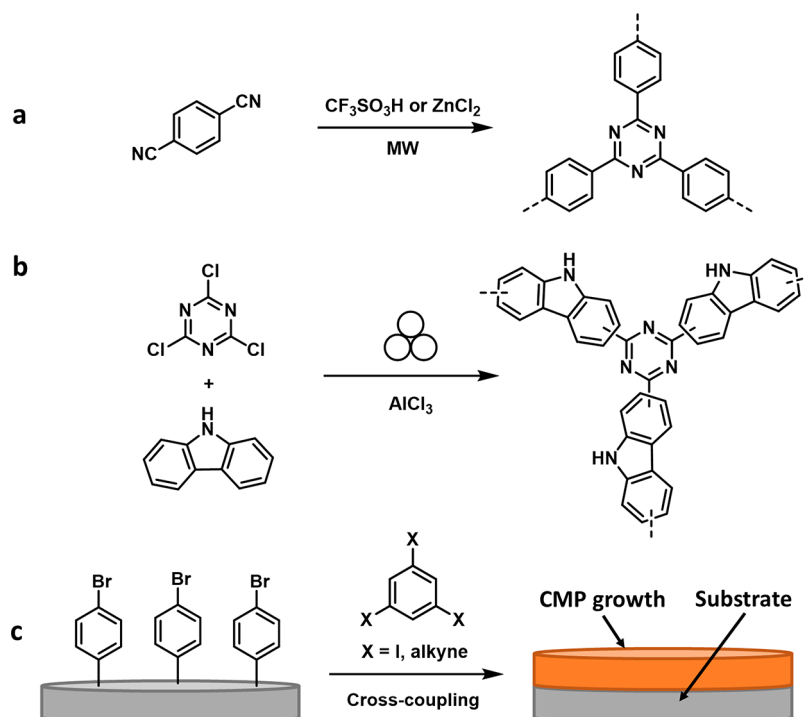


**Figure 5.** Unconventional CMP synthesis routes. (a) Microwave synthesis. (b) Mechanochemical synthesis. (c) Synthesis of CMPs on a substrate.

the formation of dimeric carbazoles and the growth of CMP film on the electrode.<sup>102</sup>

### 2.13. Hypercrosslinking Linear Conjugated Polymers

An interesting approach to produce CMPs is hypercrosslinking of preformed linear conjugated polymers. Reacting linear polyaniline or linear polypyrrole with a cross-linker resulted in BET surface areas as high as 632 and 732 m<sup>2</sup> g<sup>-1</sup>, respectively.<sup>106,107</sup> The reaction method, choice of solvent, and choice of cross-linker greatly affected the porosity.

### 2.14. Synthesis Parameters Affecting Functionality

The type of coupling reaction that is chosen can affect the resulting properties of the CMP. In particular, subtle differences in polymer structure, and by extension semiconducting behavior, can be affected by the choice of coupling chemistry. For example, CP-CMP15 (a polypyrrole network) synthesized by Suzuki-Miyaura coupling has an absorption onset and a photoluminescence maximum that are more blue-shifted than the equivalent CMP synthesized by Yamamoto coupling.<sup>52</sup> Synthetic parameters also can be tuned in order to improve functionality and to produce libraries of materials. For instance, the average pore size can be increased incrementally by using monomers with increasing strut length.<sup>60</sup> The BET surface area was found to decrease with increasing pore size in this case. Reaction solvent choice can affect the porosity of CMPs, even when using the same monomers. Toluene was used for early synthesis of the first CMPs,<sup>25</sup> but we later found that DMF, dioxane, and THF could give different levels of porosity, depending on the specific monomer combination.<sup>73</sup> We concluded that no “universal” solvent is optimal; as such, researchers should spend time to investigate this parameter when new materials are being prepared. A recent study shows that the addition of salts can affect solubility parameters, which controls aspects of the polymerization.<sup>56</sup> Good solvent compatibility with the polymerization results in the formation

of more micropores, a higher polymerization degree and, generally, higher surface areas.

### 2.15. Unconventional Synthesis Methods and Composites

CMPs are most commonly synthesized by solution-phase synthesis routes in conventional glassware, but more unconventional routes can also have their advantages.

Microwave-assisted synthesis allows for time- and energy-efficient syntheses. As discussed earlier, Brønsted acid catalyzed CTFs can be synthesized in tens of minutes at microwave outputs of 120–460 W (Figure 5a).<sup>20</sup> CTFs can also be synthesized using microwaves via a ZnCl<sub>2</sub> salt-melt route.<sup>108</sup> Successful microwave-assisted synthesis using Suzuki coupling<sup>109</sup> and Schiff base reaction<sup>110</sup> have also been reported, requiring the same microwave heating temperatures as their solution-synthesized equivalents but within a shorter reaction time (2 h instead).

Mechanochemistry can sometimes allow for materials to be synthesized with low reaction times and in the absence of solvent (or with very little solvent). To our knowledge, only a single report on mechanochemistry currently exists based on the Fredel-Crafts alkylation. Cyanuric chloride and an aromatic comonomer with the presence of AlCl<sub>3</sub> can react to form CTFs in quantitative yield in 1 h through solvent-free mechanochemical synthesis (Figure 5b).<sup>111</sup> It is likely that further CMPs synthesized by mechanochemistry will be reported. Perhaps the biggest impact might be in discovering CMPs that could not be made by traditional solution synthesis methods, for example because the monomers are not soluble.

Composite synthesis of CMPs on surfaces allow for the substrate to impart additional properties to the structural design of the CMP. CMPs can be chemically grafted onto a reduced graphene oxide (rGO) surface by first grafting a typical CMP monomer onto the surface (Figure 5c).<sup>112</sup> A polymerization can then be performed, with the rGO imparting electrical conductivity to the material, which is not

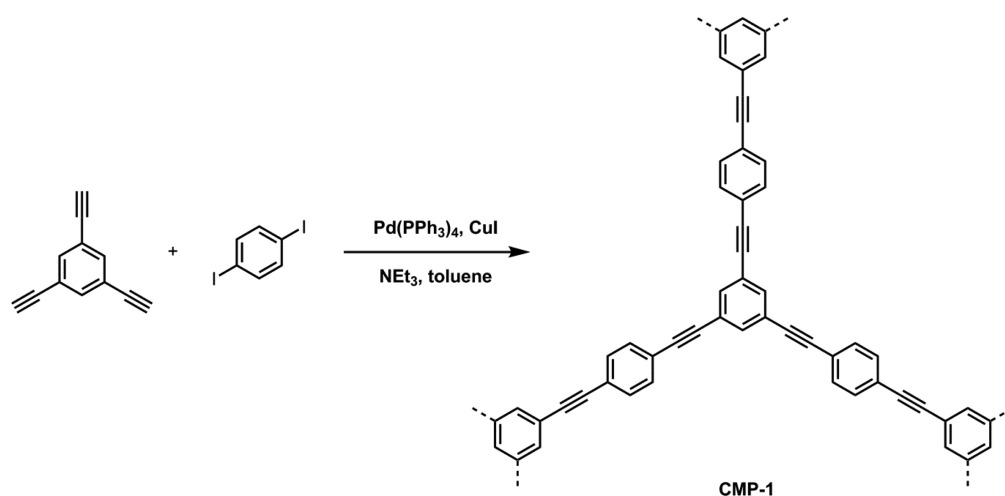


Figure 6. Synthesis of poly(aryleneethynylene) network, CMP-1.<sup>25</sup>

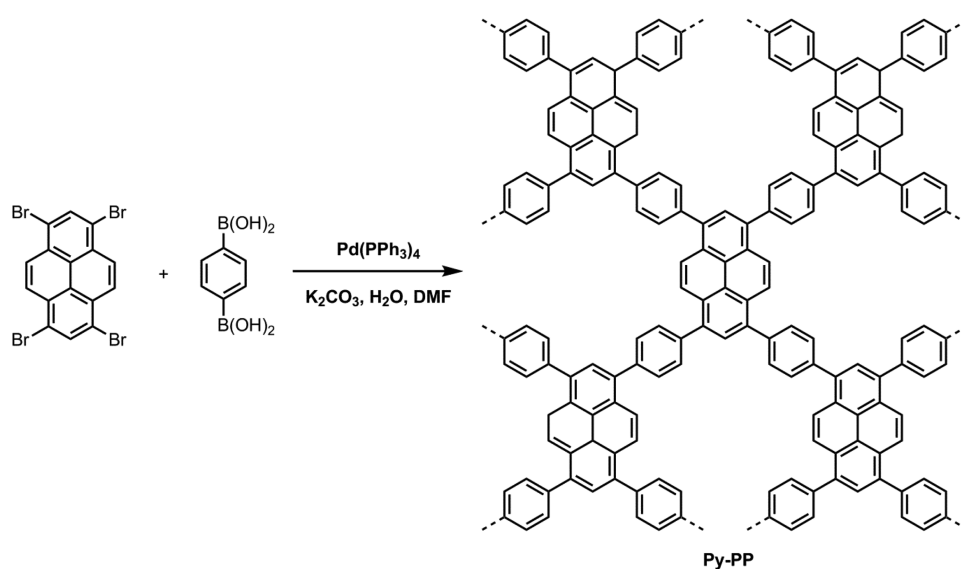


Figure 7. Synthesis of pyrene-based CMP, Py-PP.<sup>117</sup>

typically an intrinsic property of CMPs. Other substrates can also be used, such as a polyacetonitrile support that allows for CMPs to be used as membranes.<sup>55</sup>

### 3. APPLICATIONS OF CMPS

CMPS have potential to be used in a diverse range of applications, based on their extended conjugation, high porosity, tunable chemistry, and often excellent chemical and thermal stabilities. Indeed, CMPS have been evaluated for gas storage and separations,<sup>25,113–115</sup> encapsulation of chemicals,<sup>116–119</sup> heterogeneous catalysis,<sup>43,120–123</sup> photoredox catalysis,<sup>124–131</sup> light emittance,<sup>44,49,132–135</sup> chemosensing,<sup>48,79,80,136–138</sup> energy storage,<sup>46,51,100,104,139–146</sup> biological,<sup>103,147–153</sup> and photocatalytic H<sub>2</sub> evolution.<sup>52,53,154–160</sup> In this section, we review the performance of CMPS in these applications, with a particular emphasis on the applications that exploit the extended  $\pi$ -conjugation in these materials.

#### 3.1. Gas Storage and Separation

The largest area of study for CMPS thus far is the adsorption and storage of gases.<sup>29,161,162</sup> The synthetic control over structure and composition in CMPS offers strategies to

heighten adsorption capacity and selectivity. However, the use of expensive transition metals in many CMP syntheses might prohibit their use in large-scale adsorption applications. The storage of H<sub>2</sub>, CH<sub>4</sub>, and CO<sub>2</sub> are the most widely studied areas. Interest in H<sub>2</sub> and CH<sub>4</sub> is driven by their potential use as fuels. CO<sub>2</sub> is the primary greenhouse and contributes to global warming and acidification of the oceans, and hence sorbents for this gas are of interest.

We first reported poly(aryleneethynylene) networks in 2007 for the storage of H<sub>2</sub> (Figure 6). CMP-1 had a BET surface area of 834 m<sup>2</sup> g<sup>-1</sup> and a modest H<sub>2</sub> uptake of 0.99 wt % at 77.3 K and 1 bar.<sup>25</sup> CO<sub>2</sub> sorption capacities were later found to be 0.97 mmol g<sup>-1</sup> at 298 K and 1 bar.<sup>163</sup> Tuning of CMP structures can lead to even much higher storage capacities; for example, FCTF-1–600, a CTF with 1535 m<sup>2</sup> g<sup>-1</sup> BET surface area, exhibits a CO<sub>2</sub> uptake of 3.41 mmol g<sup>-1</sup> at 298 K and 1 bar.<sup>113</sup> CMPS can also be used for separation applications by tailoring the size and shape of the pores to host one guest more strongly than the other.<sup>115</sup> CMPS also are processed into membranes and show favorable selectivities for gases with small kinetic diameters.<sup>114</sup> In general, though, it is not clear at this stage that CMPS offer a particular advantage for gas

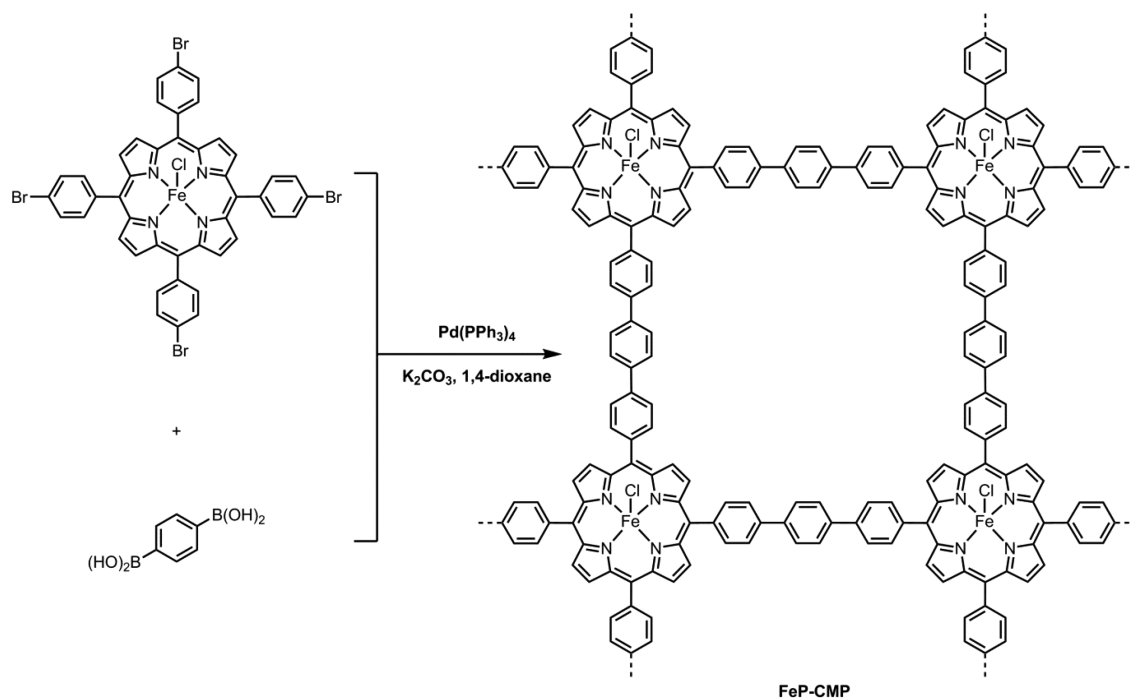


**Figure 8.** Synthesis of iron(III) porphyrin-based CMP, FeP-CMP.<sup>43</sup>

storage or separation over other porous materials, either in terms of efficacy, cost, or processability. It is possible that some of the most interesting opportunities lie in solution-processable linear CMPs, or “C-PIMs”,<sup>50</sup> for membrane formation, where the conjugation serves to rigidify the polymer backbone rather than to give an optoelectronic effect.

### 3.2. Adsorption and Encapsulation of Chemicals

The pores of CMPs can also be tuned to capture various chemicals other than permanent gases, such as dyes, organic solvents, and other substances. In 2009, our group showed that pores of CMPs can be functionalized to take up particular guests, or not, based on hydrophobicity.<sup>116</sup> The presence of hydrophilic hydroxyl groups in the network favored uptake of the water-soluble methyl orange dye; by contrast, the presence of a methyl-substituted group in the structure disfavored dye uptake, even when the micropore volumes were similar.<sup>116</sup>

George et al. reported guest-responsive swelling in a poly tetraphenyl pyrene (Py-PP), which encapsulates dye molecules at room temperature, such as red-emitting 4-(dicyanomethylene)-2-methyl-6-(4-dimethylaminostyryl)-4H-pyran (DMDP) and Nile red (NR), as well as C<sub>60</sub> (Figure 7).<sup>117,119</sup> When Py-PP (BET surface area = 1070 m<sup>2</sup> g<sup>-1</sup>) was placed into a saturated C<sub>60</sub> solution in toluene, the solution immediately became colorless, indicating efficient and instantaneous uptake of C<sub>60</sub> into the pores. This suggests possible future applications where a bulk heterojunction is formed by fullerene encapsulation within a preformed CMP network. The same network also showed high uptake of diesel (1200 wt %) from water because of its hydrophobic nature. The absorbed oil could be recovered by simply compressing the material.<sup>117</sup> The Ma group also showed that the porphyrin-based polymer, PCPF-1 (BET surface area = 1300 m<sup>2</sup> g<sup>-1</sup>), has very high adsorption capacities (1470 to 2590 wt %) for gasoline and saturated hydrocarbons, such as *n*-pentane, *n*-hexane, *n*-heptane, *n*-octane, cyclopentane, and cyclohexane.<sup>118</sup>

### 3.3. Heterogeneous Catalysis

The ability to functionalize CMPs with catalytic sites in the network makes them promising candidates for heterogeneous catalysts. The open, porous structure allows easy access of reactants to the catalytic sites compared with nonporous analogues. Also, the extended, conjugated chromophores in CMPs make them particularly intriguing as photoredox catalysts.

In 2010, the Jiang group developed the first examples of CMP-based catalysts with an iron-based porphyrin network, FeP-CMP.<sup>43</sup> FeP-CMP was synthesized by Suzuki-Miyaura cross-coupling polycondensation of an iron(III) tetrakis(4'-bromophenyl)porphyrin derivative with 1,4-phenyldiboric acid (Figure 8). The network is microporous with a BET surface area of 1270 m<sup>2</sup> g<sup>-1</sup>, which aids access to the catalytic metalloporphyrin sites to yield a high turnover number (TON). The FeP-CMP was able to activate molecular oxygen and to catalyze the oxidation of various sulfides with conversions as high as 97% and TONs as high as 97,320.<sup>43</sup> The same group also showed that Fe-CMP can be used in catalytic epoxidation of olefins under aerobic, ambient conditions.<sup>164</sup>

Deng et al. both captured and utilized CO<sub>2</sub> with Co- and Al-functionalized CMPs. The materials had CO<sub>2</sub> uptakes of up to 1.80 mmol g<sup>-1</sup>. When these metal-CMPs were combined with a quaternary ammonium cocatalyst, TBAB, they displayed high catalytic activities to convert propylene oxide into propylene carbonate at atmospheric pressure and room temperature, with yields of up to 98.1% and TONs up to 201.<sup>120</sup>

The Müllen group developed a cobalt-based porphyrin CMP electrocatalyst, CoP-CMP, for oxygen reduction reactions.<sup>121</sup> The network was synthesized via a Yamamoto homocoupling of 5,10,15,20-tetrakis(4'-bromophenyl) porphyrin-Co(II). CoP-CMP was then thermally treated at temperatures between 600 and 1000 °C to yield nitrogen-rich porous carbons with embedded cobalt nanoparticles. CoP-CMP pyrolyzed at 800



°C showed excellent performance with an onset potential observed with CV at  $-0.12$  V, a half-wave potential of  $-0.18$  V, and mainly a four-electron oxygen reduction process in  $O_2$ -saturated  $0.1$  M KOH (Figure 9). The superior activity was

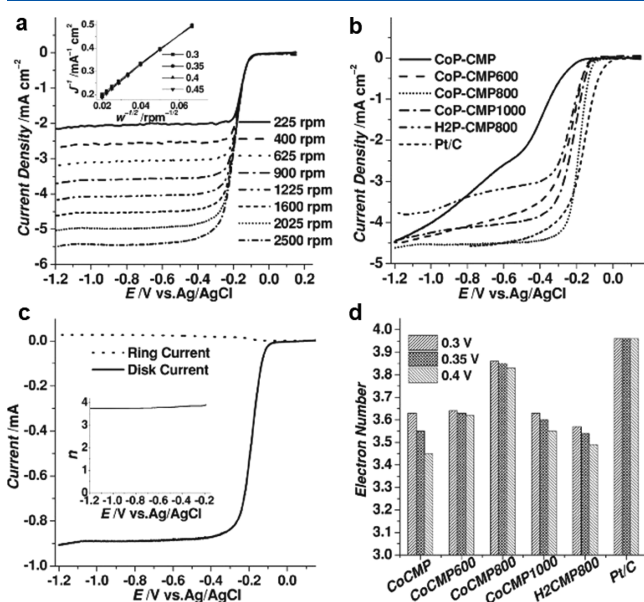


**Figure 9.** (a) Linear sweep voltammetry curves for CoP-CMP800 at different rotation rates in  $O_2$ -saturated  $0.1$  M KOH at  $10$   $mV s^{-1}$ . Inset shows the Koutecky–Levich (K-L) plot. (b) Linear sweep voltammetry curves for various CoP-CMP materials and Pt/C in  $O_2$ -saturated  $0.1$  M KOH at  $10$   $mV s^{-1}$  at  $1600$  rpm. (c) RRDE test of the ORR on CoP-CMP800 in  $O_2$ -saturated  $0.1$  M KOH electrolyte at  $1600$  rpm. Inset shows the electron transfer number ( $n$ ) against electrode potential. (d) The  $n$  values of various CoP-CMPs and Pt/C against electrode potential. Reprinted with permission from ref 121. Copyright 2014 Wiley-VCH.

prescribed to the high surface area of  $\sim 480$   $m^2 g^{-1}$  and mesoporous structure that allowed close interaction of oxygen with to the Co–N active sites.<sup>121</sup> In this case, the CMP is more a precursor, rather than the catalyst per se. More recently, the Du group reported a copper porphyrin-based CMP for both  $H_2$  evolution and oxygen evolution to allow overall water splitting.<sup>122</sup>

Feng and co-workers showed that one-dimensional CMPs could be prepared by templating them onto carbon nanotubes through a “layer-by-layer method”.<sup>123</sup> The materials had surface areas of up  $623$   $m^2 g^{-1}$  and exhibited strong electronic interactions between the  $p$ -type CMP and the  $n$ -type carbon

nanotube and could be used for oxygen reduction reactions upon pyrolysis.

### 3.4. Photoredox Catalysis

In 2013, Vilela et al. reported a benzothiadiazole-based CMP for photocatalytic oxygen activation with porosity-dependent activity.<sup>126</sup> The networks were synthesized through Sonogashira-Hagihara cross-coupling of 4,7-dibromobenzo[*c*]-1,2,5-thiadiazole with 1,3,5-triethynylbenzene with silica nanoparticles as templating agents to control porosity (from  $270$   $m^2 g^{-1}$  in nontemplated to  $660$   $m^2 g^{-1}$  with excess template) which is then removed (Figure 10). The most porous CMP was able to oxidize  $\alpha$ -terpinene into ascaridole in 96% conversion with  $420$  nm irradiation. The photocatalytic performance was observed to increase with surface area but dispersibility and the effective surface area in contact with reactants was also noted to influence activity as the lower density CMPs resulted in more stable dispersions, thus more efficient singlet oxygen production.<sup>126</sup>

The Son group reported benzodifuran-containing CMPs as a photoredox catalyst for conversion of primary amines into imines.<sup>125</sup> Benzodifuran-containing organic polymers have previously showed promising photoelectrical performances in polymer solar cells.<sup>165</sup> Sonogashira-Hagihara couplings of 1,3,5-triethynylbenzene and 2,5-diiodo-1,4-hydroquinone yielded BDF-MON with a BET surface area of  $455$   $m^2 g^{-1}$ . The network was able to mediate electron transfer from 1,4-bis(dimethylamino)benzene to oxygen to generate a blue-colored cationic radical species with strong absorption peaks at  $565$  and  $614$  nm under irradiation with a blue LED. Using BDF-MON under blue LED irradiation resulted in photocatalytic amine conversions of up to 98%. Photoirradiation was confirmed with control experiments covering the glassware and in absence of catalyst. Density functional theory calculations showed that the LUMO of BDF-MON was higher than that of oxygen and the HOMO of benzylamine was higher than that of the SOMO of oxidized BDF-MON and thus was suggested to follow an oxidative quenching process.<sup>125</sup>

Zhang and co-workers synthesized CMPs with the high internal phase emulsion polymerization (polyHIPE) method and examined their performance for photocatalytic oxidation of organic sulfides to desired mono-oxidized sulfoxides under visible light irradiation.<sup>127</sup> The initial CMPs synthesized via Suzuki-Miyaura cross-coupling contained cleavable *tert*-butyl carboxylate functional groups which can be removed to increase porosity by up to eight times without change in morphology. The polyHIPE CMPs had various electronic properties, with HOMO–LUMO band gaps from  $2.31$  to  $3.31$  eV. Photooxidation of thioanisole at room temperature with

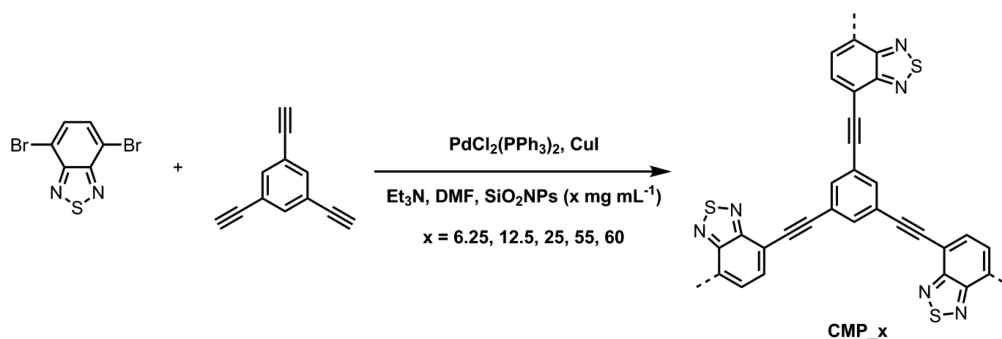


**Figure 10.** Synthesis of CMP photoredox catalysts using  $SiO_2$  nanoparticle templates to control porosity.<sup>126</sup>

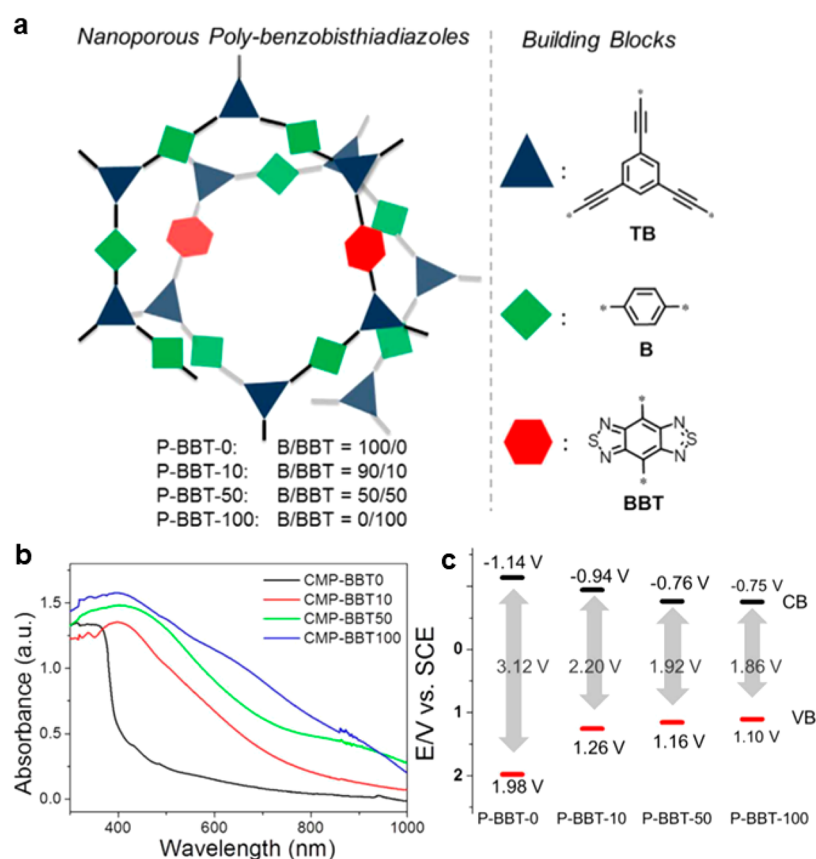


**Figure 11.** (a) Synthesis of polybenzobisthiadiazole-based CMPs series. (b) Diffuse reflectance UV–vis spectra. (c) Conduction band (CB) and valence band (VB) positions of P-BBTs. Adapted with permission from ref 130. Copyright 2016 Wiley-VCH.

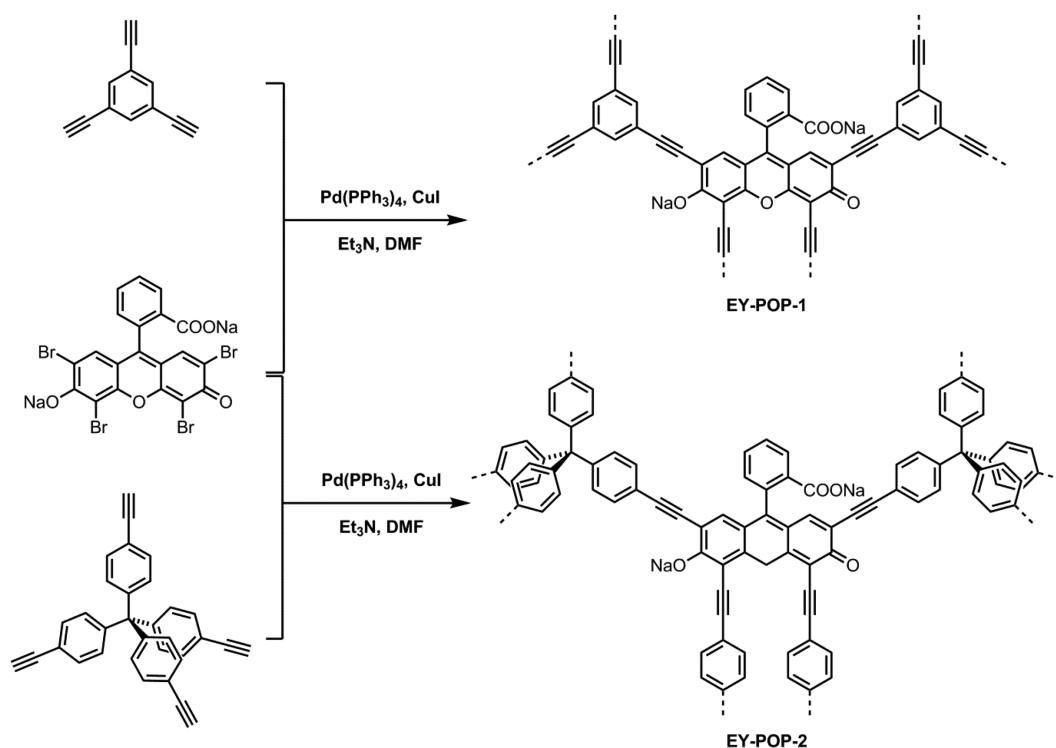


**Figure 12.** (a) Synthesis of Eosin Y dye-embedded porous organic polymers (EY-POPs).<sup>131</sup>

polyHIPE CMPs under visible light yielded almost quantitative selectivity of >99% and up to 99% conversion. The CMP

photoredox catalysts were shown to have general applicability for organic sulfides bearing electron-withdrawing or electron-

donating substituents to produce the mono-oxidized products.<sup>127</sup>

The same group showed that a Pd-immobilized CMP can be used as a photoredox catalyst for Suzuki coupling reactions under visible light via the photoamplified Schottky effect at the metal–semiconductor interface.<sup>128</sup> The Pd-immobilized CMP contained ~3 wt % Pd nanoparticles of sizes between 5 and 10 nm resulting in a BET surface area of 176 m<sup>2</sup> g<sup>-1</sup>, less than the pristine CMP due to the weight increase of the immobilized nanoparticles.

The Zhang group extended this work with band gap engineered polybenzobisthiadiazole-based CMPs (P-BBT) to fine-tune the conduction band (CB) and valence band (VB) levels by copolymerization (Figure 11a).<sup>130</sup> This allowed the optical absorption of the photoredox catalysts to be extended into the visible region and alignment of band positions to bracket the targeted photoredox reaction (Figure 11b). The copolymerization strategy utilizes varying amounts of electron-withdrawing dibromobenzo-1,2-[c];-4,5-[c']bis-1,2,5-thiadiazole (BBT), resulting in BET surface areas from 1017 to 57 m<sup>2</sup> g<sup>-1</sup> with BBT monomer from P-BBT-0 to P-BBT-100. The optical band gaps also decreased with increasing comonomer (Figure 11c). P-BBT-10, which contains 10% comonomer, resulted in the highest yield of 82% for the oxidative cyclization reaction of *N,N*-dimethylaniline with *N*-phenylmaleimides in air and room temperature. Addition of KI as a hole scavenger or benzoquinone as a radical scavenger resulted in lower yields, indicating that both the photogenerated electron and hole play a critical role in the photocatalytic cycle.<sup>130</sup>

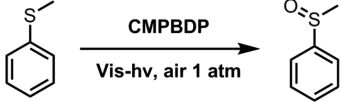
Zhang et al. reported a thiophene-based CTF as a pure organic and visible light-active photoredox catalyst for selective oxidation of alcohols at room temperature, using molecular oxygen as a clean oxidant.<sup>166</sup> The presence of thiophene units in the CTF allows for a low HOMO level at +1.75 V versus SCE, resulting in a high photo-oxidation potential. The same group extended this principle for this type of CTF by using asymmetric repeating thiophene-phenyl units linked to the CTF core.<sup>167</sup> This allowed for four different donor–acceptor domains to exist within the network, resulting in enhanced photogenerated charge separation through an intramolecular energy transfer cascade. The asymmetric CTF performed visible light-driven production of benzophosphole oxides from diphenylphosphine oxide and diphenylacetylene with higher efficiency than the symmetric CTF equivalent.

In 2013, we reported the use of Rose Bengal dye-based CMPs as photoredox catalysts in aza-Henry reactions with high conversions and recyclability.<sup>124</sup> Han et al. recently built upon this, reporting the bottom-up synthesis of Eosin Y dye embedded CMPs, EY-POP, for highly efficient photocatalytic dehydrogenative coupling in aza-Henry reactions.<sup>131</sup> Two EY-POPs were prepared, one with a 1,3,5-triethynylbenzene core, EY-POP-1, and a second with a tetra(4-ethynylphenyl)-methane core, EY-POP-2 (Figure 12). Tetrahedral-based CMP, EY-POP-2, had a higher surface area of 718 m<sup>2</sup> g<sup>-1</sup>, compared with EY-POP-1 which contains a C<sub>3</sub> core and surface area of 587 m<sup>2</sup> g<sup>-1</sup>. In spite of the lower surface area of EY-POP-1, the polymer performed better as a photoredox catalyst. The result was prescribed to the extended  $\pi$ -conjugation present in EY-POP-1 which does not exist in EY-POP-2.<sup>131</sup>

Liras and co-workers developed a CMP based on boron-dipyrromethene (BODIPY) dye (CMPBDP) which shows luminescent properties and is used as a photoredox catalyst for

selective oxidations of thioanisoles.<sup>129</sup> CMPBDP was synthesized by Sonogashira–Hagihara cross-coupling reaction between diiodoBODIPY and 1,3,5-triethynylbenzene, resulting in a surface area of 299 m<sup>2</sup> g<sup>-1</sup> and total pore volume of 0.19 cm<sup>3</sup> g<sup>-1</sup>. CMPBDP is highly fluorescent in the solid-state and also with dispersions in 2-ethoxyethanol (2-EE) and DCM. CMPBDP show an absorption maximum at 536 nm. The oxidation of thioanisoles to the corresponding sulfoxides were tested with CMPBDP as a photoredox catalyst using a 500 nm cutoff filter in order to ensure that the radiation was absorbed by BODIPY chromophore and that the UV radiation was filtered. The reaction with 0.1 mol % of CMPBDP yields 99% conversion which is 4-fold faster than its model compounds (BDP1 and BDP2) and can be recycled three times with a TON of 990 (Table 1).<sup>129</sup>

**Table 1. Photocatalyzed Oxidation of Thioanisole to Methylphenyl Sulfoxide Using CMPBDP and Model Compounds**<sup>129</sup>



entry	catalyst	solvent	cat (mol %)	conv (%)	TON
1	CMPBDP	2-EE	0.5	45	90
2			0.1	99	990
3			0.05	26	520
4	BDP1	MeOH	0.1	44	440
5		2-EE	0.1	24	240
6	BDP2	MeOH	0.1	30	300

### 3.5. Light Emission

Luminescent materials can be prepared with CMPs due to their extended  $\pi$ -conjugation properties. As CMPs contain interlocked, rigid building blocks, the restriction of rotation for phenyl rings avoids fluorescent quenching which is readily seen in linear polymers.

In 2011, we show that the band gap of CMPs are tunable, thus the luminescent properties can be controlled with CMPs.<sup>44</sup> This was reported with pyrene-based CMPs through couplings of 1,3,6,8-tetrabromopyrene (TBrPy) with 1,4-dibromobenzene (DB) and/or 4,4'-dibromobiphenyl (DP) comonomers to produce YPy, YDBPy, YDPPy, and SDBPy with the first letter denoting whether a Yamamoto or Suzuki–Miyaura reaction was used (Figure 13a). The networks showed varying surface areas but all show strong solid state fluorescence with emission colors ranging from red (YPy) to orange (YDPPy) to yellow (YDBPy) to green (SDBPy) (Figure 13b–e). The same colors were observed in suspensions of THF (Figure 13f). The differences were due to varying emissions at 620 nm for YPy, 602 nm for YDPPy, two peaks at 545 and 582 nm for YDBPy, and a single narrow peak at 530 nm for SDBPy (Figure 13g). The band gaps of the CMPs are 1.84 eV for YPy, 1.90 eV for YDPPy, 2.05 eV for YDBPy, and 2.37 eV for SDBPy, indicating the band gap can be tuned with network structure.<sup>44</sup>

Soon after, the Jiang group demonstrated luminescent CMPs using tetraphenylethene (TPE) building blocks.<sup>132</sup> The interlocked network in CMPs restricts rotation of the phenyl groups which usually cause fluorescent quenching in TPE, therefore allowing intrinsic luminescence in TPE-CMP.



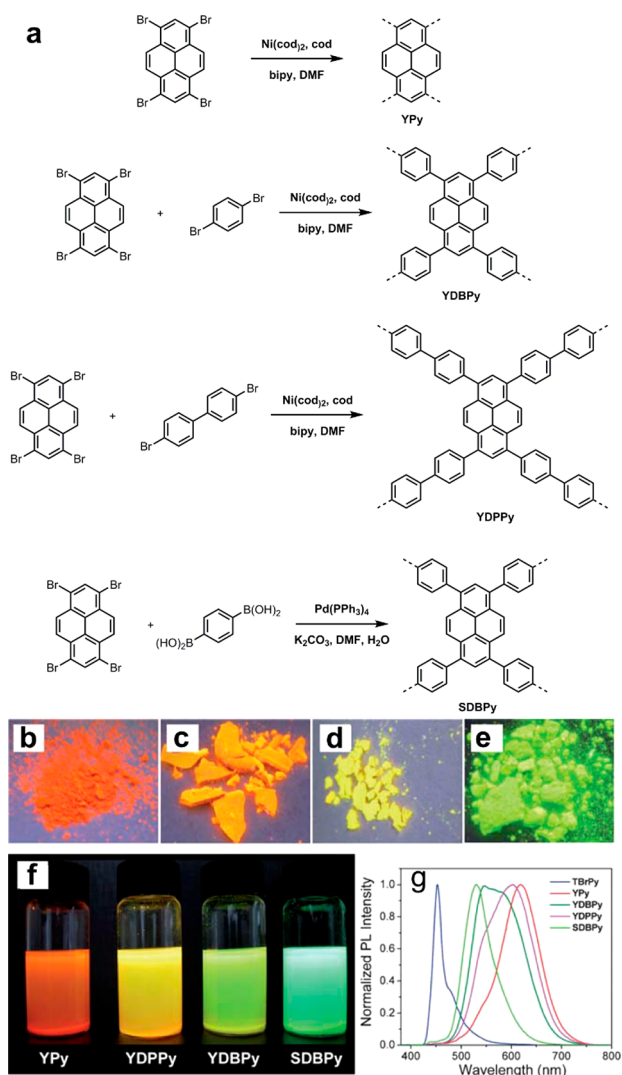


**Figure 13.** (a) Synthesis of luminescent pyrene-based CMPs. Photographs of the CMPs under irradiation with UV light ( $\lambda_{\text{excit}} = 365$  nm) in the solid state, (b) YPy, (c) YDPPy, (d) YDBPy, and (e) SDBPy. (f) Photographs of suspensions of the CMPs in THF (10 mg/10 mL). (g) Photoluminescent spectra of the monomer TBrPy and the resulting polymers measured in solid state powder ( $\lambda_{\text{excit}} = 360$  nm). Reprinted with permission from ref 44. Copyright 2011 The Royal Society of Chemistry.

TPE-CMP after 2 h polymerization emits a yellow emission in the solid state with an absorption band at 342 nm that red-shifts with increasing reaction time up to 368 nm after 72 h. The surface areas were also observed to increase from 753 to 1665  $\text{m}^2 \text{g}^{-1}$  after 2 and 72 h reaction time, respectively. The results suggest that the network grows larger as the polymerization proceeds. TPE-CMP shows strong luminescence in a large variety of solvents such as methanol, dioxane, THF, dichloromethane, chloroform, hexane, DMF, benzene, and water. The CMP shows superior quantum yields compared to the linear polymer analogue, 40%, compared with 0.65% under the same conditions.<sup>132</sup>

Jiang et al. also demonstrated a core-shell strategy for color-tunable light emissions.<sup>49</sup> The method utilized a one-pot two-stage polymerization, initially polymerizing a blue emissive polyphenylene CMP (PP-CMP) core then a yellow emissive polytetraphenylene CMP exterior surface (TPE<sub>s</sub>-PP<sub>c</sub>-CMP)

(Figure 14). The homogeneous PP-CMP showed an absorption band at 312 nm which red-shifts to 531 nm for TPE<sub>s</sub>-PP<sub>c</sub>-CMP. They also investigate the inverse core-shell CMP, PP<sub>s</sub>-TPE<sub>c</sub>-CMP, which shows a similar red-shift. This showed that  $\pi$ -conjugation is readily promoted from across the core to the shell. Fluorescence anisotropy measurements show that the emission is significantly depolarized even when the shell is as thick as 45 nm, indicating efficient exciton migration over the  $\pi$ -conjugated core-shell network.<sup>49</sup>

Triarylboron-containing  $\pi$ -conjugated systems have attracted attention because of their interesting electronic and photophysical properties.<sup>168</sup> The Liu group exploited this idea using triarylboron compounds homocoupled via Sonogashira-Hagihara to produce BCMP-1 with a BET surface area of 815  $\text{m}^2 \text{g}^{-1}$  and BCMP-2 which cross-couples triarylboron with triarylamine to yield a network with a BET surface area of 911  $\text{m}^2 \text{g}^{-1}$ .<sup>133</sup> The absorption band of BCMP-1 at 400 nm is red-shifted by 58 nm compared with its monomer. BCMP-2 shows a broad absorption profile with a main peak situated at 430 nm and a shoulder peak at 345 nm. BCMP-1 emits a light sky-blue emission with a strong fluorescent band at 483 nm, whereas BCMP-2 emits yellow with a fluorescent emission band at 558 nm. The fluorescence spectra of BCMP-2 was also studied in various solvents with an emission frequency appearing at 528 nm in toluene, 541 nm in chloroform, and 562 nm in acetonitrile, which indicates a highly polarized excited state.<sup>133</sup>

Guo and co-workers controlled fluorescence tuning over the whole visible spectrum, including emission of pure white light by immobilization of dye within the micropores of a CMP film.<sup>134</sup> They utilize a two-step polymerization by initially forming tetraphenylethene-based (TPE) hyperbranched polymer particles (HPPs) by Sonogashira-Hagihara coupling in a toluene-in-water mini-emulsion to form particles with a certain size but absent from permanent micropores. Microporosity was added to HPPs by treating them under solvothermal conditions to convert them to nanoscale CMPs (NCMPs). The two-step method, which maintains uniformity and regularity of NCMP size and morphology, gave rise to intrinsic porosity yielding surface areas of up to 1214  $\text{m}^2 \text{g}^{-1}$  for TPE-NCMP-4. TPE, TPE-HPP, and TPE-NCMP-4 dispersed in a mixture of THF and water (1/9, v/v) and excited at 340 nm show maximum emission peaks are red-shift from 480 to 500 to 520 nm, respectively, corresponding to the increase in conjugation with NCMPs. The fluorescence quantum yield in THF,  $\Phi_{\text{soln}}$ , calculated using Rhodamine 6G are relatively low reaching 0.03, 1.03, and 3.25% for TPE, TPE-HPP, and TPE-NCMP-4, respectively. The  $\Phi_{\text{soln}}$  of TPE-NCMP-4 is roughly 10 times larger than that of its monomer due to the lesser rotatable phenyl rings of TPE in NCMP that can limit the energy loss through the channel of nonradiative relaxation. The solid-state quantum yield of TPE-NCMP-4 was 58.0%. A donor-acceptor couple was made by entrapping Nile Red within the NCMPs to allow light energy to be harvested by the TPE units and transferred to the dye. Upon dispersion in water and excitation at 380 nm, it was observed that the emission maxima of TPE-NCMP-4 at 518 nm reduced with increasing dye concentration accompanied by an enhancement in the 550–590 nm window. TPE-NCMPs can be created into films by blending with poly(vinyl alcohol). The fluorescence of these films could then be tuned by the doping of red-emitting dye, Phloxine B (PhB), at concentrations of 0.1–0.4 mg/g (Figure 15a). The broad fluorescence spectrum of TPE-NCMPs ranging from 450 to 650 nm overlapped with absorption of

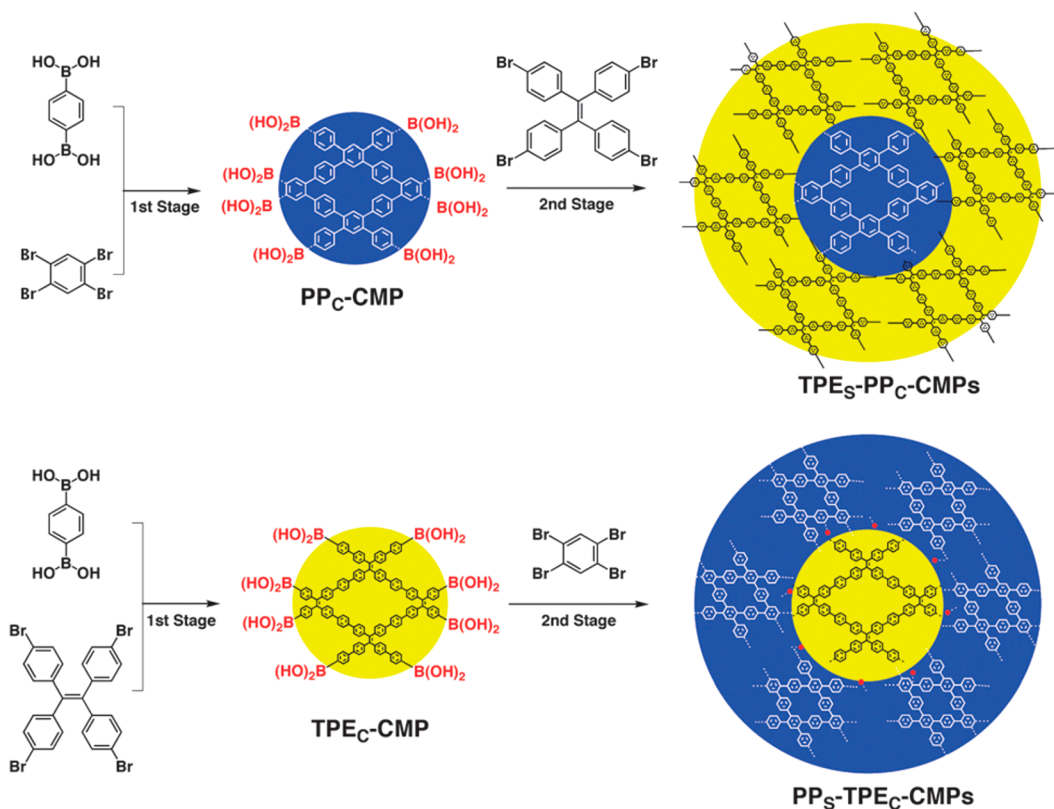


Figure 14. Synthesis of core–shell structured CMPs. Reprinted with permission from ref 27. Copyright 2013 The Royal Society of Chemistry.

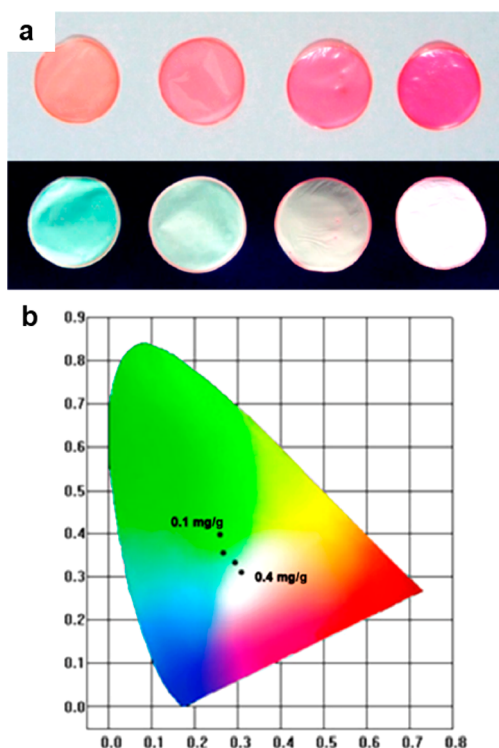


Figure 15. (a) Photographs of TPE-NCMPs films by blending with poly(vinyl alcohol). (b) Emission colors from CIE 1931 chromaticity diagram calculated from the fluorescence spectrum of various doping levels of PhB in TPE-NCMP films. Reprinted from ref 134. Copyright 2014 American Chemical Society.

PhB. Thus, the green light emission of TPE-NCMP is gradually quenched with increasing PhB concentration, which strongly emits colors ranging from green to white under UV irradiation (365 nm) (Figure 15b).<sup>134</sup>

We developed a method to fine-tune the optical band gap and the emission of CMPs by addition of a small amount of acceptor dopant comonomer as a chromophore in the network.<sup>135</sup> CP-CMP0, synthesized from the Suzuki-Miyaura coupling of tetrabromobenzene and benzene-1,4-diboronic acid, was chosen as a native polymer which shows strong blue fluorescence emission when undoped. By polymerization with small amounts of acceptor comonomers such as benzothiadiazole (BT), bistiophenebenzothiadiazole (TBT), and perylene-diimide (PDI) between 0.1–5 mol %, the fluorescence can be changed with emission in the solid state ranging from 445 to 655 nm (Table 2). The optical band gap of the CMPs could be tuned between 1.85 and 2.95 eV. A white-emitting CMP was designed by combining blue (CP-CMP0), green (BT), and red fluorescence (TBT) in a single material by combined polymerization in the feed ratio of 0.028 TBT: 0.1 BT, to produce CP-CMPw11. CP-CMPw11 in the solid state shows a fluorescence quantum yield of 8.8% and BET surface area of 580 m<sup>2</sup> g<sup>-1</sup>, reducing the level of aggregation, thus allowing a relatively high quantum yield. The polymer dispersion excited at 360 nm gave the International Commission on Illumination (CIE) coordinates (0.25, 0.30).<sup>135</sup>

### 3.6. Chemosensors

The luminescent properties of CMPs which arise from their extended  $\pi$ -conjugation can be used for the detection of various chemicals by quenching of the fluorescence. CMPs have advantages over nonporous conjugated polymers as the

**Table 2.** Acceptor Monomer Feed Ratios of CP-CMPs with Resultant Surface Areas, Optical Band Gaps, And Fluorescence and Emission Amplifications<sup>135</sup>

polymer CP-CMP	acceptor (mol %)	S <sub>A</sub> <sup>BET</sup> (m <sup>2</sup> g <sup>-1</sup> )	optical band gap (eV) <sup>a</sup>	λ <sub>emission</sub> (nm) solid state	λ <sub>emission</sub> (nm) PEG dispersion	amplification in solid state I <sub>AD</sub> /I <sub>A</sub>	amplification in PEG dispersion I <sub>AD</sub> /I <sub>A</sub>	quantum yield (%) <sup>b</sup>
0		660	2.95	445	436			13.4
3a	BT (0.1)	731	2.59	506	430, 502	0.92	6.42	
3b	BT (0.5)	592	2.52	513	510	0.64	2.15	
3c	BT (1)	307	2.50	515	512	0.61	3.86	7.1
3d	BT (2)	634	2.48	518	515	0.59	1.98	
3e	BT (3)	506	2.42	524	515	0.48	1.15	
3f	BT (5)	547	2.41	524	519	0.49	1.05	
4a	TBT (0.1)	543	2.07	419, 586	429, 595	0.11	1.81	
4b	TBT (0.5)	459	2.04	416, 603	422, 605	0.07	0.84	
4c	TBT (1)	544	2.00	415, 611	416, 610	0.06	0.62	1.82
4d	TBT (2)	540	1.98	621	416, 612	0.04	0.40	
4e	TBT (3)	287	1.97	626	413, 613	0.03	0.29	
4f	TBT (5)	459	1.95	630	415, 621	0.03	0.20	
5a	PDI (0.1)	693	1.96	450, 590	440	0.07		
5b	PDI (0.5)	650	1.94	424, 618	424	0.042	2.02	
5c	PDI (1)	637	1.90	451, 633	421, 613	0.041	1.22	1.29
5d	PDI (2)	656	1.88	641	417, 627	0.037	0.96	
5e	PDI (3)	583	1.87	649	408, 630	0.036	0.27	
5f	PDI (5)	563	1.85	655	414, 636	0.026	0.49	
LP0			2.81	450	453			0.43
LP3	BT (1)		2.38	522	398, 520	0.43	4.37	0.94
LP4	TBT (1)		1.90	448, 624	400, 612	0.14	1.14	0.15
LP5	PDI (1)		1.85	577, 643	400, 638	0.13	0.33	0.56

<sup>a</sup>Calculated from the onset of the absorption spectrum in solid state. <sup>b</sup>The absolute quantum yields were estimated using Wrighton–Ginley–Morse's method.

large open sites in CMPs allow more interactions with chemicals, thus providing enhanced signal sensitivities.

Jiang et al. reported the first CMP sensor with the use of a carbazole-based TCB-CMP to detect arene vapors by taking advantage of its porous,  $\pi$ -conjugated, and photoluminescence properties.<sup>48</sup> TCB-CMP exhibits blue luminescence and an emission band at 468 nm with a quantum yield of 10% upon excitation at 368 nm. The fluorescence of TCB-CMP is quenched upon exposure to 2,4-dinitrotoluene, 2-nitrotoluene, nitrobenzene, or 1,4-benzoquinone vapors (Figure 16). They also showed that the network with a BET surface area of 1280 m<sup>2</sup> g<sup>-1</sup> and pore volume of 0.923 cm<sup>3</sup> g<sup>-1</sup> possessed enhanced sensitivities compared to its linear analogue. Interestingly, the level of fluorescence responded to the electron density of the arene detected, with prominent enhancement observed with electron-rich vapors and drastic quenching seen with electron-poor vapors. The large surface areas of TCB-CMP aid in maximizing the interface for arene absorption.<sup>48</sup>

Novotny and Dichtel developed various CMPs for detection of 2,4,6-trinitrotoluene (TNT) vapor via fluorescence quenching.<sup>136</sup> The polymers were synthesized through a Sonogashira–Hagihara cross-coupling reaction with the solvent choice and activation procedures optimized with DMF and freeze-drying, yielding various surface areas of up to 259 m<sup>2</sup> g<sup>-1</sup> which also gave the highest sensitivity to the TNT vapors. A  $\pi$ -electron rich unit containing 4-dialkoxybenzene subunits was chosen because of its electronic complementarity to TNT. The CMPs prepared as films show strong absorption out to ~450 nm which was expected for a *m*-polyphenyleneethynylene network. Local  $\lambda_{\text{max}}$  were observed at 325 and 380 nm for polymerizations in DMF and 300 and 370 nm in toluene which indicated an increased degree of conjugation in the DMF

polymers. This was consistent with the increased TNT sensitivity they observed with the DMF synthesized polymers which was concluded due to the longer excitation diffusion lengths in the DMF films.<sup>136</sup>

Liang and co-workers produced a series of porous polymers utilizing the Heck reaction of 1,3,5-tri(4-ethenylphenyl)benzene (TEPB) with 1,3,5-tri(4-iodophenyl)benzene to produce LMOP-1, an amine core equivalent (4-iodophenyl)amine to produce LMOP-2, and tetrahedral tetrakis(4-bromophenyl)methane to produce LMOP-3 (Figure 17).<sup>79</sup> TEPB monomer shows a bright blue emission at 450 nm when excited at 325 nm at the solid state. Excitation of LMOP-1 exhibits a broad emission at 475 nm, LMOP-2 at 515 nm, and LMOP-3 at 458 nm. Suspensions of LMOP-2 and LMOP-3 in THF showed blue-shifted emissions compared to the solid state. Addition of picric acid was observed to quench emissions of the LMOPs, with LMOP-3 able to be regenerated and reused for at least five cycles.<sup>79</sup> The group later developed additional LMOPs with tunable luminescence, emitting blue to green to yellow light depending on the comonomer ratio during synthesis. The optimized LMOP was used to sense picric acid for up to five cycles.<sup>80</sup>

Recently, Wang et al. synthesized a carbazole-based CMP synthesized by palladium-catalyzed Sonogashira–Hagihara cross-coupling of 1,3,6,8-tetrabromo-9*H*-carbazole and 1,4-diethynylbenzene monomers both in polymeric network form (DCZP) and as porous nanoparticles (DCZN) which were used as sensors for picronic acid.<sup>138</sup> The network has a BET surface area of 688 m<sup>2</sup> g<sup>-1</sup> and pore volume of 0.429 cm<sup>3</sup> g<sup>-1</sup>, while synthesizing the nanoparticles in emulsion yields a reduced surface area and pore volume of 97 m<sup>2</sup> g<sup>-1</sup> and 0.149 cm<sup>3</sup> g<sup>-1</sup>, respectively. DCZN showed strong fluorescent



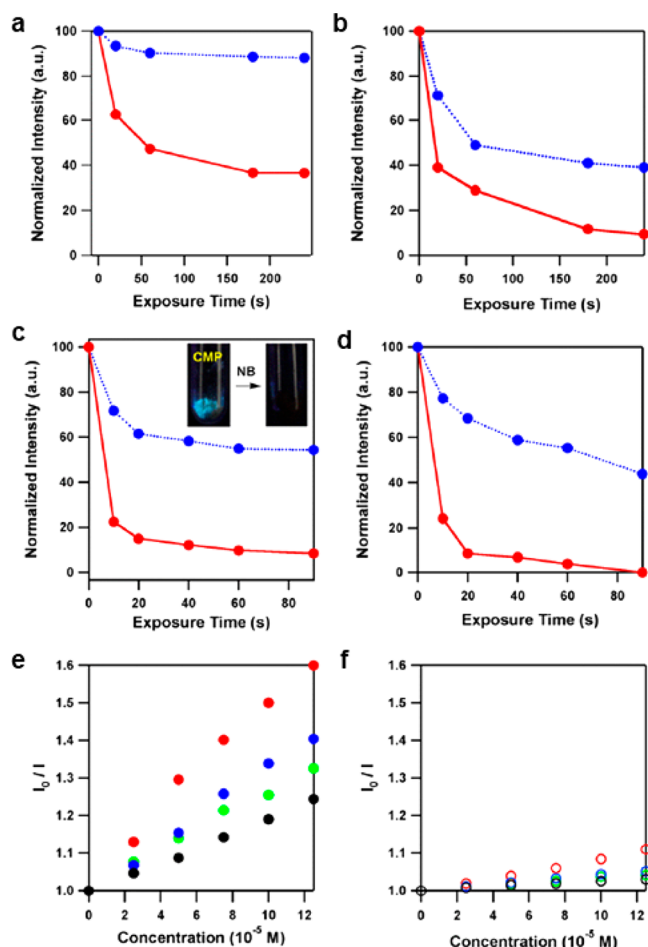


**Figure 16.** Fluorescence quenching of TCB-CMP (red) and its linear analogue (blue) at 25 °C upon exposure to vapors of (a) 2,4-dinitrotoluene, (b) 2-nitrotoluene, (c) nitrobenzene, or (d) 1,4-benzoquinone vapors. Inset in (c): luminescence images of TCB-CMP in the presence and absence of nitrobenzene under a hand-held UV lamp. Reprinted from ref 48. Copyright 2012 American Chemical Society.

emission by excitation at 365 nm in THF suspension and exhibits a higher sensitivity to picronic acid than the polymeric form, suggesting that considerations to the dispersive medium is important.<sup>138</sup>

The Liu group reported a triarylboron-linked CMP, BCMP-3, capable of sensing and removing fluoride ions.<sup>137</sup> The network synthesized through a Suzuki–Miyaura cross-coupling polycondensation of tris(4-bromo-2,6-dimethylphenyl)borane and tris(4-dihydroxyboranylphenyl)amine has a BET surface area of 950 m<sup>2</sup> g<sup>-1</sup> and pore volume of 0.768 cm<sup>3</sup> g<sup>-1</sup> (Figure 18). BCMP-3 displays an intense absorption band with maxima at ~380 nm and strong fluorescence emission, prescribed to efficient charge transfer from the triarylamine donor sites to triarylborane acceptor sites, with an emission band in the solid state at 488 nm and quantum yield of 18% upon excitation at 375 nm. Upon addition of F<sup>-</sup> to a dispersion of BCMP-3 in THF, the solution can be seen to turn slightly paler. The intensity of the absorption band at 278 nm increased while there was a decrease in the nitrogen-to-boron charge-transfer band at 409 nm, interrupting the conjugation of the network by formation of a boron-fluoride complex.<sup>137</sup>

### 3.7. Energy Storage

CMPs possess microporosity and extended  $\pi$ -conjugation which are favorable in electrodes for electrical energy storage. Supercapacitors can store charge by electric double-layer capacitance (EDLC) and pseudocapacitance (PC) mechanisms. EDLC operates by reversible charge accumulation at the electrode–electrolyte interface. PC exploits fast reversible redox reactions of electroactive species. High surface areas from CMPs allow access to many active sites for charge from the electrolyte to be stored upon the surface, important for EDLC. The ease in tunability of CMPs allows redox-active groups to be introduced within the skeleton which can have interesting and beneficial properties during the electrochemistry. Batteries favor similar properties to supercapacitors; however, the redox properties of the material are especially important. Electronic conductivity of CMP materials has been a major issue in this field, but many strategies have been put forward to tackle this.

**3.7.1. Supercapacitors.** In 2011, the Jiang group introduced aza-fused CMPs for supercapacitive energy storage.<sup>46</sup> The CMPs were synthesized at high temperatures between 300 and 500 °C through a phenazine ring fusion reaction using 1,2,4,5-benzenetetramine tetrahydrochloride and triquinoyl hydrate, in the presence of AlCl<sub>3</sub> in an evacuated ampule (Figure 19a). The N-rich, black CMP powder possesses BET surface areas from 24 to 1227 m<sup>2</sup> g<sup>-1</sup> with increasing temperature. The materials are conductive, with the aza units aiding in dipolar interactions with the electrolyte cations thus supporting proton accumulation on the surface, while the porosity aids in electrolyte diffusion and provides a large surface for EDLC. The CV profiles show a diagonal shape, especially at higher scan rates of up to 200 mV s<sup>-1</sup>, with the current proportionately increasing with the shift in electrode potential in both the positive and negative sweeps over the whole potential range, which can be associated with high electric resistance of the Aza-CMPs (Figure 19b,c).<sup>169</sup> The highest capacitance reported was at 946 F g<sup>-1</sup> for Aza-CMP@450 from galvanostatic charge–discharge experiments at a current density of 0.1 A g<sup>-1</sup> (Figure 19d). However, the group only showed charge–discharge curves at current densities between 0.2 and 10 A g<sup>-1</sup> but not at 0.1 A g<sup>-1</sup>, so it is difficult to conclude how much capacitance may come from irreversible decomposition reactions at low current densities considering the large jump in capacitance from 0.2 to 0.1 A g<sup>-1</sup> in the aza-CMPs. It was noted that Aza-CMP@500 resulted in a lower capacitance due to the smaller pores in the structure, which could not retain capacitance, especially at higher current densities of 5 and 10 A g<sup>-1</sup>. Aza-CMP@300 showed excellent supercapacitive stability with no loss of capacitance after 10000 charge–discharge cycles at a current density of 5 A g<sup>-1</sup>.<sup>46</sup>

Feng et al. demonstrated a graphene-based CMP as a supercapacitor.<sup>139</sup> The method utilizes reduced graphene oxide (RGO) as a structure to polymerize CMPs onto by Sonogashira–Hagihara cross-coupling to create 2D CMPs. The strategy combines the 2D templating of RGO with the porosity and functionality of CMPs into the material. Different heteroatoms were introduced into the material with thiophene-, thiazole, and pyridine-containing polymers and pyrolyzed to introduce electrical conductivity producing GMC-S, GMC-NS, and GMC-N, respectively. GMC-NS and GMC-N had a sulfur weight content of 7.7 and 5.9%, respectively, and GMC-NS and GMC-N had a nitrogen

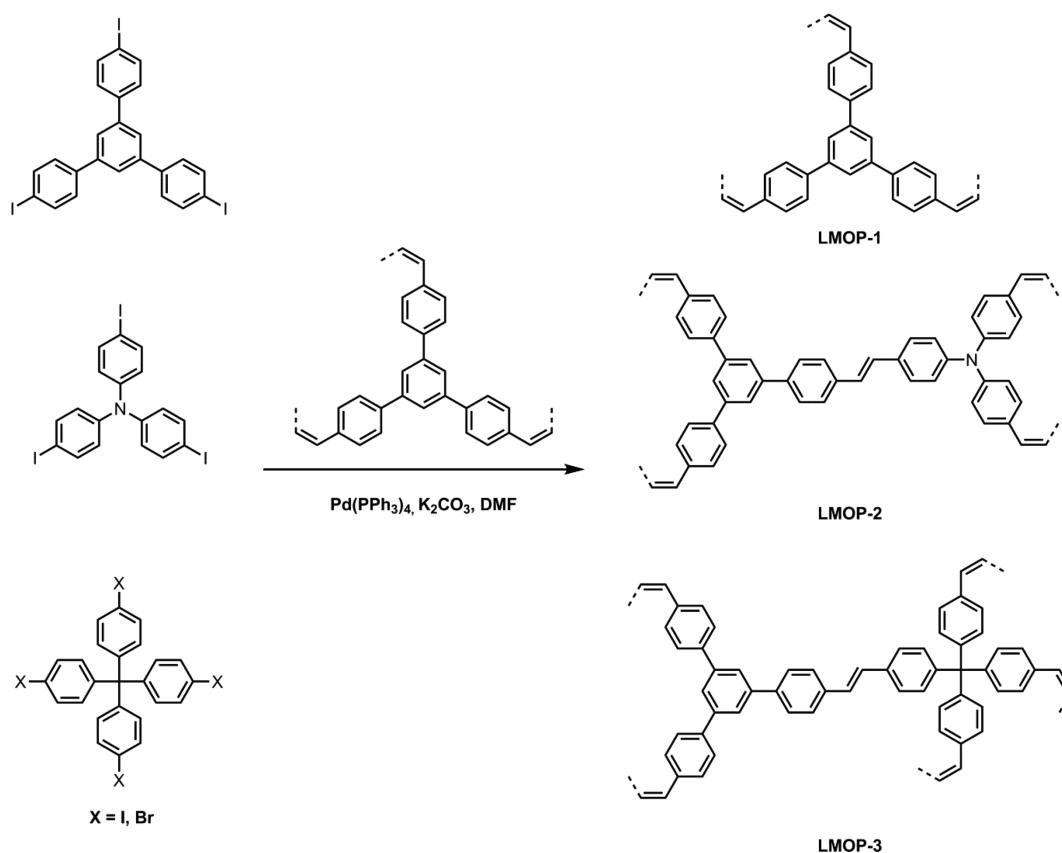


Figure 17. (a) Synthesis of LMOPs by the Heck reaction.<sup>79</sup>

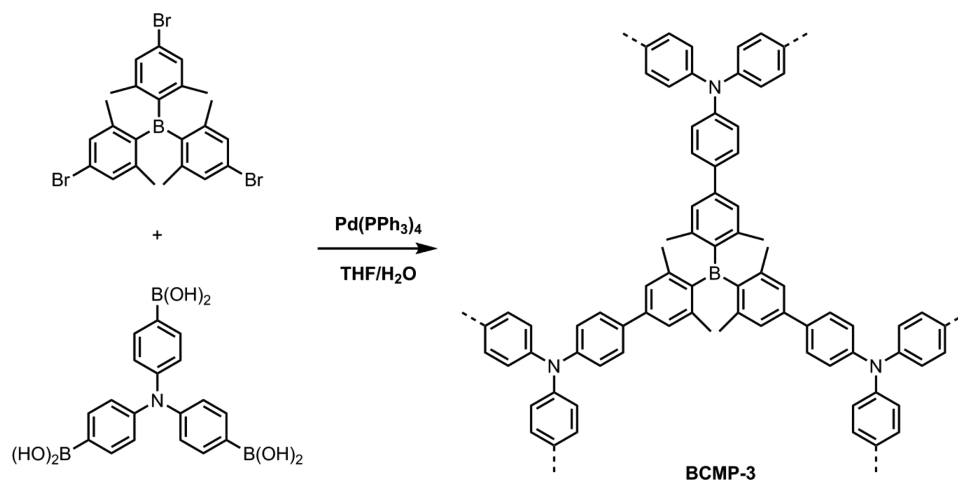
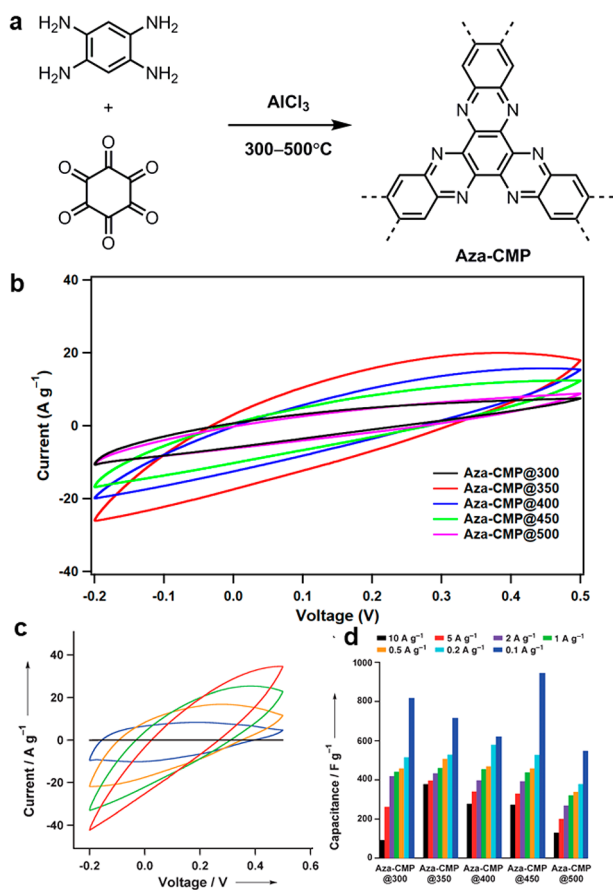


Figure 18. Synthesis of triarylboron-linked CMP, BCMP-3.<sup>137</sup>

content of 3.0 and 3.8%, respectively, with a BET surface area ranging from 560 to 681  $\text{m}^2 \text{g}^{-1}$ . The materials show traditional quasi-rectangular CV shapes associated with good reversible supercapacitor behavior. Galvanostatic charge–discharge experiments yielded specific gravimetric capacitances of 244–304  $\text{F g}^{-1}$  at 0.1  $\text{A g}^{-1}$  for the GMCs, which is 14–35% higher than without the graphene template.<sup>139</sup>

Ma and co-workers report an electropolymerization approach to producing CMP films on electrodes with supercapacitive properties.<sup>104</sup> Zinc porphyrin-carbazole-based CMP films were synthesized onto indium tin oxide (ITO) electrodes by CV of Zn(II)-5,10,15,20-tetrakis[(carbazol-9-yl)phenyl]porphyrin (Zn-mTCPP) in  $\text{CH}_2\text{Cl}_2$  between a

potential range of 0–1.4 V (Figure 20a,b). The tetrahedral configuration of the monomer provides high surface areas and facilitate ion transportation in combination with redox-active sites to behave as a PC electrode. The film thickness increased with increased scans (Figure 20c), and the thickness of a few tens of nanometers were calculated using impedance spectroscopy from Nyquist plots. The CMP film of 38 nm thickness exhibits two reversible redox processes in CV at about 0.9 and 1.2 V associated with the reversible redox process of zinc tetraphenylporphyrin and dimeric carbazole units when run between –0.4 and 1.4 V (Figure 20d). A maximum capacitance of 142  $\text{F g}^{-1}$  was obtained at current density of 5  $\text{A g}^{-1}$ . Interestingly, the film shows excellent capacitance retention



**Figure 19.** (a) Synthesis of Aza-fused CMPs by high temperature phenazine ring fusion reaction in an ampule. (b) Cyclic voltammograms of Aza-CMPs at a scan speed of  $100 \text{ mV s}^{-1}$ . (c) Cyclic voltammogram of Aza-CMP@300 at a scan rate of 25 (blue), 50 (orange), 100 (green), and  $200 \text{ mV s}^{-1}$  (red), and hexaazatriphenylene (HAT) at a scan rate of  $100 \text{ mV s}^{-1}$  (black). (d) Capacitance of Aza-CMPs at varying current densities. Adapted with permission from ref 46. Copyright 2011 Wiley-VCH.

remaining at 70% at a high current density of  $50 \text{ A g}^{-1}$ . There is promise to electropolymerize these materials onto flexible conducting substrates such as ITO-coated polyethylene terephthalate (PET-ITO) films to produce flexible supercapacitor devices.<sup>104</sup>

Pristine CMP electrodes suffer from poor electrical conductivity which limits the material in electrochemical applications. We reported a pyrolysis method in combination with a nitrogen dopant gas to produce CMP electrodes with both EDLC and PC functionalities that retain morphology and porosity properties.<sup>143</sup> The wide feasibility was demonstrated with CMP-1 which was pyrolyzed under inert gas, ammonia gas, and a combination of the two. The surface areas of pyrolyzed CMP under inert gas remain mostly unchanged while under ammonia increases were observed from CMP-1 with a BET surface area of  $692 \text{ m}^2 \text{ g}^{-1}$  to up to  $1436 \text{ m}^2 \text{ g}^{-1}$  in N3-CMP-1 which uses a combination of pyrolysis under inert gas then postpyrolysis under ammonia. The increase in surface area was due to the activation nature of ammonia. While the surface areas of the materials varied, all pyrolyzed CMP-1 products, both under inert and/or ammonia gas, show a primary pore size at  $\sim 11 \text{ \AA}$ , shifted from CMP-1 which has a primary pore size at  $\sim 13 \text{ \AA}$  (Figure 21a). The  $\sim 2 \text{ \AA}$  decrease in pore size was attributed to further micropore development

upon pyrolysis. An amine-functionalized CMP, CMP-1-NH<sub>2</sub>, was also pyrolyzed under inert gas and saw a shift in pore size from  $\sim 16$  to  $14 \text{ \AA}$ . This showed that the pore size could essentially be controlled relative to the original CMP pore size, while the products also retained their original morphology. CVs show a quasi-rectangular plot for N3-CMP-1, associated with good EDLC behavior with additional peaks observed for redox-active N-groups in the materials contributing to PC (Figure 21b). The hybrid supercapacitor maintains a quasi-rectangular CV even at scan rates of  $1000 \text{ mV s}^{-1}$  (Figure 21c), while retaining 74% capacitance. Basic KOH electrolyte was found to perform best with N3-CMP-1, attributed to higher PC contributions of 15.2% compared with H<sub>2</sub>SO<sub>4</sub> of 14.3%, with Galvanostatic charge–discharge showing capacitances as high as  $260 \text{ F g}^{-1}$  at  $0.1 \text{ A g}^{-1}$ . The material showed no signs of degradation after 10000 cycles but displays an increase in capacitance due to progressive wetting of a small fraction of less accessible and therefore previously occluded pores (Figure 21d).<sup>143</sup>

Up to now, CMP-based supercapacitors have utilized high temperature synthesis or electropolymerization. In 2016, Wei et al. reported the microwave synthesis of an amorphous  $\beta$ -ketoenamine-linked CMP (KECMP-1) for supercapacitors.<sup>142</sup> KECMP-1 was synthesized by a one-pot microwave-assisted Schiff-base condensation of *m*-phenylenediamine and 1,3,5-triformylphloroglucinol at  $150 \text{ }^\circ\text{C}$  for 2 h (Figure 22). KECMP-1 is microporous, with a surface area of  $484 \text{ m}^2 \text{ g}^{-1}$ , and was shown to be chemically stable under various solvents including hexane, methanol, THF, *o*-DCB, DMF, water, 9 M HCl, or 9 M NaOH. The material undergoes reversible redox processes, with two oxidation peaks appearing at 0.1 and 0.2 V; correspondingly two reduction peaks appear at 0.18 and 0.3 V when run between a  $-0.2$  to  $0.8 \text{ V}$  potential window. However, the peak to peak separations indicate a relatively slow heterogeneous charge propagation within the glassy carbon electrode attributed to poor conductivity of the CMP architecture. A specific capacitance of  $252 \text{ F g}^{-1}$  was yielded at a current density of  $1 \text{ A g}^{-1}$  in H<sub>2</sub>SO<sub>4</sub> electrolyte and retains 50% capacitance at a  $200 \text{ A g}^{-1}$ . KECMP-1 shows an increase in capacitance after 10000 cycles due to expansion of the pore diameter. Rapid ion transport rates of the material were showed by fast frequency responses from impedance spectroscopy.<sup>142</sup>

The Huang group designed triazatruxene-based CMPs (TAT-CMPs) that show promising supercapacitive properties.<sup>145</sup> Triazatruxene (TAT) is a C<sub>3</sub> symmetry unit selected for its nitrogen-rich feature and large  $\pi$ -conjugated planar structure which are beneficial to increasing the electrical conductivity. TAT-CMPs were synthesized by a condensation reaction under solvothermal conditions at  $120 \text{ }^\circ\text{C}$  for 3 days. TAT-CMP-1, synthesized from TAT and pyromellitic dianhydride, had a surface area of  $88 \text{ m}^2 \text{ g}^{-1}$ , and TAT-CMP-2, synthesized from TAT and terephthalaldehyde, yielded a surface area of  $106 \text{ m}^2 \text{ g}^{-1}$ . The materials exhibit nearly rectangular CV shapes, due to a combination of a series of successive multiple surface redox reactions occurring over the potential window of  $-1.0$  to  $0 \text{ V}$  versus Hg/HgO, prescribed to PC effects from the multiple nitrogen groups. They found that TAT-CMP-2 showed a higher specific capacitance of  $183 \text{ F g}^{-1}$  at  $1 \text{ A g}^{-1}$  which was in line with a higher nitrogen content for this CMP. TAT-CMP-2 showed 5% capacitance decay after 500 charge–discharge cycles, and



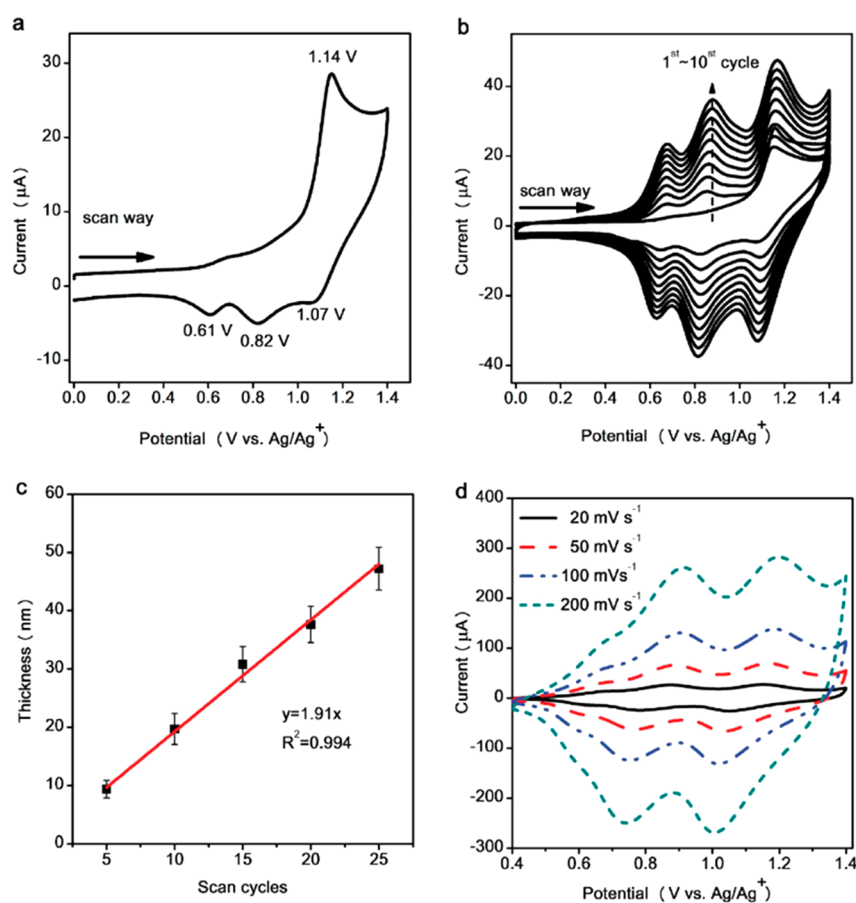


**Figure 20.** (a) First and (b) first to tenth cyclic voltammogram cycle of  $1.5 \times 10^{-5}$  Zn-mTCPP in  $\text{CH}_2\text{Cl}_2$ . (c) Relationship of film thickness with scan cycles. (d) Cyclic voltammogram of CMP film in monomer-free electrolyte at different scan rates. Reprinted with permission from ref 104. Copyright 2015 Wiley-VCH.

then no changes over 10000 cycles at a current density of  $10 \text{ A g}^{-1}$ .<sup>145</sup>

Recently, Liao and co-workers synthesized 3D polyaminoanthraquinone networks via Buchwald-Hartwig with high capacitances of  $576 \text{ F g}^{-1}$  and  $168 \text{ F g}^{-1}$  in three-electrode and two-electrode configurations, respectively.<sup>100</sup> The group coupled a 2,6-diaminoanthraquinone linker with five different aryl bromide cores to yield the CMPs with surface areas between  $331$  and  $600 \text{ m}^2 \text{ g}^{-1}$  (Figure 23a). The CMPs were coated onto carbon paper to produce flexible electrodes and showed redox peaks in the CV ascribed to the pseudocapacitive behavior of the networks (Figure 23b). The network consisting of consisting of anthraquinonylamine and triphenylamine (PAQTA) showed the highest activity, whereas the network containing anthraquinonylamine and triphenylbenzene (PAQTB) showed the lowest activity. The high performance of PAQTA was thought to be linked to the combination of the strong donor (anthraquinonylamine) and acceptor (triphenylamine) which allows for high redox activity (Figure 23c). Asymmetric supercapacitors constructed from PAQTA showed a 97% capacitance retention after 2000 cycles and an energy density of  $60 \text{ Wh kg}^{-1}$ .

**3.7.2. Batteries.** In 2014, the Jiang group showed the first example of a CMP used in Li-ion battery applications.<sup>51</sup> They use a hexaazatrinaphthalene CMP (HATN-CMP) synthesized via Sonogashira cross-coupling polycondensation of 1,4-diethynylbenzene and 2,3,8,9,14,15-hexaiododiquinoxalino[2,3-*a*:2',3'-*c*]phenazine (Figure 24a). The network is redox-

active from the in-built nitrogen units that serves to store energy, bears inherent nanopores that are accessible to lithium ions, and possesses a high surface area to maximize charge dynamics. HATN-CMP has a BET surface area of  $616 \text{ m}^2 \text{ g}^{-1}$  with a micropore surface area of  $433 \text{ m}^2 \text{ g}^{-1}$ , thus 70% of the surface area is microporous. The HATN unit is a six-electron redox active compound. The material used as a cathode in a coin cell exhibited a first discharge capacity of  $147 \text{ mA h g}^{-1}$  from the potential range 1.5 to 4.0 V versus  $\text{Li/Li}^+$ , at a current density of  $100 \text{ mA g}^{-1}$  (Figure 24b). HATN-CMP achieves 71% of the theoretical capacity of  $214 \text{ mA h g}^{-1}$ . Lone HATN monomer exhibited a discharge capacity of  $52 \text{ mA h g}^{-1}$  which is only 56% of the theoretical capacity. This was attributed to the hierarchical porous structure of the CMP which facilitates efficient access of electrolyte ions to the redox-active HATN units. The material was tested to 50 cycles which exhibited a capacity of  $91 \text{ mA h g}^{-1}$ , retaining 62% of the original capacity (Figure 24c). HATN-CMP was more stable than HATN which loses 30% of the original capacity upon 2 cycles. At rapid charge-discharges by testing the HATN-CMP at  $1000 \text{ mA h g}^{-1}$ , the material exhibited a capacity of  $50 \text{ mA h g}^{-1}$ . The Ragone plot shows that the energy density ranges from  $36.5$  to  $106 \text{ Wh kg}^{-1}$  with a power density ranging from  $70$  to  $706 \text{ W kg}^{-1}$ .<sup>51</sup>

Li and co-workers reported a  $\text{MnO/CMP}$  composite which was pyrolyzed to produce a hard carbon composite ( $\text{MnO/PHC}$ ) for Li storage.<sup>140</sup> A poly(phenylene butadiynylene) CMP was used to increase the surface area for access of ions to

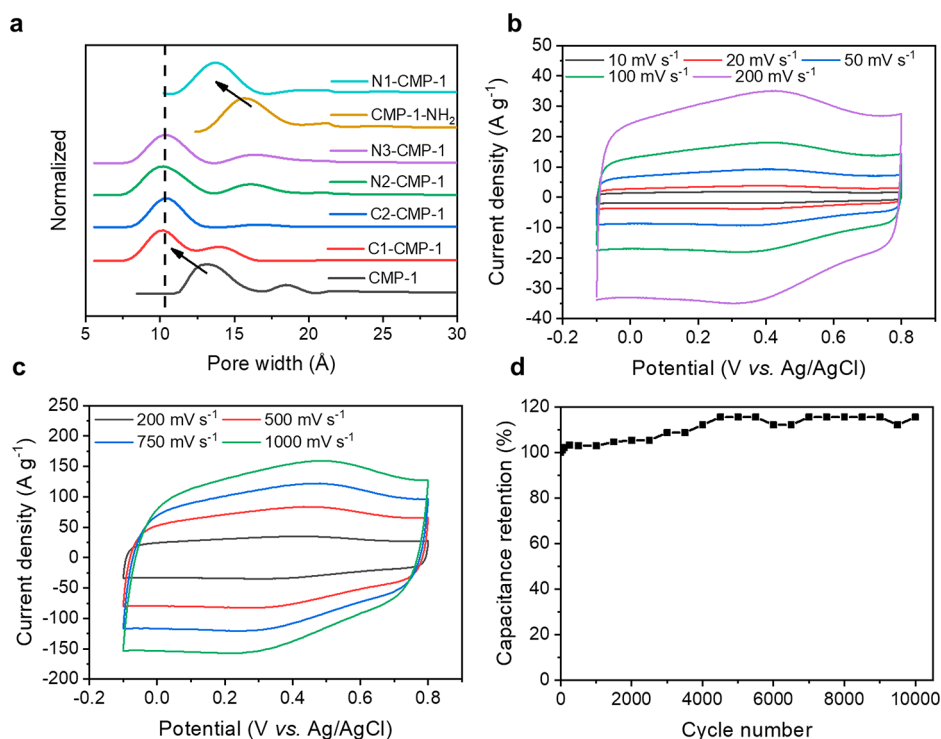


**Figure 21.** (a) Pore size distributions of CMP-1 and pyrolyzed products calculated by NL-DFT. (b) Cyclic voltammograms of N3-CMP-1 at varying scan rates between 10 and 200  $\text{mV s}^{-1}$ . (c) Cyclic voltammograms of N3-CMP-1 at varying scan rates between 200 and 1000  $\text{mV s}^{-1}$ . (d) Cycling stability of N3-CMP-1 at a current density of 5  $\text{A g}^{-1}$ . Adapted with permission from ref 143. Copyright 2016 The Royal Society of Chemistry.

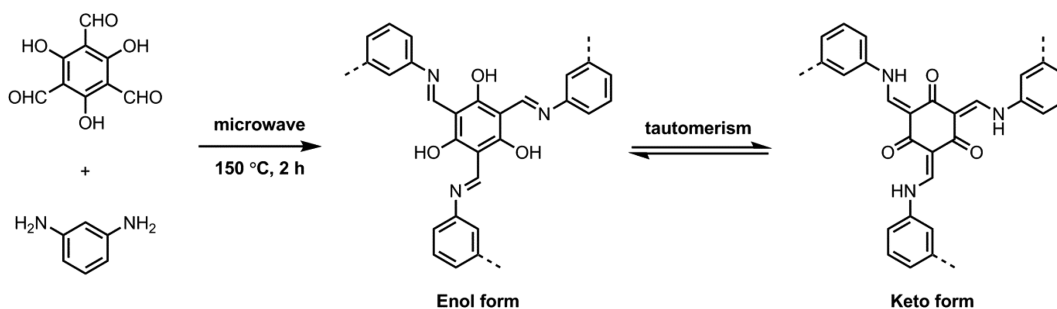


**Figure 22.** Microwave-assisted Schiff-base condensation polymerization of KECMP-1.<sup>142</sup>

MnO, and pyrolysis improved the poor cyclic stability of the MnO anode and decreased their initial irreversible storage capacity. MnO/PHC has a BET surface area and pore volume of  $27.3 \text{ m}^2 \text{ g}^{-1}$  and  $0.77 \text{ cm}^3 \text{ g}^{-1}$ , respectively. The nanocomposite exhibited an initial discharge capacity of  $1104 \text{ mA h g}^{-1}$  at a current rate of 0.2 C. MnO/PHC retains 85% of its initial capacity after 300 charge–discharge cycles at 0.2 C, compared with pristine MnO with only 8.2% of the initial capacity after 150 cycles.<sup>140</sup> The group more recently studied a pyrolyzed MnO/CMP composite in a nanotube morphology which shows a capacity of  $573 \text{ mA h g}^{-1}$  after 300 cycles at 1 C.<sup>144</sup>

Cui et al. reported a carbazole- and thiazole-containing CMP for both Li-ion and Na-ion battery applications.<sup>141</sup> The polymer was synthesized from  $\text{FeCl}_3$  oxidative coupling polymerization of 4,7-dicarbazyl-[2,1,3]-benzothiadiazole (DCzBT) to produce PDCzBT (Figure 25a). The BET surface area and pore volume of PDCzBT was  $1166 \text{ m}^2 \text{ g}^{-1}$  and  $0.7 \text{ cm}^3 \text{ g}^{-1}$ , respectively. When evaluated for Li storage, the CV showed an irreversible band at 1.0 to 0.5 V due to the

electrochemical decomposition of the electrolyte which forms a solid electrolyte interface (SEI) on the electrode surface (Figure 25b). Further scans show that the largest part of the specific capacity ( $>70\%$ ) resides in the region below 0.5 V, corresponding to  $\text{Li}^+$  doping into the polymer chains. Capacity from above 0.5 V was attributed to  $\text{Li}^+$  absorbing on the surfaces/interfaces of PDCzBT. The specific capacity was  $1042 \text{ mA h g}^{-1}$  at a current density of  $20 \text{ mA g}^{-1}$  after 5 cycles (Figure 25c). The value which is higher than other organic materials reported previously to this was attributed to the high specific surface area and inherent homogeneous microporous structure of PDCzBT. PDCzBT delivers a capacity of  $312 \text{ mA h g}^{-1}$  after 400 cycles at  $200 \text{ mA g}^{-1}$  (Figure 25d). The specific capacity was  $\sim 490 \text{ mA h g}^{-1}$  at  $100 \text{ mA g}^{-1}$  and  $\sim 190 \text{ mA h g}^{-1}$  at  $1000 \text{ mA g}^{-1}$  (Figure 25e). Na storage shows similar CV and charge–discharge behavior to Li storage but with lower voltage and capacity due to the larger ionic radius and more sluggish kinetics of  $\text{Na}^+$  than  $\text{Li}^+$ . The polymer exhibited a reversible capacity of  $145 \text{ mA h g}^{-1}$  after 100 cycles at a current density of  $20 \text{ mA g}^{-1}$ . At higher current densities of 50 and 100

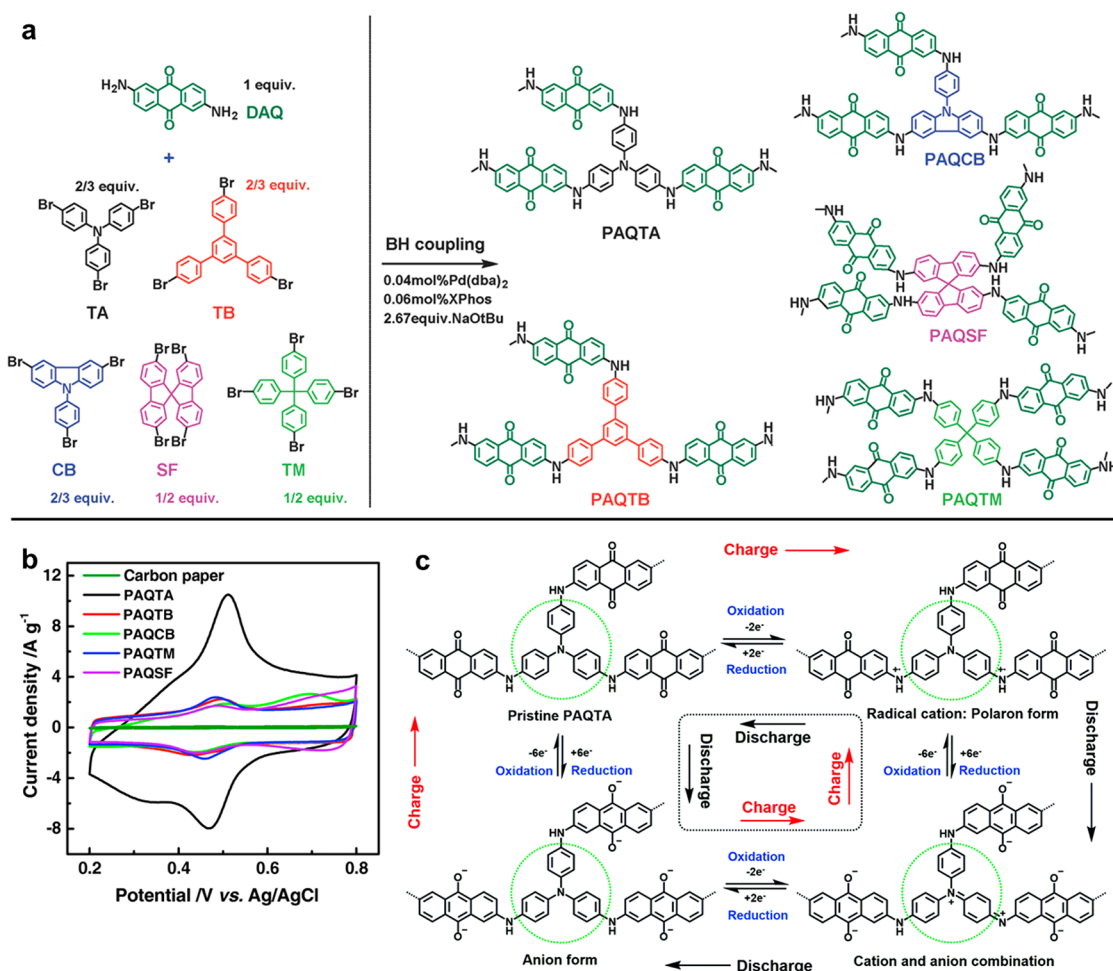


**Figure 23.** (a) Synthesis of polyaminoanthraquinone networks. (b) CV curves of polyaminoanthraquinones in 0.5 M H<sub>2</sub>SO<sub>4</sub> at a scan rate of 10 mV s<sup>-1</sup>. (c) Proposed charge/discharge mechanism of PAQTA. Reprinted with permission from ref 100. Copyright 2018 Wiley-VCH.

mA g<sup>-1</sup>, the capacity was up to 119 and 99 mA h g<sup>-1</sup>, respectively.<sup>141</sup>

Zhang and co-workers applied a structure-design strategy to improve the redox activity in thiophene-containing CMPs in Li-ion batteries.<sup>146</sup> Linear polythiophene and cross-linked poly(3,3'-bithiophene) (P33DT) were synthesized by FeCl<sub>3</sub>-catalyzed oxidative couplings to yield polymers with surface areas of 13 and 696 m<sup>2</sup> g<sup>-1</sup>, respectively (Figure 26). P33DT exhibited a high reversible capacity of 1403 mAh g<sup>-1</sup> for the first cycle of charge, compared to the 745 mAh g<sup>-1</sup> shown by polythiophene. Upon further cycling, P33DT showed a capacity retention of 375 mAh g<sup>-1</sup> at a current density of 5 A g<sup>-1</sup>, whereas polythiophene only exhibited 141 mAh g<sup>-1</sup> at 3 A g<sup>-1</sup>. The results suggest that the cross-linked structure and highly accessible surface area played a key role in the electrochemical performance. Further thiophene polymers synthesized with varying degrees of thiophene content and surface areas supported this.

### 3.8. Biological Applications

Relatively few reports for CMPs in biological applications exist compared with other applications. However, there is potential here for CMPs as they are generally nontoxic, biocompatible, and purely organic, *c.f.*, more widely studied MOFs which may contain heavy metal ions. Currently, CMPs have been utilized in biosensing,<sup>103,147</sup> drug delivery and bioimaging,<sup>148</sup> active singlet oxygen production (1O<sub>2</sub>),<sup>149,150</sup> antibacterial,<sup>151,152</sup> and

phototherapy.<sup>153</sup> Other bioapplications such as DNA detection, enzyme immobilization, and colorimetric immunoassay have yet to be demonstrated using CMPs, however, have been reported with other POPs and recently reviewed.<sup>170,171</sup>

**3.8.1. Biosensing.** In 2014, Jiang et al. electropolymerized a C<sub>3</sub> monomer containing three N-substituted carbazole groups (TPBCz) to produce biosensing TPBCz-CMP films with controllable thickness, high porosity, and uniform pore distribution (Figure 27a).<sup>103</sup> TPBCz-CMP is electron-donating and showed high sensitivity to dopamine (a neurotransmitter and related to a number of important diseases). Immersion of the CMP films in saline solutions of dopamine with a concentration of 10<sup>-5</sup> and 10<sup>-8</sup> M for 20 s resulted in fluorescence quenching by 90% and 50%, respectively (Figure 27b). The CMP films could also be recycled by rinsing with a NaBH<sub>4</sub> solution and deionized water to recover the fluorescence (Figure 27c).

Bhattacharya and co-workers utilized a donor-acceptor CMP (PER@NiP-CMOP-1) for biosensing neomycin (an aminoglycoside antibiotic used in the pharmaceutical industry as a preventive medicine, though highly restricted in humans due to its nephrotoxic and ototoxic effects).<sup>147</sup> PER@NiP-CMOP-1 was synthesized by copolymerization of Ni(II)-containing porphyrin and perylene-based monomers via Suzuki-Miyaura cross-coupling, yielding an insoluble but dispersible material. PER@NiP-CMOP-1 shows a faint blue



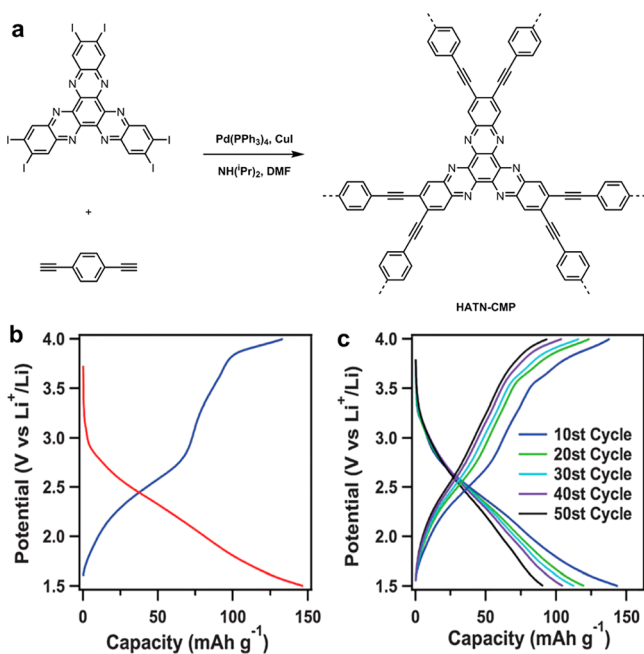


**Figure 24.** (a) Synthesis of redox-active, HATN-CMP. (b) First charge (blue) and discharge (red) profiles of HATN-CMP cell. (c) Charge–discharge profiles of HATN-cell for 50 cycles. Adapted with permission from ref 51. Copyright 2014 The Royal Society of Chemistry.

luminescence in a pH 7.4 buffer due to the extended conjugation with an alternative donor–acceptor arrangement. With the presence of neomycin, a ~62 fold emission intensity enhancement was observed at 440 nm. The emission intensity was found to be linearly dose-dependent and, therefore, can be used for quantification of neomycin even in unknown samples.

**3.8.2. Drug Delivery and Bioimaging.** The Huh group demonstrated drug delivery and bioimaging of cells with nanoscale microporous CTF particles loaded with the anticancer drug, doxorubicin (DOX).<sup>148</sup> The CTF was synthesized via Friedel–Crafts and size reduced to <200 nm via sonication (Figure 28a). The polymer was proved to be nontoxic in nature via a 3-(4,5-dimethylthiazol-2-yl)-2,5-diphenyltetrazolium bromide (MTT) assay, thus suitable to use in cells. The CTF was able to be loaded with water insoluble DOX via physisorption, with a loaded capacity of 200 mg g<sup>-1</sup> due to its high surface area,  $\pi$ – $\pi$  stacking, and hydrophobic interaction. Biotransmission electron microscopy (bio-TEM) was used to observe the effects of the CTF-DOX in cancer cells, HeLa (Figure 28b–d). Figure 28b shows the control image. HeLa when incubated with CTF-DOX shows the material dispersed throughout the cytoplasm (Figure 28c), with the nuclear membrane beginning to degrade, chromosomal material fragmenting, and peroxisomes forming in the cell. However, using only free DOX completely destroys the HeLa cells (Figure 28d).

**3.8.3. Singlet Oxygen Production.** Han et al. demonstrated the first report of <sup>1</sup>O<sub>2</sub> generation using metallophthalocyanine-based CMPs (MPC-CMPs).<sup>150</sup> MPC-CMPs were synthesized by Schiff base chemistry containing M = Co, Ni, Cu, or Zn. UV–vis showed broadening in the long-wavelength region of the CMPs compared to their monomers, and narrowing of the band gap due to the extended  $\pi$ -conjugation, indicating high light-harvesting capability. <sup>1</sup>O<sub>2</sub> was investigated by irradiation of the MPC-CMPs at 700 nm

with a xenon lamp and using 1,2-diphenylisobenzofuran (DPBF) as a trap with monitoring by time-dependent electronic absorption spectroscopy. The absorption band of DPBF in DMF at 410 nm decreases with the presence of MPC-CMPs due to oxidative degeneration by <sup>1</sup>O<sub>2</sub>. MPC-CMPs containing metal ions with open-shell configurations showed lower activities ascribed to influences of the *d*-electrons on their triplet states; thus, ZnPc-CMP showed the highest <sup>1</sup>O<sub>2</sub> generation due to the *d*<sup>10</sup> configuration of the Zn<sup>2+</sup> ion.

Lang and co-workers designed a series of 2D and 3D porphyrin-based CMP which generates <sup>1</sup>O<sub>2</sub> for potential antimicrobial applications.<sup>149</sup> 2D and 3D structures were made by linking porphyrin units with a C<sub>2</sub> linker or a 4-connected tetrahedral unit, respectively. The microporous CMPs allowed for good accessibility of oxygen to the excited porphyrin units, important for the CMPs to act as efficient photosensitizers of <sup>1</sup>O<sub>2</sub>. It was found that the <sup>1</sup>O<sub>2</sub> activity was not directly correlated with porosity but instead the immediate porphyrin environment. Enlarging the porphyrin separation between units leads to higher activity; otherwise most of the absorbed light energy is dissipated by nonradiative processes.

**3.8.4. Antibacterial Materials.** The Zhang group reported a series of photoactive CMP nanoparticles which can inactivate bacteria in water upon visible light exposure.<sup>151</sup> Electron-donating thiophene (Th) and electron-withdrawing benzothiadiazole (BT) linkers of varying ratios were copolymerized with a 1,3,5-triethynylbenzene core using an oil-in-water mini emulsion to create the CMP nanoparticles (Figure 29a). The CMP nanoparticles showed no toxic effects on bacteria cells in the absence of light irradiation. The materials are able to generate <sup>1</sup>O<sub>2</sub>, with Th-BT-100 shown to be the most efficient antibacterial agent of the series, achieving 95% cell death in *E. coli* K-12 and 97% cell death in *B. subtilis* after 120 min visible light irradiation (Figure 29b).

Li et al. recently showed that porphyrin-based CMPs can be combined with antibiotic-free Band-Aids to produce antibacterial Band-Aids for wound disinfection.<sup>152</sup> Under visible light irradiation, the CMPs can produce photothermal heat, in addition to reactive oxygen species to trigger hyperthermia and reactive oxygen species on wounds.

**3.8.5. Phototherapy.** Guo and co-workers synthesized photothermal nanoscale CMP capsules for the thermal ablation of cancer cells.<sup>153</sup> Three kinds of cross-linked poly(methacrylic acid) (PMAA) microspheres were used as sacrificial templates onto which to polymerize CMP-1 (Figure 30), creating microporous and hollow poly(aryleneethynylene) shells in a single step. The shell thickness was able to be tuned from 30 to 140 nm by varying the feeding amount of PMAA particles, with a particle size remaining around 500 nm. The photothermal conversion effect was confirmed by UV–vis of the samples in phosphate-buffered saline solution (PBS), with a broad absorption observed covering the visible and near-infrared windows, implying high levels of conjugation. Exposure of the dispersed CMP shells in PBS solution to a 808 nm near-infrared laser at a power density of 5 W cm<sup>-2</sup> resulted in an increase in temperature of 24 °C in 6 min. It was found that a rough surface allowed for generation of more heat, explained by enhanced scattering effectiveness. The CMP shells showed no significant cytotoxic effect to HeLa cells and are able to destroy the cells in vitro upon irradiation by near-infrared light.

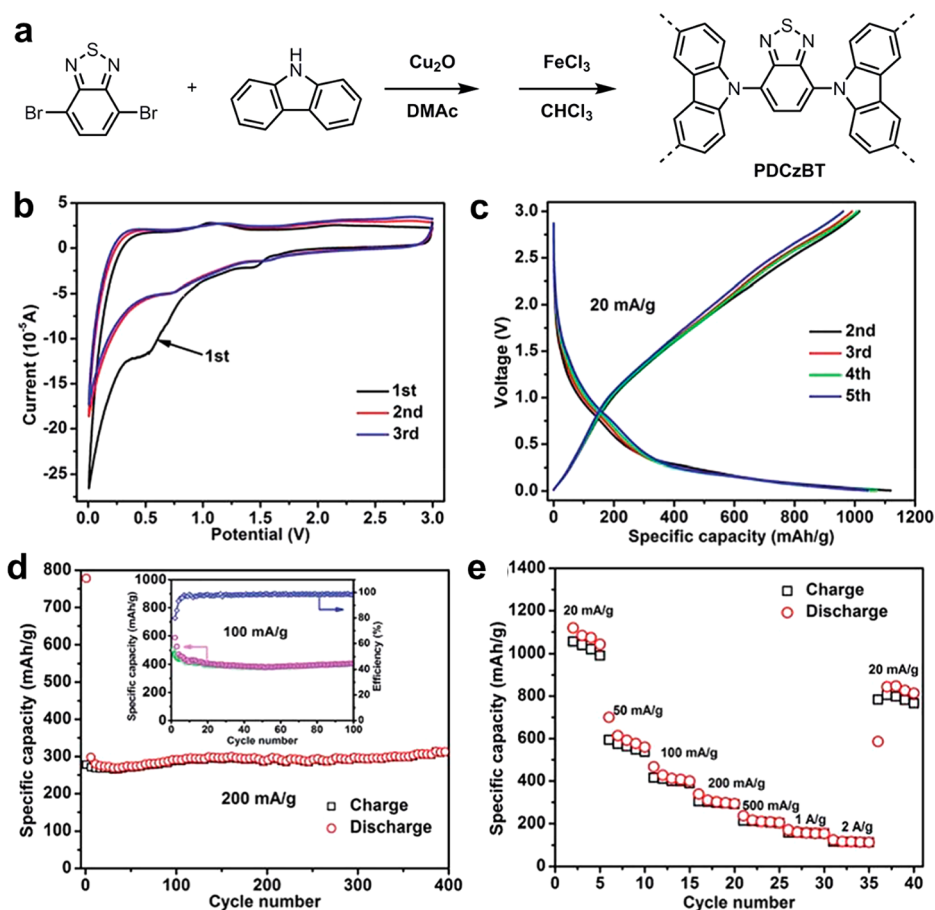


**Figure 25.** (a) Synthesis of redox-active, PDCzBT. Electrochemical performance of PDCzBT for lithium-ion batteries: (b) cyclic voltammogram profiles. (c) Charge–discharge profiles at a current density of  $20 \text{ mA g}^{-1}$ . (d) Cycling performance at a current density of  $200 \text{ mA g}^{-1}$  (inset is cycle performance and Coulombic efficiency at  $100 \text{ mA g}^{-1}$ ). (e) Rate performance at current densities from 20 to  $2000 \text{ mA g}^{-1}$ . Reprinted with permission from ref 141. Copyright 2015 The Royal Society of Chemistry.

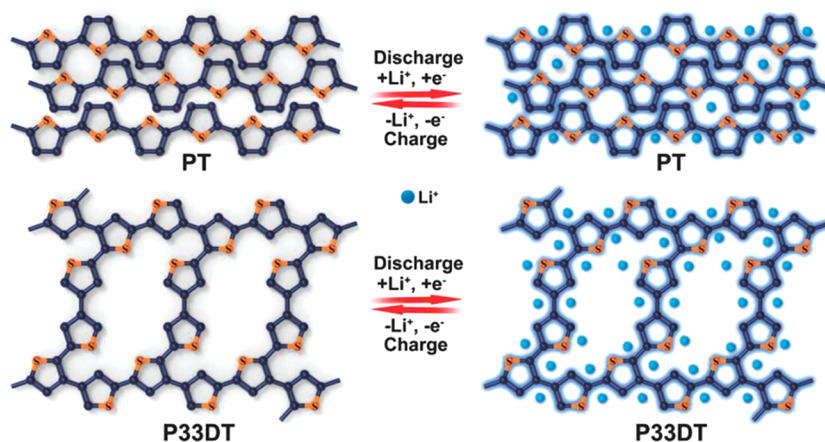


**Figure 26.** Schematic of charging mechanisms for polythiophene (PT) and P33DT. Reprinted with permission from ref 146. Copyright 2018 Wiley-VCH.

### 3.9. Photocatalytic Hydrogen Evolution

Many studies have focused on carbon nitride and inorganic semiconductors in photocatalytic  $\text{H}_2$  evolution reactions.<sup>172–174</sup> However, issues of tunability and low activity in visible light limits these materials. An organic porous push–pull polymer was reported for  $\text{H}_2$  evolution from water but requires preparation as a composite with  $\text{TiO}_2$ .<sup>175</sup> The microstructure and electronic properties of CMPs can be

controlled though the designed combination of building blocks, which provides potential advantages for water splitting photocatalysts.

In 2015, we described a library of CMPs copolymers, showing that the band gap can be tuned over a wide range in continuous fashion. These polymers were used for the photocatalytic generation of  $\text{H}_2$  from water in the presence of a sacrificial electron donor.<sup>52</sup> The polymers exhibited high

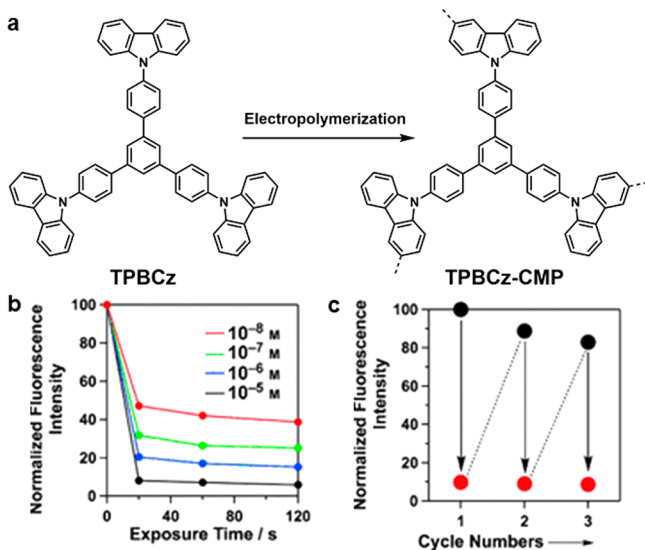


**Figure 27.** (a) Synthesis of TPBCz-CMP films. (b) Fluorescence intensity of CMP films upon immersion in saline solutions of dopamine. (c) Recycling tests of CMP films in  $10^{-8}$  M dopamine saline solution. Adapted with permission from ref 103. Copyright 2014 Wiley-VCH.

levels of porosity of up to  $1710 \text{ m}^2 \text{ g}^{-1}$  and could be used without additional metal cocatalysts or photosensitizers. It was found that some polymers were solely active under visible light rather than UV irradiation which we believe to be exclusive to

organic photocatalysts. The materials were stable for several catalytic cycles without photodegradation.

Fifteen CMP examples were statistically polymerized by Suzuki-Miyaura polycondensation of 1,4-benzene diboric acid (1) and/or 1,3,6,8-tetraboronic pinacol ester of pyrene (3) and/or 1,2,4,5-tetrabromobenzene (2) and/or 1,3,6,8-tetrabromopyrene (4) (Figure 31a, Table 3).<sup>52</sup> The BET surface areas range from  $597$  to  $1710 \text{ m}^2 \text{ g}^{-1}$ , with CP-CMP1 and CP-CMP10 reported previously for other electronic applications.<sup>42,44,117</sup> CP-CMP15 has the same nominal polymeric structure as in our previous work<sup>44</sup> but was synthesized using Suzuki-Miyaura coupling instead of Yamamoto coupling. The resultant CP-CMP15 here has a blue-shifted absorption onset and photoluminescence maximum, suggesting a subtly different microstructure from using an alternate synthetic protocol. UV-vis reflectance spectroscopy show a red-shift in optical absorption onset from  $420$  to  $640 \text{ nm}$  with increasing pyrene content when going from CP-CMP1 to CP-CMP15. This shows that the optical properties could be fine-tuned and by extension the optical gap over a broad range by adjusting the monomer ratios (Table 3). CP-CMP1, which is free from pyrene, emits in the blue with a maximum emission at  $445 \text{ nm}$ . CP-CMP2 through CP-CMP15, which has increasing levels of pyrene units, show a gradual red-shift from a bluish-green emission at  $465 \text{ nm}$  (CP-CMP2), to a saturated green-yellow emission at  $534 \text{ nm}$  (CP-CMP10), to a red emission at  $588 \text{ nm}$  (CP-CMP15). The gradual red-shift was attributed to the shift in the optical gap

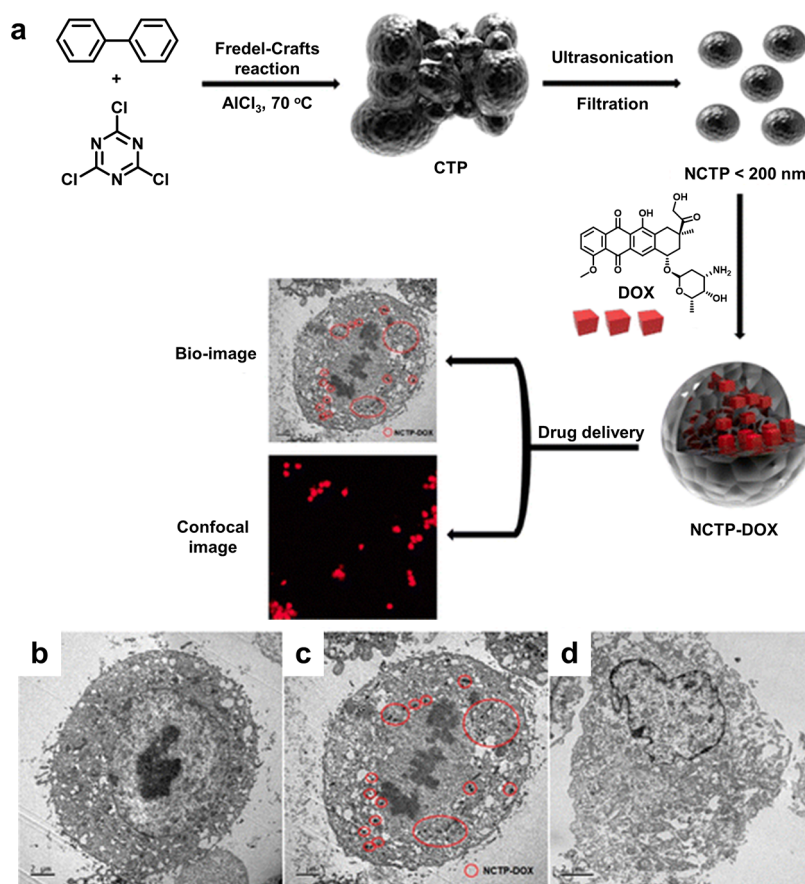


**Figure 28.** (a) Synthesis of nano-CTFs and encapsulation of DOX. Bio-TEM images of (b) HeLa cell control and (c) CTF-DOX and (d) DOX-treated HeLa cells after 6 h. Reprinted from ref 148. Copyright 2016 American Chemical Society.



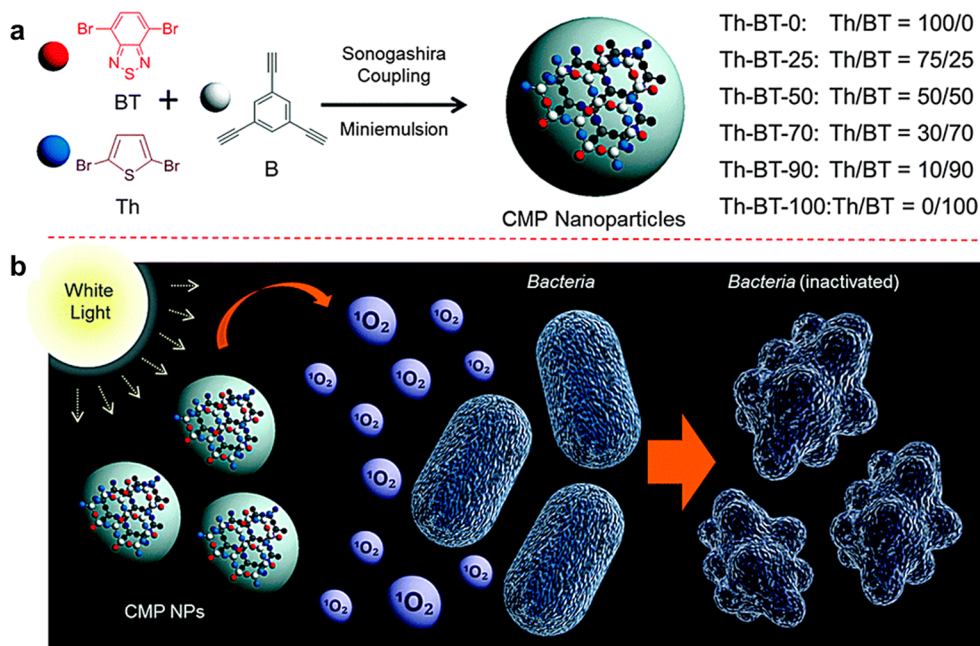


**Figure 29.** (a) Synthesis scheme of antibacterial CMP nanoparticles. (b) Schematic of bacteria inactivation with the use of CMP nanoparticles. Reprinted with permission from ref 151. Copyright 2016 The Royal Society of Chemistry.

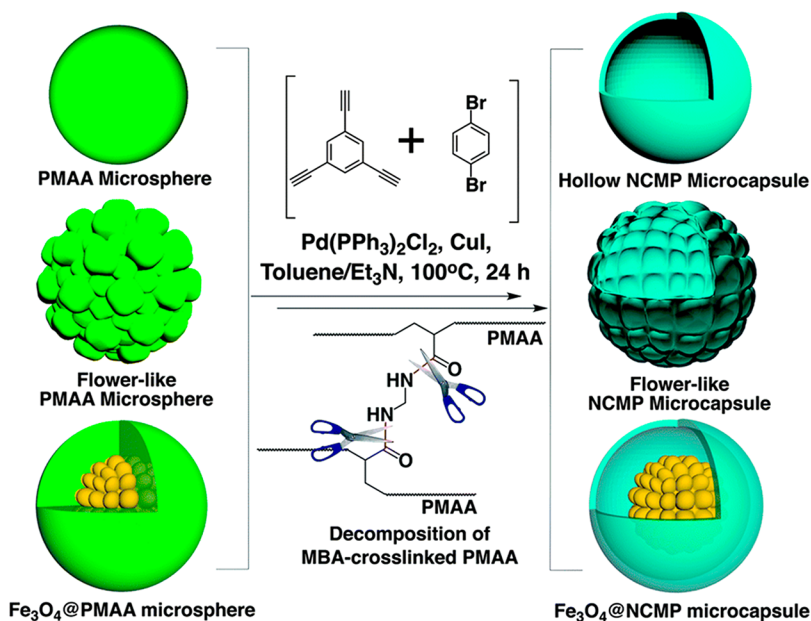


**Figure 30.** Synthesis of photothermally active CMP-1 shells using PMAA microsphere sacrificial templates. Reprinted with permission from ref 153. Copyright 2015 The Royal Society of Chemistry.

by incorporation of the pyrene chromophore, in combination with an increase in ring strain along the copolymer series. The CP-CMPs were tested for photocatalytic  $\text{H}_2$  evolution in water in the presence of the sacrificial electron donor diethylamine. Diethylamine showed the highest photocatalytic activity among a range of sacrificial agents, possibly due to better wettability or swelling of the polymer in the water/diethylamine mixture. All CP-CMPs show steady  $\text{H}_2$  evolution under visible light ( $\lambda > 420$  nm, Table 3), with an increase in the  $\text{H}_2$  evolution rate (HER) from CP-CMP1 to CP-CMP10 up to  $17.4 \pm 0.9 \mu\text{mol h}^{-1}$ , but a drop in performance was observed with CP-CMP11 through CP-CMP15 (Figure 31b). This shows there is an optimal optical band gap, with CP-CMP11 to

CP-CMP15 having optical band gaps too small. A kinetic explanation suggests that the barrier for electron-transfer between the polymers and protons increases with increasing pyrene content, therefore reducing the  $\text{H}_2$  evolution rate after CP-CMP10. CP-CMP10 has an absolute quantum yield of 4.2% and was shown to be stable over multiple 6 h cycles and continually over a 100 h period. We also show that CP-CMP10 does not perform under UV irradiation by replacement of the  $>420$  nm filter with a 710–315 nm filter, which resulted in a very similar rate of  $\text{H}_2$  production. A filter which only transmits UV light (U-340, 270–400 nm) showed a HER of only  $0.6 \mu\text{mol h}^{-1}$ . Other reports require addition of a metal cocatalyst for photocatalytic  $\text{H}_2$  evolution, whereas CP-CMPs are

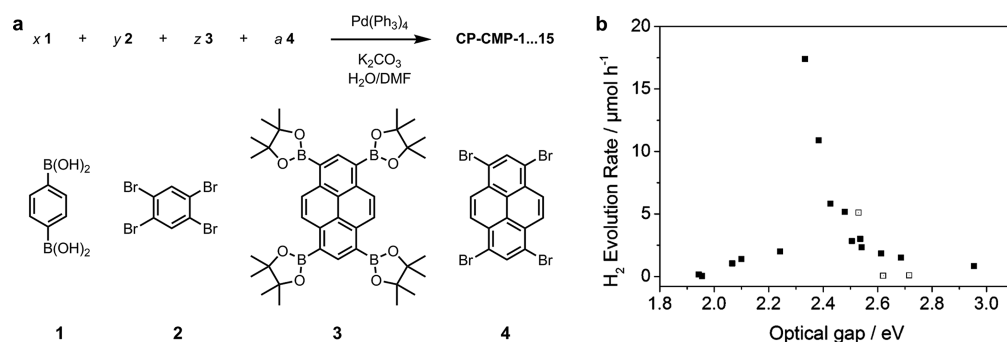


**Figure 31.** (a) Synthesis of CMP photocatalysts, CP-CMP-1 to 15.<sup>52</sup> (b) Rate of H<sub>2</sub> evolution against optical gap of polymers CP-CMP1–15 (■) and analogous linear polymers (□). Measurements relate to 100 mg catalyst in water containing 20 vol % diethylamine as an electron donor under filtered, visible irradiation ( $\lambda > 420$  nm,  $E < 2.95$  eV). Reprinted from ref 52. Copyright 2015 American Chemical Society.

**Table 3. Monomer Feed Ratios to Produce CP-CMPs and Their Surface Areas, Photophysical Properties, and H<sub>2</sub> Evolution Rates<sup>52</sup>**

copolymer	relative molar monomer ratio <sup>a</sup>				S <sub>A</sub> BET (m <sup>2</sup> g <sup>-1</sup> ) <sup>b</sup>	$\lambda_{em}$ (nm) <sup>c</sup>	optical gap (eV) <sup>d</sup>	total H <sub>2</sub> evolved ( $\mu$ mol) <sup>e</sup>	H <sub>2</sub> evolution rate ( $\mu$ mol h <sup>-1</sup> ) <sup>e</sup>
	1	2	3	4					
CP-CMP1	2	1	0	0	597	445	2.95	5	1.0 ± 0.1
CP-CMP2	2	0.99	0	0.01	682	465	2.69	8	1.4 ± 0.4
CP-CMP3	2	0.95	0	0.05	710	474	2.61	11	1.8 ± 0.2
CP-CMP4	2	0.90	0	0.10	684	483	2.54	14	2.4 ± 0.1
CP-CMP5	2	0.80	0	0.20	734	498	2.53	17	3.0 ± 0.2
CP-CMP6	2	0.60	0	0.40	726	512	2.50	15	2.6 ± 0.2
CP-CMP7	2	0.50	0	0.50	839	517	2.47	17	2.9 ± 0.2
CP-CMP8	2	0.40	0	0.60	1056	523	2.42	35	6.0 ± 0.6
CP-CMP9	2	0.20	0	0.80	762	528	2.38	69	10.9 ± 0.1
CP-CMP10	2	0	0	1	995	534	2.33	100	17.4 ± 0.9
CP-CMP11	1.9	0	0.05	1	770	535	2.24	11	2.0 ± 0.2
CP-CMP12	1.6	0	0.2	1	957	547	2.10	8	1.4 ± 0.2
CP-CMP13	1	0	0.5	1	1710	558	2.07	6	1.0 ± 0.1
CP-CMP14	0.4	0	0.8	1	1525	566	1.96	<0.5	<0.1
CP-CMP15	0	0	1	1	1218	588	1.94	<1	0.2 ± < 0.1

<sup>a</sup>The structures of monomers 1–4 are shown in Figure 31. <sup>b</sup>Apparent BET surface area. <sup>c</sup>Photoluminescent emission peak of polymer recorded in the solid state. <sup>d</sup>Calculated from the onset of the absorption spectrum. <sup>e</sup>Reaction conditions: 100 mg polymer was suspended in 100 mL diethylamine/water solution (20 vol %) and irradiated by a 300 W Xe lamp ( $\lambda > 420$  nm visible filter) for 6 h.

effective photocatalysts without the need for additional metal cocatalysts. It is worth noting that the Suzuki-Miyaura coupling reaction utilizes a Pd catalyst, and 0.42 wt % was found in CP-CMP10: control experiments show no correlation with the H<sub>2</sub> evolution activity, but this does not eliminate the likelihood that it plays a role in the photocatalysis.<sup>52</sup> Indeed, it was shown recently that noble metal concentrations as low as <40 ppm can influence catalytic H<sub>2</sub> evolution rates in conjugated polymers.<sup>176</sup>

Shortly after, the Lotsch group report tunability in a series of azine-linked COFs for visible light induced H<sub>2</sub> evolution;<sup>154</sup> a step forward from the first H<sub>2</sub> evolving COF based on hydrazine-linkage reported by the same group.<sup>177</sup> COFs with progressive substitution of alternate carbons in the central aryl ring of the triphenylaryl core by nitrogen atoms were synthesized, that is, phenyl (N = 0), pyridyl (N = 1), pyrimidyl (N = 2), and triazine (N = 3), to change the electronic and steric properties (Figure 32). The COFs produced from Schiff-base condensation yielded BET surface areas of 702 m<sup>2</sup> g<sup>-1</sup> in N<sub>0</sub>-COF, 326 m<sup>2</sup> g<sup>-1</sup> in N<sub>1</sub>-COF, 1046 m<sup>2</sup> g<sup>-1</sup> in N<sub>2</sub>-COF, and 1537 m<sup>2</sup> g<sup>-1</sup> in N<sub>3</sub>-COF. Diffuse reflectance spectra (DRS) show that COFs show similar absorption profiles with an absorption edge at ~465–475 nm,

suggesting an optical band gap of 2.6–2.7 eV. The increase in planarity along the N<sub>0</sub> to N<sub>3</sub> series leads to a higher degree of conjugation, thus a red-shift in the absorption spectrum. Concurrently, there is an increase in the electron-deficient character of the central aryl ring, leading to a blue-shift, which results in minimal changes in the overall optical band gap of the networks. The networks were tested for visible-light induced H<sub>2</sub> evolution with the addition of hexachloroplatinic acid for in situ formation of a Pt cocatalyst and triethanolamine as a sacrificial electron donor. The N<sub>x</sub>-COFs show an about 4-fold increase in HER with each additional N in the core, with N<sub>0</sub>, N<sub>1</sub>, N<sub>2</sub>, and N<sub>3</sub>-COF producing 23, 90, 438, and 1703 mmol h<sup>-1</sup> g<sup>-1</sup>, respectively, after 8 h. N<sub>3</sub>-COF was shown to be stable for 120 h with sustained H<sub>2</sub> evolution. Calculations showed that the formation of a radical anion during the photocatalytic process which is the rate-determining step was most favored for the N<sub>3</sub> system and least facile for the N<sub>0</sub> system, explaining the observed trend in H<sub>2</sub> evolution activity.<sup>154</sup>

Yu et al. reported the Suzuki-Miyaura polycondensation of several chromophore monomers with biphenyl (bph) and bipyridyl (bpy) units to generate PCP polymers for photocatalytic H<sub>2</sub> evolution.<sup>156</sup> Two types of monomers were

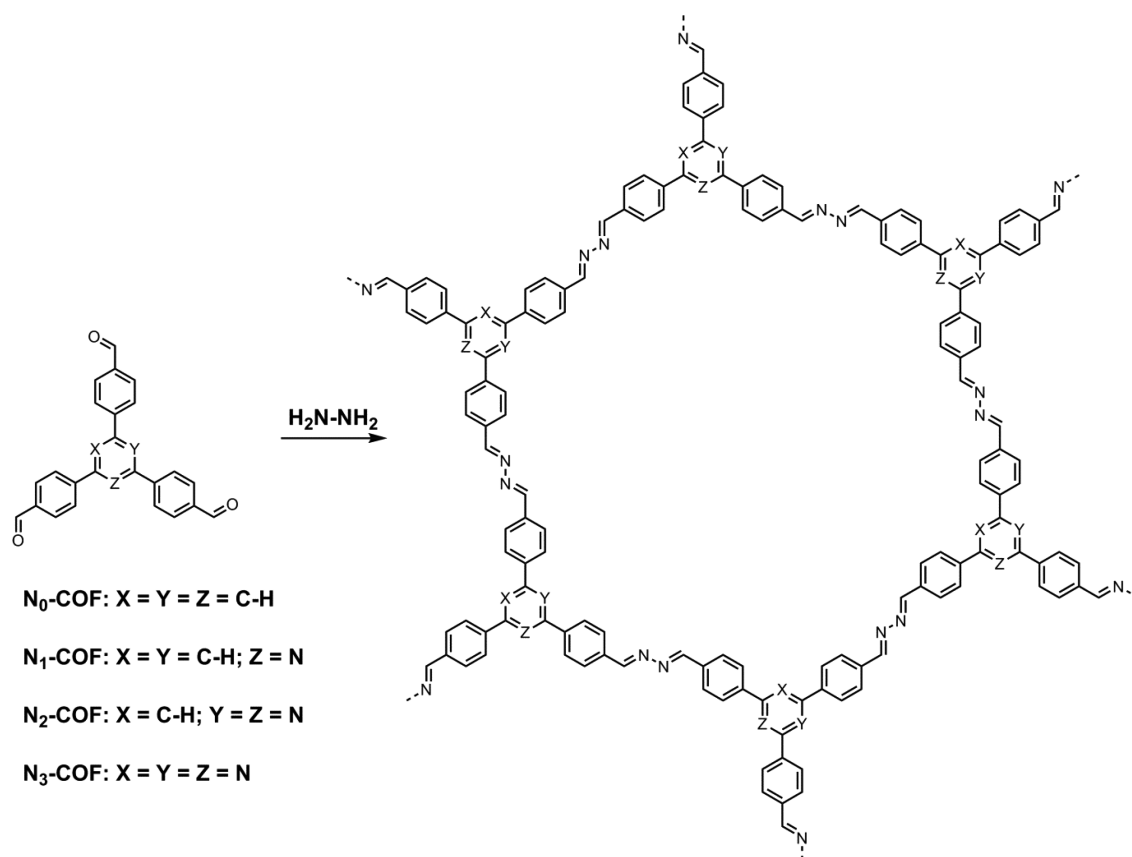


Figure 32. Synthesis of  $\text{N}_x\text{-COFs}$  from  $\text{N}_x\text{-aldehydes}$  and hydrazine for tunable photocatalytic  $\text{H}_2$  evolution.<sup>154</sup>

studied, an electron-deficient perylene bisimide and electron-rich spiro-fluorene, perylene, and a 4,8-di(thiophen-2-yl)benzo[1,2-b:4,5-b']dithiophene chromophore which were linked with weak donor pbh or weak acceptor bpy at different ratios (Figure 33). The polymers had BET surface areas ranging from 39 to 279  $\text{m}^2 \text{g}^{-1}$  and optical band gaps ranging from 1.81 eV using the electron-deficient monomer, to 2.89 eV using electron-rich spiro-fluorene due to limited extension of conjugation caused by the twisted structures (Table 4). Density functional theory (DFT) calculations were used to calculate the HOMO and LUMO energy levels, with the calculated band gap values matching that of the experimental measurements. The polymers were tested for photocatalytic  $\text{H}_2$  evolution under visible light in the presence of a sacrificial agent with the performance rates in the following order: triethylamine > diethylamine > diethanolamine > methanol. It was found that PCP4e, built from 4,8-di(thiophen-2-yl)benzo[1,2-b:4,5-b']dithiophene and bpy, had the best performance with a HER of 33  $\mu\text{mol h}^{-1}$  compared with the electron-rich chromophore using bph of  $\sim 8 \mu\text{mol h}^{-1}$ . They also found that polymers with a higher degree of extended conjugation resulted in larger  $\text{H}_2$  evolution rates. It was thought that the nitrogen atom in the bpy unit may play a role by hydrogen-bonding with the water molecules and help increase the local concentration of water molecules for reduction. The optimized polymer, PCP4e, had the highest apparent quantum yield (AQY) of 0.34% at 350 nm. The effects of PCP4e with various amounts of residual Pd content were tested by varying the initial catalyst amount during polymerization and found that the  $\text{H}_2$  evolution rate rapidly increases with residual metal content but becomes saturated above 0.46%.<sup>156</sup>

Maji and co-workers reported band gap engineering by varying the donor and acceptor monomer contents with tetraphenylene and 9-fluorenone, respectively.<sup>178</sup> The optical band gap systemically decreases with increasing amounts of the acceptor monomer, from 2.8 to 2.1 eV. An optimum  $\text{H}_2$  evolution rate of 660  $\mu\text{mol g}^{-1} \text{h}^{-1}$  under visible-light irradiation was found for the CMP with a moderate amount of acceptor units. The  $\text{H}_2$  evolution rate increased with decreasing optical band gap as the redshift allowed absorption of more photons and generated more charge carriers, which facilitates the photocatalysis. On the contrary, a too narrow band gap with the most acceptor units promoted nonradiative electron-hole recombination, leading to a reduced  $\text{H}_2$  evolution rate.

Zhang and Wang et al. reported benzothiadiazoles-based CMPs for  $\text{H}_2$  production in water.<sup>159</sup> An electron-donor-acceptor strategy was utilized with benzothiazole as an electron-withdrawing unit incorporated into the polymer backbone at various positions on the phenyl ring, resulting in 1D to 3D polymers. Suzuki-Miyaura polycondensations of 4,7-dibromobenzo[*c*]-[1,2,5]thiadiazole (BT) with either benzene-1,4-diboronic or 1,3,5-phenyltriboronic acid tris(pinacol) ester (Figure 34a) yielded polymers with BET surface areas from 17 to 280  $\text{m}^2 \text{g}^{-1}$ . DRS showed a broad absorption range of the polymers in the visible region, where the one-dimensional polymer, B-BT-1,4 exhibited the largest adsorption area and the 3D counterpart, B-BT-1,3,5, showed the narrowest absorption range (Figure 34b). It was observed that by expanding the 3D character of the polymer, this resulted in a gradual decrease in the absorption ranges. B-BT-1,4 possessed the narrowest optical band gap of 2.17 eV, whereas B-BT-1,3,5



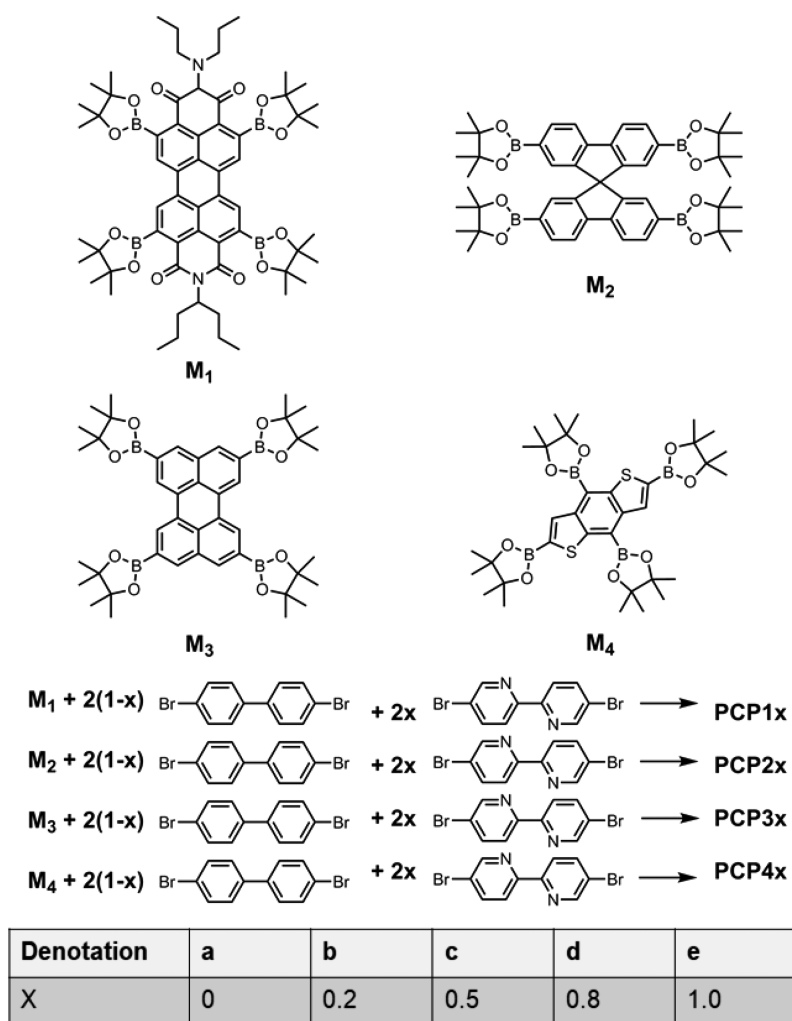


Figure 33. Structures of M<sub>x</sub> monomers and the Suzuki-Miyaura polymerization to produce PCP photocatalysts.<sup>156</sup>

Table 4. Physical and Chemical Properties and H<sub>2</sub> Evolution Rates of PCP Photocatalysts<sup>156</sup>

PCP	S <sub>A</sub> BET (m <sup>2</sup> g <sup>-1</sup> ) <sup>a</sup>	λ <sub>o</sub> (nm) <sup>b</sup>	optical band gap (eV) <sup>c</sup>	Pd (wt %) <sup>d</sup>	H <sub>2,ful</sub> (μmol h <sup>-1</sup> ) <sup>e</sup>	H <sub>2,vis</sub> (μmol h <sup>-1</sup> ) <sup>e</sup>
PCP1a	39	683	1.81	1.22	1.4	0.06
PCP1e	59	633	1.95	1.60	13.0	0.49
PCP2a	228	429	2.89	1.15	6.4	1.39
PCP2e	279	505	2.45	0.89	26.0	5.11
PCP3a	121	535	2.31	1.17	5.1	0.91
PCP3e	99	566	2.19	0.94	17.8	2.75
PCP4a	80	530	2.33	0.84	7.2	1.45
PCP4e	104	601	2.06	0.81	33.0	6.65

<sup>a</sup>BET surface areas were measured from the N<sub>2</sub> adsorption isotherms from 0.005 to 0.20 bar. <sup>b</sup>Absorption onsets were measured by diffuse reflectance UV–vis spectroscopy. <sup>c</sup>Optical band gaps were calculated by the equation  $E_g = 1240/\lambda_o$ . <sup>d</sup>Residual Pd contents were measured by ICP-MS. <sup>e</sup>H<sub>2,ful</sub> and H<sub>2,vis</sub> represent the H<sub>2</sub> production rates under full-arc irradiation and visible light irradiation, respectively.

exhibited the broadest optical band gap of 2.42 eV. CV showed that the linear polymers had lower LUMO levels than the 3D polymers due to better extended conjugation, thus a narrower band gap (Figure 34d). The photocatalytic HER of B-BT-1,4 was ~12 μmol h<sup>-1</sup> under visible light irradiation and with a triethanolamine sacrificial electron donor. The polymer was optimized with ~3 wt % Pt and resulted in a 10-fold HER of 116 μmol h<sup>-1</sup> under visible light and a AQY of 4.01% at 420 nm. B-BT-1,3,5 showed a moderate HER of 20 μmol h<sup>-1</sup>. A study of the 3D structural influence was performed by gradual copolymerization with an increasing amount of cross-linker

into the polymer backbone (Figure 34a) and resulted in the gradual widening of the optical band gap and decrease in HER. The performance was attributed to light-induced electron mobility and electron transfer, which was superior in the linear series and the broader absorption range of B-BT-1,4 in the visible region providing additional contribution.<sup>159</sup>

Our group looked upon the structure–property relationships of CMP linker geometry, comonomer linker length, and degree of planarization on HER.<sup>158</sup> In addition to previously reported CP-CMP1,<sup>52</sup> an extended biphenyl analogue (PE-CMP) was studied (Figure 35a). A 1,3,5-linked analogue of poly(*meta*-

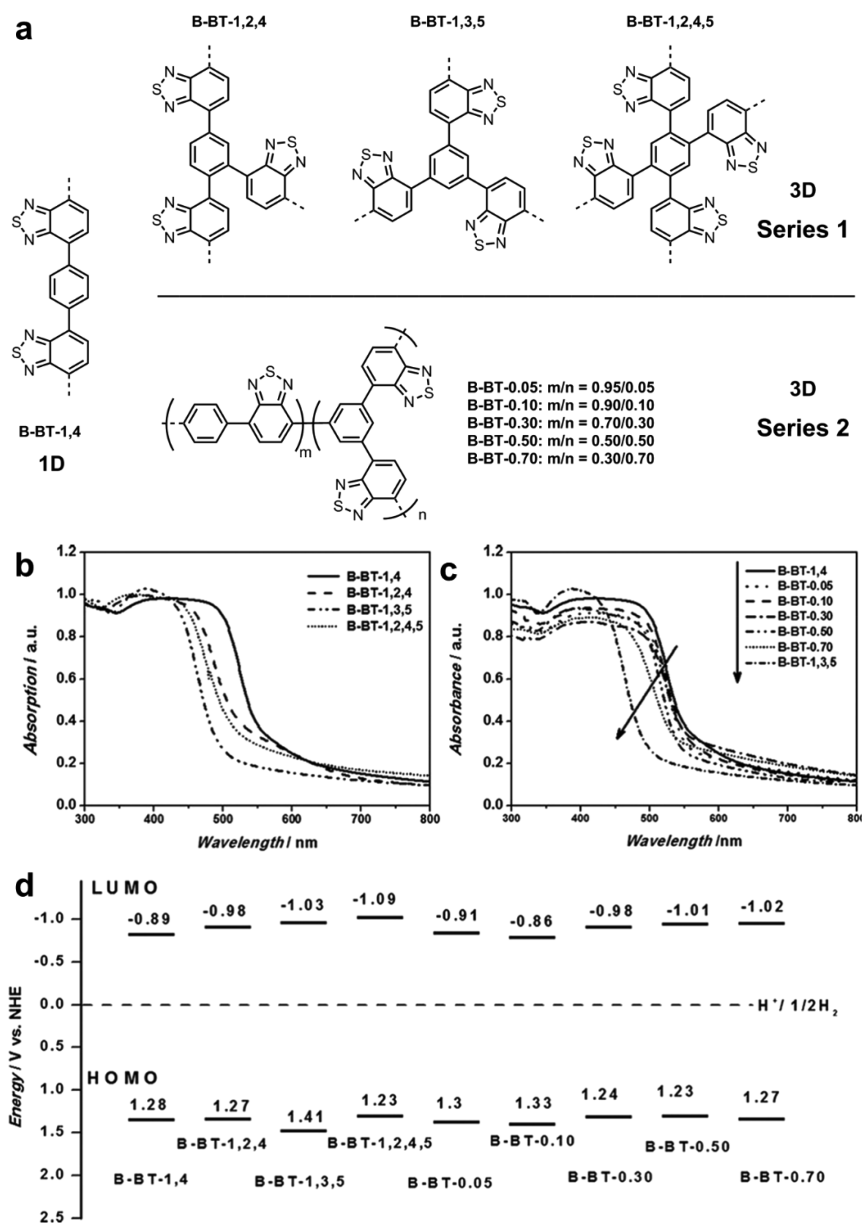


**Figure 34.** (a) Structures of 1D and 3D polybenzothiadiazole CMPs. UV-vis diffuse reflectance spectra of polymers in (b) series 1 and (c) series 2. (d) HOMO and LUMO band position of polymers calculated from cyclic voltammetry (the standard error of the LUMO position is  $\pm 0.008$  eV from three measurements). Adapted with permission from ref 159. Copyright 2016 Wiley-VCH.

phenylene) (M-CMP) and its extended analogue (ME-CMP) was also synthesized. The concept of planarization was studied with a spirobifluorene CMP (SP-CMP) and its extended analogue (ESP-CMP). The CMPs synthesized from Suzuki-Miyaura polycondensation yielded BET surface areas of up to  $895 \text{ m}^2 \text{ g}^{-1}$  for SP-CMP, with the extended equivalents resulting in a lower surface area than their nonextended analogues. A red-shift in the solid-state UV-vis reflectance was observed when extending the linker from CP-CMP1 to PE-CMP. The 1,3,5-linked M-CMP and ME-CMP are blue-shifted compared to their 1,2,4,5-linked analogues (CP-CMP1 and PE-CMP) both in their absorption onsets and photoluminescence maxima. This result was attributed to a lower effective conjugation length for the meta-linked CMPs. SP-CMP and ESP-CMP are red-shifted with respect to PE-CMP due to a greater effective conjugation length. In this study, triethylamine was used as a sacrificial electron donor in a

water/methanol mixture which was found to yield better HERs. It was found that the efficiency of the CMPs as photocatalysts strongly related to their chemical structure. PE-CMP showed higher HERs than its nonextended equivalent CP-CMP1, both under combined UV/visible light ( $17.9 \mu\text{mol h}^{-1}$  vs  $4.1 \mu\text{mol h}^{-1}$ ;  $>295 \text{ nm}$ ) and under visible light ( $0.5 \mu\text{mol h}^{-1}$  vs  $0.2 \mu\text{mol h}^{-1}$ ;  $>420 \text{ nm}$ ) (Figure 35b). M-CMP showed only a very small amount of  $\text{H}_2$  evolved under  $>295 \text{ nm}$  illumination and complete loss of activity under visible light. Extension from phenyl to biphenyl in ME-CMP resulted in a significant increase of  $9.8 \mu\text{mol h}^{-1}$  under  $>295 \text{ nm}$  illumination but still no activity under visible light. SP-CMP resulted in the highest HER under  $>295 \text{ nm}$  illumination of  $28.8 \mu\text{mol h}^{-1}$  and visible light of  $3.0 \mu\text{mol h}^{-1}$ . The extended ESP-CMP has a similar absorption on-set of  $2.86 \text{ eV}$  to SP-CMP of  $2.84 \text{ eV}$ , with no significant change in photocatalytic activity. The AQY of SP-CMP was 0.23% at  $420 \text{ nm}$ .

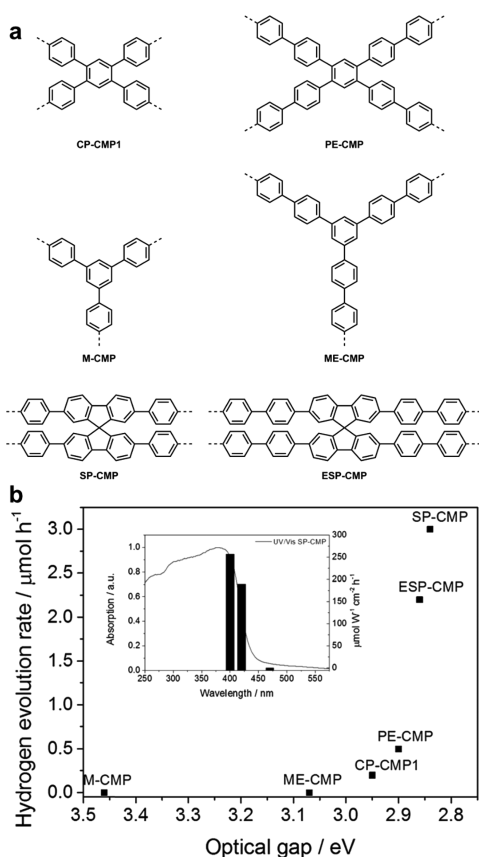


**Figure 35.** (a) Structures of CMPs and their extended equivalent for photocatalytic H<sub>2</sub> evolution. (b) H<sub>2</sub> evolution rates under visible light ( $\lambda > 420$  nm) correlated with the optical gap of the CMPs. Measurements were performed with 25 mg catalyst in water/MeOH/triethylamine mixture. Wavelength dependency of the photocatalytic H<sub>2</sub> evolution for SP-CMP (insert). Reprinted with permission from ref 158. Copyright 2016 The Royal Society of Chemistry.

Photostability tests of SP-CMP under  $>420$  nm illumination for 72 h, followed by  $>295$  nm illumination for 44 h, showed no significant changes to the material properties, both suggesting good stability and ruling out the polymer as the H<sub>2</sub> source. Photoluminescence lifetime of the polymers were only partially associated with the H<sub>2</sub> evolution activity as other factors, such as lack of light absorption, can become dominant.<sup>158</sup>

Bhunia and Janiak et al. synthesized CTFs for CO<sub>2</sub> sorption, sensing, and light-driven H<sub>2</sub> evolution applications.<sup>155</sup> They utilized room temperature, trifluoromethanesulfonic acid

catalyzed cyano-cyclotrimerization of tetra(4-cyanophenyl)-ethylene to produce PCTF-8 with a BET surface area of 625 m<sup>2</sup> g<sup>-1</sup> (Figure 36). Solid-state absorption of PCTF exhibits a broad absorption band centered around 400 nm ranging from 300 to 600 nm, associated with the tetraphenylethylene units. The material shows a strong greenish-yellow fluorescence with an emission maximum at 562 nm when excited at 395 nm and a fluorescence quantum yield of 31% at room temperature. The optical band gap of PCTF-8 was estimated to be 2.25 eV from its UV-vis spectrum. The pristine CTF shows no H<sub>2</sub> evolution in the presence of methanol or triethanolamine sacrificial donor aqueous solutions. After loading PCTF-8 with 2.3 wt % Pt, the material shows HER rates of 1780 and 2370  $\mu\text{mol g}^{-1}$  after irradiation with a 300 W Xe lamp for 20 h in buffered aqueous methanol and sacrificial donor solutions, respectively.<sup>155</sup>

From 2017, we explored how structural changes affected the photocatalytic H<sub>2</sub> evolution behavior in amorphous CTFs.<sup>179</sup> We first investigated the relationship between photocatalytic activity with differing phenylene spacer lengths of 1 to 4 units, synthesized by acid-catalyzed trimerization and Suzuki-Miyaura polycondensation. The H<sub>2</sub> evolution rates were not significantly different for both reaction types, despite some differences in optical properties. CTF-2, with a biphenyl linker, exhibited the highest photocatalytic activity, due to a combination of thermodynamic driving force and optical gap which could be controlled by this structural tuning. Recently, we extended this study to 39 CTFs containing various phenylene oligomers, 5-membered ring heterocycles, substituted benzenes, bipyridyls, *N*-heterocycles, planar-substituted fluorenes, and azoles/quinoxalines, using a high-throughput workflow (Figure 37).<sup>180</sup> This approach allowed discovery of CTFs with H<sub>2</sub> evolution rates among the highest for this class of materials. The photocatalytic performances could be analyzed by their predicted ionization potential, optical gap, predicted electron affinity, and dispersibility, with the latter two found to be the dominant variables. This study shows that high-throughput workflow is a powerful tool to discover new photocatalysts and can provide important insights into the structure–property relationships across a wide range of chemical functionality in any material class.

Tan and co-workers recently reported a new strategy to synthesize crystalline CTFs by slowing down the nucleation process, which leads to higher photocatalytic H<sub>2</sub> evolution than less crystalline CTFs.<sup>181</sup> The controlled oxidation of alcohol monomers in DMSO solution at a moderate temperature of 120–150 °C allows for optimal crystallinity. The best performing material (CTF-HUST-C1) had a H<sub>2</sub> evolution

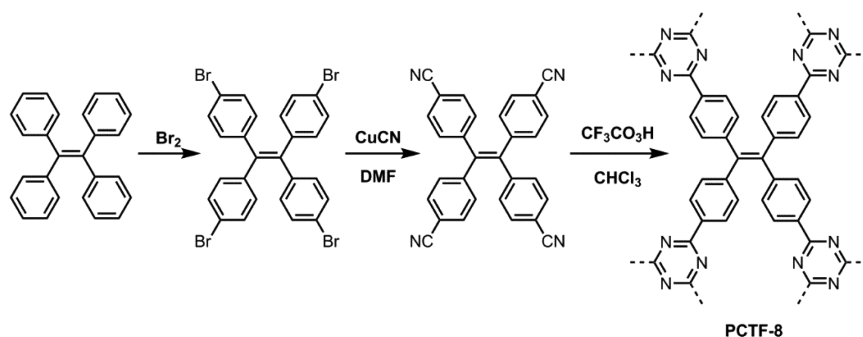


**Figure 36.** Synthesis of PCTF-8 photocatalyst.<sup>155</sup>



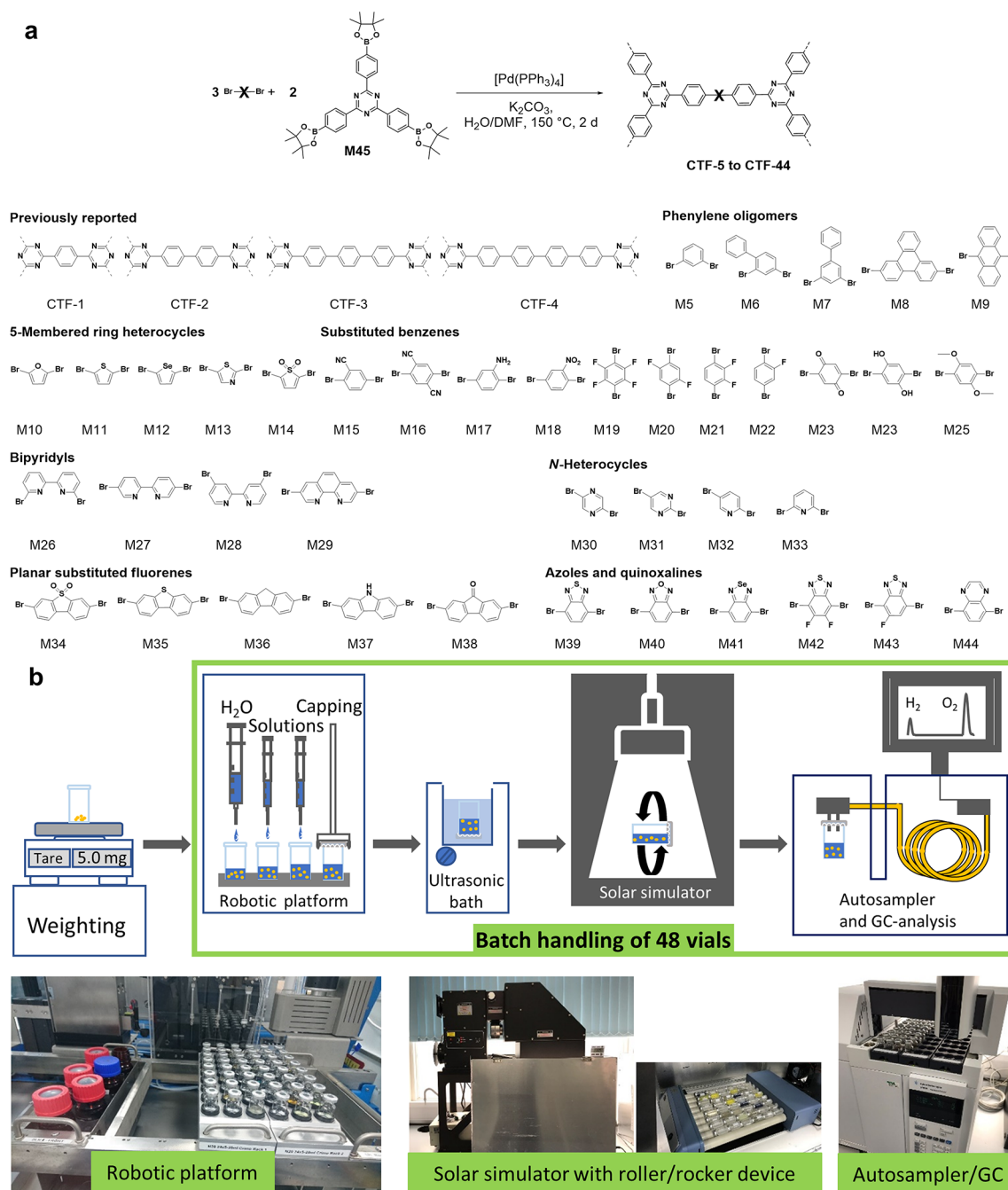


**Figure 37.** (a) Synthesis of CTF library. (b) High-throughput workflow for  $\text{H}_2$  evolution testing (top row) and photographs of equipment used in the workflow (bottom row). Reprinted with permission from ref 180. Copyright 2019 American Chemical Society.

rate of  $5100 \mu\text{mol h}^{-1} \text{g}^{-1}$ , which was higher than its amorphous equivalent, and this material maintained a  $\text{H}_2$  evolution rate of  $3880 \mu\text{mol h}^{-1} \text{g}^{-1}$  over a 25 h irradiation time. The improved performance was attributed to better charge transport and a broader light absorption in the more crystalline CTF.

The Li group demonstrated that the formation of CTF heterostructures can enhance photocatalytic  $\text{H}_2$  production.<sup>182</sup> A sequential polymerization strategy was utilized to synthesize a benzothiadiazole (BT) and thiothene (Th) CTF with electron-withdrawing and electron-donating units, respectively (Figure 38). The hybrid material exhibited improved charge-carrier separation efficiency, suppressing the usual fast recombination of photoexcited electrons and holes. The

CTFs with photodeposited Pt nanoparticles (ca. 3 wt %) exhibited a  $\text{H}_2$  of  $6.6 \text{ mmol g}^{-1} \text{h}^{-1}$  under visible light irradiation, approximately 6 times higher than the single-component polymers, CTF-BT and CTF-Th.

Yu and co-workers studied various donor–acceptor linked CMPs, observing the effect of the acceptor comonomer with photocatalytic  $\text{H}_2$  evolution.<sup>157</sup> Eleven polymers, PCP0–PCP11, were synthesized from Suzuki–Miyaura polycondensations of 4,8-di(thiophen-2-yl)benzo[1,2-b:4,5-b']-dithiophene (DBD) and various phenyl comonomers of different lengths, geometries, and amount of nitrogen substituted into the phenyl ring (Figure 39a). Photocatalytic  $\text{H}_2$  evolution was evaluated in a water/triethylamine mixture with 12.0 mg of polymer under full-arc irradiation. Low activity ( $1.9\text{--}10.1 \mu\text{mol h}^{-1}$ ) was

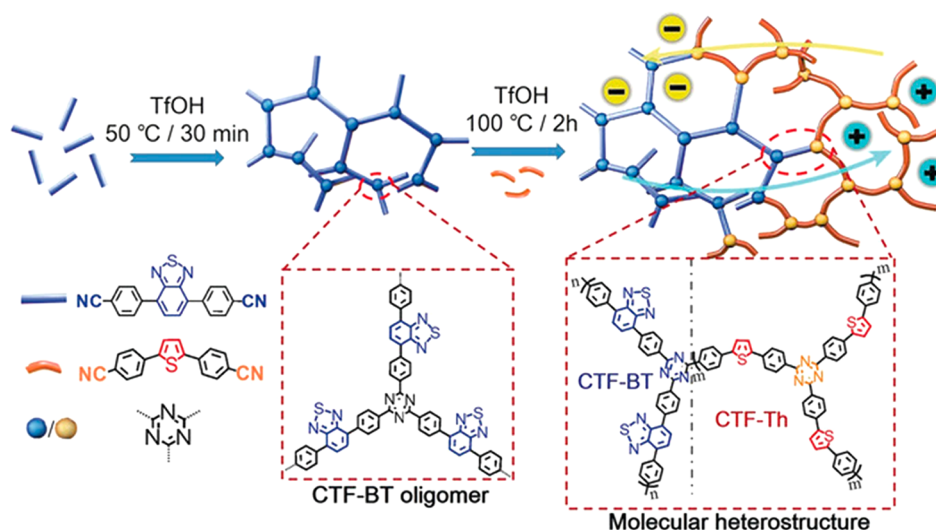


**Figure 38.** Synthesis of CTF heterostructures by sequential polymerization. Reprinted with permission from ref 182. Copyright 2019 Wiley-VCH.

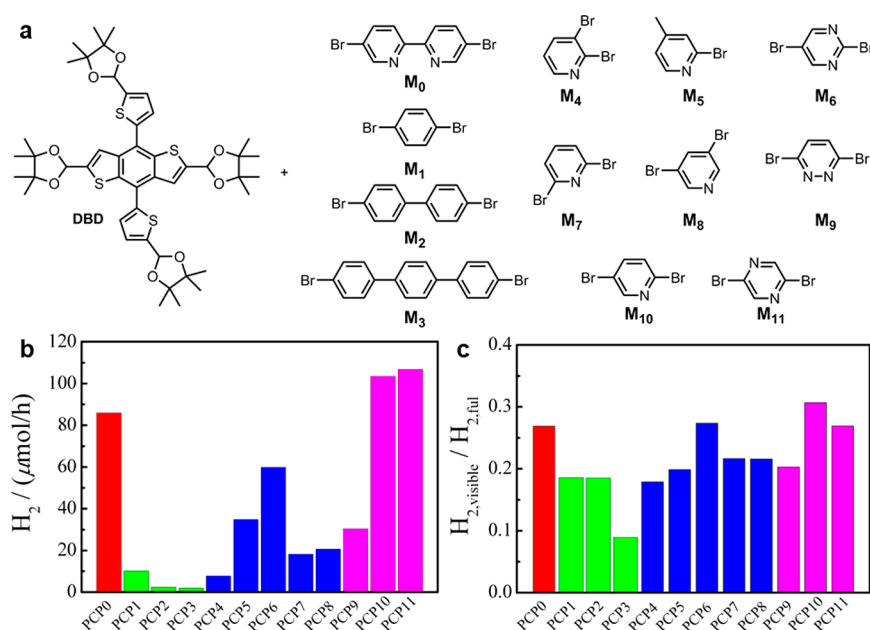


**Figure 39.** (a) Structures of M<sub>0</sub>–M<sub>11</sub>, used to synthesize PCP0–PCP11. (b) Photocatalytic H<sub>2</sub> evolution rates of PCP0–11 under full-arc irradiation for 2 h. (c) Retention ratios of H<sub>2</sub> evolution rates of PCP0–11 under visible light and full-arc irradiation. Adapted from ref 157. Copyright 2016 American Chemical Society.

observed for donor–donor based polymers (PCP1–3), and the HER decreases as the chain length of the phenylene linker increases from 1 to 3 (Figure 39b). Thus, full donor-based polymers are not ideal due to a lack of internal polarization for effective charge separation process and the hydrophobicity of these materials. PCP4–8 based on a set of pyridine units but at different connectivities and dipole orientations show high HERs, with PCP6 containing a para-substituted pyridine yielding a HER of 59.8 μmol h<sup>-1</sup>. The meta-substituted equivalent (PCP5, PCP6, and PCP8) show HERs ranging from 18.2–34.9 μmol h<sup>-1</sup>. Ortho-substituted PCP4 show a HER of 7.8 μmol h<sup>-1</sup>. It was concluded that the lower HERs from ortho- or meta-substituted units into the system break the conjugation of the polymer backbone which are detrimental for the charge transport. Strong acceptor diazine units at various positions were incorporated into PCP9–11. PCP10 and PCP11 show enhanced HERs of 103.6 and 106.9 μmol h<sup>-1</sup>,

respectively, due to the enhanced internal polarization. PCP9 shows a moderate HER of ~30.4 μmol h<sup>-1</sup> due to its different internal dipole orientation. It was found that most of the polymers retained ~20% of their HER under visible light irradiation (Figure 39c).<sup>157</sup>

The Jiang group demonstrated high photocatalytic H<sub>2</sub> evolution with dibenzothiophene dioxide-containing CMPs and report the influence of strut length, from monophenyl to triphenyl, on the performance.<sup>183</sup> They found that an increasing strut length reduced the photocatalytic performance of the materials due to a lower degree in conjugation and planarity of the molecular main chain, which resulted from the increasingly twisted polymer skeleton. The CMPs with the addition of 3 wt % Pt exhibited a H<sub>2</sub> evolution rate of 4600, 440, and 140 μmol h<sup>-1</sup> g<sup>-1</sup> under visible light for strut lengths of 1, 2, and 3 phenyls, respectively.

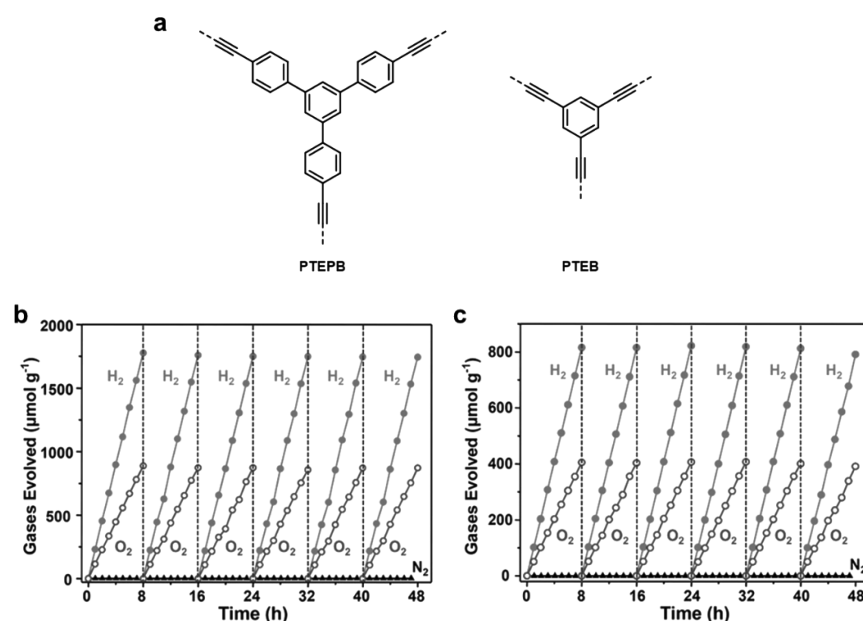
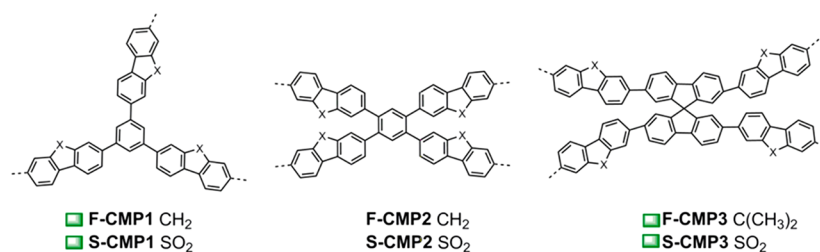


**Figure 40.** (a) Structures of PTEPB and PTEB photocatalysts. Time course of  $\text{H}_2$  and  $\text{O}_2$  production under visible light irradiation using (b) PTEPB and (c) PTEB. Reprinted with permission from ref 53. Copyright 2017 Wiley-VCH.

### Microporous Networks



### Non-porous Linear Polymers

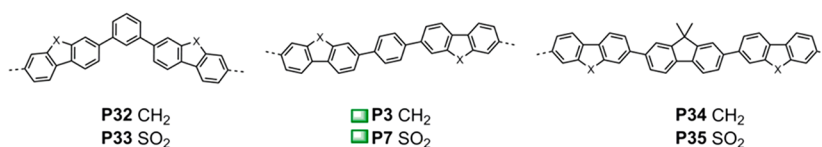


**Figure 41.** CMP networks (first row) with linear polymer equivalent (second row). For each pairing, the photocatalyst showing higher performance under visible light (CMP or nonporous/low porosity linear polymer) is marked with a green square. Reprinted from ref 160. Copyright 2019 American Chemical Society.

In 2017, Wang et al. reported the first CMP that shows overall photocatalytic water splitting in pure water.<sup>53</sup> The group used conventional 1,3,5-diyne-linked CMPs prepared in a sheet-like structure, which led to the simultaneous generation of  $\text{H}_2$  and  $\text{O}_2$  under visible light irradiation. It was claimed that the nanosheet structure allows the photogenerated excitons to instantaneously reach the polymer surface to drive redox reactions and that this suppresses electron–hole recombination. Poly-1,3,5-tris(4-ethynylphenyl)-benzene (PTEPB) and poly-1,3,5-triethynylbenzene (PTEB)<sup>40</sup> CMPs were studied (Figure 40a).  $\text{H}_2$  and  $\text{O}_2$  were generated close to the expected 2:1 stoichiometry expected for overall water splitting (Figure 40b,c). The average  $\text{H}_2$  production rates for PTEPB and PTEB were reported to be 218 and 102  $\mu\text{mol h}^{-1} \text{g}^{-1}$ , respectively,

translating to apparent quantum efficiencies at 420 nm of 10.3% and 7.6%, respectively. The solar-to- $\text{H}_2$  conversion efficiency was reported to reach 0.6%, coming close to the performance of leading inorganic catalysts reported by Domen and colleagues.<sup>184</sup> This is a remarkable result that merits further detailed investigation and validation.

It is difficult to distinguish whether porosity is an important factor for photocatalytic  $\text{H}_2$  evolution as there have been reports of linear conjugated polymers that surpass results of CMPs.<sup>159,185,186</sup> Recently, we investigated this question with three series of CMPs and their linear structural analogues (Figure 41).<sup>160</sup> In general, neither the porous CMPs nor the nonporous linear can be considered superior overall: instead, the optimal morphology (porous or nonporous) depends on



the linkers used in the polymer. Various factors contribute to the photocatalytic activities of these polymers: particle size, swellability, residual Pd content, and wettability. It was found that the observed optical gaps and light absorption profiles of the porous and nonporous polymers were quite similar. Porosity can have benefits of increasing access to the catalytically active sites, which is further benefitted with swelling. In contrast, the highly twisted natures in CMP linkers might cause a reduction in charge-mobility, which may counterbalance or negate any benefits of mass transfer that arises from porosity.

These various studies on photocatalytic H<sub>2</sub> evolution highlight a number of important design parameters to consider for the design of future CMPs for this application.

1. The donor–acceptor ratio should be carefully considered. Increasing the redshift in CMPs allows for the absorption of more photons and results in a lower band gap.
2. Planarization of units is important for efficient conjugation. Twisted aromatic units reduce conjugation throughout the polymer, and this often results in lower photocatalytic activity.
3. Porosity can increase the accessibility of water to catalytically active sites and promote mass transfer. However, porous networks often result in increased twisting in the aromatic units when compared to nonporous linear polymers. Crystalline-layered COFs offer a potential solution here,<sup>154,187</sup> and it is possible that these might outperform amorphous CMPs for this particular application, also because crystalline materials may exhibit more efficient charge transport. More generally, while porosity aids mass transport, it may also decrease charge transport, and the pore size/pore topology might be important. A moderately high surface area material with no pores (e.g., dense nanoparticles) might outperform a porous solid in some cases.
4. Increasing the wettability by the use of hydrophilic monomers can improve activity by improving the surface interaction with water; studies so far suggest that this is a relatively general rule, providing that the introduction of these monomers does not compromise other key properties.
5. Reducing the polymer particle size can increase performance. A lower particle size exposes more of the external catalytic surface area. It can also help with dispersibility, especially when coupled with hydrophilicity.
6. Sulfone CMPs generally show increased lifetime of the excited state compared to their hydrocarbon equivalents. There is value in exploring other monomer functionalities in this regard.
7. Long-term photochemical stability beyond 50–100 h or so is still a somewhat open question for CMPs and COFs, and this should be explored in more detail.

#### 4. OUTLOOKS AND CONCLUSION

As summarized above, CMPs have emerged as a surprisingly broad platform in materials chemistry. Undoubtedly, much interest stems from the modularity of the approach: there are a large number of coupling reactions available to create a diverse range of networks and, so long as the monomers are chosen to be relatively rigid, the result will quite likely be a porous solid.

In this respect, these materials are similar to MOFs and PCPs:<sup>2–5</sup> there are a huge number of permutations that can be explored. As for MOFs, however, not all such combinations are likely to be interesting or competitive with other materials classes. There are now many types of porous solids available (and, recently, even porous liquids),<sup>188</sup> and some of these, such as activated carbon, are inexpensive and scalable. It is worth considering, therefore, what the unique advantages of CMPs might be. In 2015, we reviewed porous materials from a function perspective<sup>189</sup> and concluded that the fundamental “unique selling point” for CMPs was their extended conjugation. Indeed, in this regard we consider CMPs to be unique; to our knowledge, they were the first microporous organic semiconductors, later joined by conjugated COFs.<sup>19,54,187,190–193</sup>

A number of examples in this review take advantage of conjugation in CMPs, such as in photocatalysis, but there is still much untapped potential. As far back as 2009, one of us wrote a perspective on CMPs<sup>26</sup> that concluded: “The high physical surface area in CMPs offers the potential of in-filling with a second conjugated polymer—for example, the compatibilization of polymers that might otherwise phase separate in a blend, and which cannot be generated in one step as an interpenetrating network.” Ten years on, there are still opportunities there: for example, to form donor–acceptor heterojunction materials for photocatalysis,<sup>52,126,156</sup> as discussed further below.

Given that we highlight extended conjugation as the unique selling point for CMPs, one should consider CMPs with respect to conjugated COFs. When the first CMP paper was published,<sup>25</sup> the few COFs that were then known were nonconjugated in the 2D plane of the COF layers because the linking groups were boronate esters.<sup>12,39</sup> Subsequently, a range of conjugated COFs has been introduced by using bonds such as imines,<sup>193,194</sup> azines,<sup>154,190</sup> triazines,<sup>19</sup> fused azabenzene,<sup>195,196</sup> and alkenes.<sup>54,197,198</sup> Here, we define “conjugation” as the covalent bonding pattern in the framework: it is also possible that  $\pi$ -stacked columns in these COF structures can contribute significantly to charge transport.<sup>54,198–201</sup> This raises the question of whether crystalline conjugated COFs or amorphous conjugated microporous polymers are likely to be superior platforms in functional materials chemistry in terms of their optoelectronic properties. We suggest that there is no simple answer to this. First, the level of long-range order in COFs can be quite variable. A very small number of COFs are single crystalline,<sup>202,203</sup> but these examples are not conjugated: most conjugated COFs so far have moderate to good levels of long-range order, though the recent work of Dichtel and colleagues, in particular, points to ways to enhance order on COFs in the future.<sup>204–206</sup> Similarly, not all networks formed using irreversible chemistry are totally amorphous; for example, CTFs can be rendered at least partially crystalline if forcing synthesis conditions are used.<sup>19</sup>

A different question is how much does crystalline order actually matter in these materials? There are few studies that compare analogous ordered and disordered systems to answer this. In 2018, we investigated the photocatalytic H<sub>2</sub> evolution rates for an ordered sulfone COF and its disordered, amorphous analogue, synthesized purposely under conditions to eliminate crystallinity.<sup>187</sup> In that case, the photocatalytic activity of the ordered COF was much better than the amorphous analogue, though it should be noted that the degree of order was not the only property affected; for

example, the surface area of the amorphous form was much lower, and it also had a reduced conjugation length. Nonetheless, in this specific example at least, the ordered COF form showed far superior function to its amorphous analogue. Stability is another consideration: when the first few CMPs and COFs were reported,<sup>12,25,39,41</sup> CMPs were much more stable materials because of the labile boronate ester bonding used in the COFs. This picture, too, has evolved, and there are now a number of “ultrastable” COFs using other bonding chemistries; we highlight here the important work of Banerjee.<sup>207–211</sup>

Given our sulfone COF example, above, it is tempting to gravitate toward ordered COFs over amorphous CMPs because they offer the alluring prospect of positioning atoms exactly where we want them to be. In turn, this suggests the potential for a priori, in silico design of function; this is particularly appealing in terms of introducing “designer” optoelectronic properties into these frameworks. While this is undoubtedly an exciting prospect, which our group and others are following, the current reality is more nuanced. First, many properties of interest, such as electronic gap, are expensive to calculate for periodic crystalline systems. Second, electronic properties may depend on the subtleties of crystal packing, such as the precise alignment of the  $\pi$  systems in the COF layers, and inferring from a modest-quality X-ray powder diffraction that a COF exhibits AA layer packing might not, in itself, be enough to deduce the precise charge transport properties. Third, it is still challenging to synthesize specific frameworks to order, and issues such as framework interpenetration or polymorphism can confound the bottom up design of these materials. Here, the “mix and match” nature of CMPs has much to offer, and the amorphous nature of these materials can be a benefit. To give a specific example in photocatalysis: we produced a library of 15 CMPs with different ratios of comonomers and found that one, CP-CMP10, showed a maximum H<sub>2</sub> evolution rate (Table 3; Figure 31).<sup>52</sup> This approach would have been difficult if not impossible in the case of COFs: while there are some examples of “multivariate MOFs” with more than one organic linker,<sup>212</sup> there are fewer examples of multilinker COFs. Also, for those crystalline solids, it is necessary to use linkers that all have the same dimensions in order to maintain an isorecticular structure, which was not the case with the pyrene/benzene linkers used in our CMP study. As such, amorphous CMPs allow a cocktail of monomers to be used to dial-in precise functions, and this allows large libraries to be produced, not only for CMPs but also for linear conjugated polymer photocatalysts.<sup>213</sup> Another example is the blending of monomers to achieve white light emission in CMPs.<sup>135</sup> Such monomer blending strategies could equally apply to CMP photoorganocatalysis in the future, for example, to achieve a particular reaction specificity. This in turn raises the question of how we should best deal with the inherent complexity in such multicomponent systems; one solution is to use robotic screening approaches<sup>213</sup> and directed evolution strategies, perhaps coupled with emerging selection methods such as inverse molecular design using machine learning.<sup>214</sup>

Given these considerations, we select four research directions where we can see particular promise and specific benefits for further CMP research:

#### 4.1. Photoorganocatalysis/Organocatalysis

While there are now several examples of CMP photoredox catalysis (section 3.4), and a rapidly expanding range of CMP photocatalysts for hydrogen evolution (section 3.9), we feel that this area is still underexploited, especially for synthetic organic transformations. Most photoredox catalysts are homogeneous and use rare transition metals.<sup>215</sup> The development of microporous, semiconducting polymers as heterogeneous photoredox catalysis offers a number of advantages, most obviously by reducing the use of expensive metals and simplifying catalyst recovery and reuse. Here, learnings from the area of photocatalytic hydrogen production (section 3.9), for example in terms of maximizing visible light absorption, should be directly transferable. The modular nature of CMPs also makes it quite straightforward to introduce chirality and (if needed) metal cocatalysts.<sup>45</sup> Because CMPs are not crystalline, this releases a design constraint encountered for COFs, and it may be possible to design (or to discover) multicomponent catalysts, for example, to carry out multistep cascade reactions, with a level of complexity that may be hard to replicate in crystalline COFs. This area is a natural “marriage” for CMPs since it necessarily combines light absorption and semiconductivity (conjugation) with surface area and mass transport (porosity).

#### 4.2. Heterojunction Semiconductor Composites

The area of polymer organic photovoltaics (OPV) is based around composite materials, often with fullerenes or their derivatives.<sup>216–218</sup> Surprisingly, there has been rather little overlap between CMP research and OPV research, although many of the design considerations are close to those in photoredox catalysis (section 3.4) and photocatalysis (section 3.9). One obvious constraint is solubility; with few exceptions,<sup>47,50,219</sup> most CMPs are insoluble and cannot be directly cast as thin films, which is fundamental to the preparation of large area OPV devices. Still, there are a number of untapped opportunities here. The micropores in many CMPs fall in the size range that should allow efficient fullerene absorption, although few studies exploit this so far.<sup>117,119,220,221</sup> (There are more studies with COFs, although not all of those frameworks are conjugated.<sup>222–228</sup>) This offers opportunities to create more effective CMP photocatalysts by introducing heterojunctions to promote charge separation. Also, while insoluble CMPs might not themselves be suitable for the formation of large-area OPV devices, the ability to form CMP nanoparticles<sup>138,151,229</sup> or to form dispersible, exfoliable materials<sup>187,230–232</sup> means that they could in principle be used as additives in OPV inks to improve performance.

#### 4.3. Batteries and Energy Storage

One limitation to the use of CMPs for energy storage (e.g., batteries and supercapacitors, section 3.7) is that CMPs tend to have poor bulk conductivity. As a result, it is usually necessary to use a relatively large quantity of an additive, such as carbon. This means that even CMP materials with inherently high charge storage capacities might lead to a device where the overall storage capacity is more modest. The development of highly porous, functionalized CMPs with much better electrical conductivity is therefore a promising line of research. The recent reports on sp<sup>2</sup> carbon-based COFs<sup>54,197,233,234</sup> might generate new avenues here.

#### 4.4. CMP Biohybrids

There have been exciting developments recently in materials that fuse inorganic semiconductor catalysts with biological organisms to create functional biohybrids,<sup>235,236</sup> for example, for solar-driven carbon dioxide fixation.<sup>237–239</sup> Since CMP materials can also exhibit photoredox activity (sections 3.4 and 3.9), there is scope to make analogous CMP biohybrids. This is currently an unexplored area, but there are several potential benefits in addition to the inherent modularity and synthetic breadth of CMP materials. For example, it is possible that biological organisms will be more biocompatible with organic CMPs, although we note that some CMPs show antibacterial activity (section 3.8.4). It is also possible that microporosity as well as monomer structure could modulate the adherence of bacteria to the CMP surface, as well as allowing efficient mass transport (e.g., ion transport) between the biological species and the organic semiconductor.

#### ASSOCIATED CONTENT

##### Supporting Information

The Supporting Information is available free of charge at <https://pubs.acs.org/doi/10.1021/acs.chemrev.9b00399>.

Full list of CMP-specific papers that cite back to key classic CMP studies used in Figure 2 (PDF)

#### AUTHOR INFORMATION

##### Corresponding Author

**Andrew I. Cooper** – Department of Chemistry and Materials Innovation Factory, University of Liverpool, Liverpool, United Kingdom; [orcid.org/0000-0003-0201-1021](https://orcid.org/0000-0003-0201-1021); Email: [aicooper@liverpool.ac.uk](mailto:aicooper@liverpool.ac.uk)

##### Author

**Jet-Sing M. Lee** – Department of Chemistry and Materials Innovation Factory, University of Liverpool, Liverpool, United Kingdom; [orcid.org/0000-0002-6740-8700](https://orcid.org/0000-0002-6740-8700)

Complete contact information is available at: <https://pubs.acs.org/doi/10.1021/acs.chemrev.9b00399>

##### Notes

The authors declare no competing financial interest.

##### Biographies

Jet-Sing M. Lee was born in the UK and obtained a first-class M. Chem degree (2013) at the University of Liverpool, which included a research year in industry (Ineos). He received his Ph.D. (2018) at the same university under the supervision of Prof. Andrew I. Cooper, FRS. His work focused on developing functional carbonaceous materials from porous organic polymers. During the final year of his Ph.D., he simultaneously undertook a JSPS Research Fellow at Kyoto University, Japan, with Prof. Susumu Kitagawa. Afterward, he worked as a research assistant professor there for a year. He is currently a JSPS Postdoctoral Research Fellow at The University of Tokyo in the group of Prof. Takuzo Aida. His research interests include porous frameworks, carbons, stimuli-responsive materials, and energy and environmental applications.

Andrew I. Cooper is a Nottingham graduate (1991), obtaining his Ph.D. there in 1994 with Prof. Martyn Poliakoff, FRS. After his Ph.D., he held a 1851 Fellowship and a Royal Society NATO Fellowship at the University of North Carolina at Chapel Hill, USA, working with Prof. Joseph M. DeSimone (1995–1997). He then held a Ramsay

Memorial Research Fellowship at the Melville Laboratory for Polymer Synthesis in Cambridge, working with Prof. Andrew B. Holmes, FRS (1997–1999). He joined Liverpool in 1999, initially as a Royal Society University Research Fellow. He is the Academic Director of the Materials Innovation Factory and the Director of the Leverhulme Research Centre for Functional Materials Design. He was made a Fellow of the Royal Society in 2015 and was recently awarded the 2019 Royal Society Hughes Medal. In addition to CMPs, his research interests include functional materials design, in particular the fusion of a priori structure–function predictions with experiment. He also has a programme in autonomous, mobile robots for materials discovery.

#### ACKNOWLEDGMENTS

We acknowledge funding from the Engineering and Physical Sciences Research Council (EPSRC) (Grant EP/N004884/1) and the Leverhulme Trust (Leverhulme Research Centre for Functional Materials Design). We also thank colleagues who have contributed to our CMP research over the years, including J.-X. Jiang, B. Tan, C. D. Wood, N. Campbell, Y. Z. Khimyak, R. Dawson, F. Su, A. Trewin, A. Laybourn, J. T. A. Jones, T. Hasell, D. J. Adams, R. Clowes, J. Xiao, S. J. Higgins, G. Cheng, B. Bonillo Fernandez, R. S. Sprick, S. Ren, T. Ratvijitvech, M. A. Zwijnenburg, P. Guignon, K. E. Jelfs, J. R. Durrant, M. Sachs, F. Blanc, N. Brownbill, B. J. Slater, T. O. McDonald, M. E. Briggs, and X. Wu.

#### REFERENCES

- (1) Thommes, M.; Kaneko, K.; Neimark, A. V.; Olivier, J. P.; Rodriguez-Reinoso, F.; Rouquerol, J.; Sing, K. S.W. Physisorption of Gases, with Special Reference to the Evaluation of Surface Area and Pore Size Distribution (IUPAC Technical Report). *Pure Appl. Chem.* **2015**, *87*, 1051.
- (2) Kondo, M.; Yoshitomi, T.; Matsuzaka, H.; Kitagawa, S.; Seki, K. Three-Dimensional Framework with Channeling Cavities for Small Molecules: {[M<sub>2</sub>(4, 4'-bpy)<sub>3</sub>(NO<sub>3</sub>)<sub>4</sub>]·XH<sub>2</sub>O}<sub>n</sub> (M = Co, Ni, Zn). *Angew. Chem., Int. Ed. Engl.* **1997**, *36*, 1725–1727.
- (3) Long, J. R.; Yaghi, O. M. The Pervasive Chemistry of Metal-Organic Frameworks. *Chem. Soc. Rev.* **2009**, *38*, 1213–1214.
- (4) O'Keeffe, M. Design of MOFs and Intellectual Content in Reticular Chemistry: A Personal View. *Chem. Soc. Rev.* **2009**, *38*, 1215–1217.
- (5) Furukawa, H.; Cordova, K. E.; O'Keeffe, M.; Yaghi, O. M. The Chemistry and Applications of Metal-Organic Frameworks. *Science* **2013**, *341*, 1230444.
- (6) Holst, J. R.; Trewin, A.; Cooper, A. I. Porous Organic Molecules. *Nat. Chem.* **2010**, *2*, 915–920.
- (7) Jones, J. T. A.; Hasell, T.; Wu, X.; Bacsá, J.; Jelfs, K. E.; Schmidtman, M.; Chong, S. Y.; Adams, D. J.; Trewin, A.; Schiffrman, F.; et al. Modular and Predictable Assembly of Porous Organic Molecular Crystals. *Nature* **2011**, *474*, 367–371.
- (8) Hasell, T.; Cooper, A. I. Porous Organic Cages: Soluble, Modular and Molecular Pores. *Nat. Rev. Mater.* **2016**, *1*, 16053.
- (9) Budd, P. M.; Ghanem, B. S.; Makhseed, S.; McKeown, N. B.; Msayib, K. J.; Tattershall, C. E. Polymers of Intrinsic Microporosity (PIMs): Robust, Solution-Processable, Organic Nanoporous Materials. *Chem. Commun.* **2004**, *0*, 230–231.
- (10) McKeown, N. B.; Budd, P. M. Polymers of Intrinsic Microporosity (PIMs): Organic Materials for Membrane Separations, Heterogeneous Catalysis and Hydrogen Storage. *Chem. Soc. Rev.* **2006**, *35*, 675–683.
- (11) McKeown, N. B.; Budd, P. M. Exploitation of Intrinsic Microporosity in Polymer-Based Materials. *Macromolecules* **2010**, *43*, 5163–5176.
- (12) Côté, A. P.; Benin, A. I.; Ockwig, N. W.; Keffe, M.; Matzger, A. J.; Yaghi, O. M. Porous, Crystalline, Covalent Organic Frameworks. *Science* **2005**, *310*, 1166–1170.



- (13) Ding, S.-Y.; Wang, W. Covalent Organic Frameworks (COFs): From Design to Applications. *Chem. Soc. Rev.* **2013**, *42*, 548–568.
- (14) Huang, N.; Wang, P.; Jiang, D. Covalent Organic Frameworks: A Materials Platform for Structural and Functional Designs. *Nat. Rev. Mater.* **2016**, *1*, 16068.
- (15) Tsyurupa, M. P.; Davankov, V. A. Porous Structure of Hypercrosslinked Polystyrene: State-of-the-Art Mini-Review. *React. Funct. Polym.* **2006**, *66*, 768–779.
- (16) Lee, J.-Y.; Wood, C. D.; Bradshaw, D.; Rosseinsky, M. J.; Cooper, A. I. Hydrogen Adsorption in Microporous Hypercrosslinked Polymers. *Chem. Commun.* **2006**, 2670–2672.
- (17) Wood, C. D.; Tan, B.; Trewin, A.; Niu, H.; Bradshaw, D.; Rosseinsky, M. J.; Khimyak, Y. Z.; Campbell, N. L.; Kirk, R.; Stöckel, E.; et al. Hydrogen Storage in Microporous Hypercrosslinked Organic Polymer Networks. *Chem. Mater.* **2007**, *19*, 2034–2048.
- (18) Tan, L.; Tan, B. Hypercrosslinked Porous Polymer Materials: Design, Synthesis, and Applications. *Chem. Soc. Rev.* **2017**, *46*, 3322–3356.
- (19) Kuhn, P.; Antonietti, M.; Thomas, A. Porous, Covalent Triazine-Based Frameworks Prepared by Ionothermal Synthesis. *Angew. Chem., Int. Ed.* **2008**, *47*, 3450–3453.
- (20) Ren, S.; Bojdys, M. J.; Dawson, R.; Laybourn, A.; Khimyak, Y. Z.; Adams, D. J.; Cooper, A. I. Porous, Fluorescent, Covalent Triazine-Based Frameworks Via Room-Temperature and Microwave-Assisted Synthesis. *Adv. Mater.* **2012**, *24*, 2357–2361.
- (21) Katekomol, P.; Roeser, J.; Bojdys, M.; Weber, J.; Thomas, A. Covalent Triazine Frameworks Prepared from 1,3,5-Tricyanobenzene. *Chem. Mater.* **2013**, *25*, 1542–1548.
- (22) Ben, T.; Ren, H.; Ma, S.; Cao, D.; Lan, J.; Jing, X.; Wang, W.; Xu, J.; Deng, F.; Simmons, J. M.; et al. Targeted Synthesis of a Porous Aromatic Framework with High Stability and Exceptionally High Surface Area. *Angew. Chem., Int. Ed.* **2009**, *48*, 9457–9460.
- (23) Ben, T.; Qiu, S. Porous Aromatic Frameworks: Synthesis, Structure and Functions. *CrystEngComm* **2013**, *15*, 17–26.
- (24) Konstas, K.; Taylor, J. W.; Thornton, A. W.; Doherty, C. M.; Lim, W. X.; Bastow, T. J.; Kennedy, D. F.; Wood, C. D.; Cox, B. J.; Hill, J. M.; et al. Lithiated Porous Aromatic Frameworks with Exceptional Gas Storage Capacity. *Angew. Chem., Int. Ed.* **2012**, *51*, 6639–6642.
- (25) Jiang, J.-X.; Su, F.; Trewin, A.; Wood, C. D.; Campbell, N. L.; Niu, H.; Dickinson, C.; Ganin, A. Y.; Rosseinsky, M. J.; Khimyak, Y. Z.; et al. Conjugated Microporous Poly(Aryleneethynylene) Networks. *Angew. Chem., Int. Ed.* **2007**, *46*, 8574–8578.
- (26) Cooper, A. I. Conjugated Microporous Polymers. *Adv. Mater.* **2009**, *21*, 1291–1295.
- (27) Xu, Y.; Jin, S.; Xu, H.; Nagai, A.; Jiang, D. Conjugated Microporous Polymers: Design, Synthesis and Application. *Chem. Soc. Rev.* **2013**, *42*, 8012–8031.
- (28) Xu, S.; Luo, Y.; Tan, B. Recent Development of Hypercrosslinked Microporous Organic Polymers. *Macromol. Rapid Commun.* **2013**, *34*, 471–484.
- (29) Lu, W.; Yuan, D.; Zhao, D.; Schilling, C. I.; Plietzsch, O.; Müller, T.; Bräse, S.; Guenther, J.; Blümel, J.; Krishna, R.; et al. Porous Polymer Networks: Synthesis, Porosity, and Applications in Gas Storage/Separation. *Chem. Mater.* **2010**, *22*, 5964–5972.
- (30) Rose, M.; Bohlmann, W.; Sabo, M.; Kaskel, S. Element-Organic Frameworks with High Permanent Porosity. *Chem. Commun.* **2008**, 2462–2464.
- (31) Rogozhin, S. V.; Davankov, V. A.; Tsyurupa, M. P. Patent USSR 299165, 1969.
- (32) Patterson, J. A. Preparation of Crosslinked Polystyrene and Their Derivatives for Use as Solid Support or Insoluble Reagents. In *Biochemical Aspects of Reaction on Solid Supports*; Academic Press: New York, 1971.
- (33) Davankov, V. A.; Rogozhin, S. V.; Tsyurupa, M. P. Macronet Isoporous Gels through Crosslinking of Dissolved Polystyrene. *J. Polym. Sci., Polym. Symp.* **1974**, *47*, 95–101.
- (34) Davankov, V. A.; Ilyin, M. M.; Tsyurupa, M. P.; Timofeeva, G. I.; Dubrovina, L. V. From a Dissolved Polystyrene Coil to an Intramolecularly-Hypercrosslinked “Nanosponge”. *Macromolecules* **1996**, *29*, 8398–8403.
- (35) Joseph, R.; Ford, W. T.; Zhang, S.; Tsyurupa, M. P.; Pastukhov, A. V.; Davankov, V. A. Solid-State <sup>13</sup>C-Nmr Analysis of Hypercrosslinked Polystyrene. *J. Polym. Sci., Part A: Polym. Chem.* **1997**, *35*, 695–701.
- (36) Davankov, V. A.; Tsyurupa, M. P. Structure and Properties of Hypercrosslinked Polystyrene—the First Representative of a New Class of Polymer Networks. *React. Polym.* **1990**, *13*, 27–42.
- (37) Wang, S.; Zhang, C.; Shu, Y.; Jiang, S.; Xia, Q.; Chen, L.; Jin, S.; Hussain, I.; Cooper, A. I.; Tan, B. Layered Microporous Polymers by Solvent Knitting Method. *Sci. Adv.* **2017**, *3*, No. e1602610.
- (38) Webster, O. W.; Gentry, F. P.; Farlee, R. D.; Smart, B. E. Hypercrosslinked Rigid-Rod Polymers. *Makromol. Chem., Macromol. Symp.* **1992**, *54–55*, 477–482.
- (39) El-Kaderi, H. M.; Hunt, J. R.; Mendoza-Cortes, J. L.; Cote, A. P.; Taylor, R. E.; O’Keeffe, M.; Yaghi, O. M. Designed Synthesis of 3d Covalent Organic Frameworks. *Science* **2007**, *316*, 268–272.
- (40) Jiang, J.-X.; Su, F.; Niu, H.; Wood, C. D.; Campbell, N. L.; Khimyak, Y. Z.; Cooper, A. I. Conjugated Microporous Poly-(Phenylene Butadiynylene)s. *Chem. Commun.* **2008**, 486–488.
- (41) Weber, J.; Thomas, A. Toward Stable Interfaces in Conjugated Polymers: Microporous Poly(P-Phenylene) and Poly-(Phenyleneethynylene) Based on a Spirobifluorene Building Block. *J. Am. Chem. Soc.* **2008**, *130*, 6334–6335.
- (42) Chen, L.; Honsho, Y.; Seki, S.; Jiang, D. Light-Harvesting Conjugated Microporous Polymers: Rapid and Highly Efficient Flow of Light Energy with a Porous Polyphenylene Framework as Antenna. *J. Am. Chem. Soc.* **2010**, *132*, 6742–6748.
- (43) Chen, L.; Yang, Y.; Jiang, D. Cmps as Scaffolds for Constructing Porous Catalytic Frameworks: A Built-in Heterogeneous Catalyst with High Activity and Selectivity Based on Nanoporous Metalloporphyrin Polymers. *J. Am. Chem. Soc.* **2010**, *132*, 9138–9143.
- (44) Jiang, J.-X.; Trewin, A.; Adams, D. J.; Cooper, A. I. Band Gap Engineering in Fluorescent Conjugated Microporous Polymers. *Chem. Sci.* **2011**, *2*, 1777–1781.
- (45) Jiang, J.-X.; Wang, C.; Laybourn, A.; Hasell, T.; Clowes, R.; Khimyak, Y. Z.; Xiao, J.; Higgins, S. J.; Adams, D. J.; Cooper, A. I. Metal–Organic Conjugated Microporous Polymers. *Angew. Chem., Int. Ed.* **2011**, *50*, 1072–1075.
- (46) Kou, Y.; Xu, Y.; Guo, Z.; Jiang, D. Supercapacitive Energy Storage and Electric Power Supply Using an Aza-Fused II-Conjugated Microporous Framework. *Angew. Chem., Int. Ed.* **2011**, *50*, 8753–8757.
- (47) Cheng, G.; Hasell, T.; Trewin, A.; Adams, D. J.; Cooper, A. I. Soluble Conjugated Microporous Polymers. *Angew. Chem., Int. Ed.* **2012**, *51*, 12727–12731.
- (48) Liu, X.; Xu, Y.; Jiang, D. Conjugated Microporous Polymers as Molecular Sensing Devices: Microporous Architecture Enables Rapid Response and Enhances Sensitivity in Fluorescence-On and Fluorescence-Off Sensing. *J. Am. Chem. Soc.* **2012**, *134*, 8738–8741.
- (49) Xu, Y.; Nagai, A.; Jiang, D. Core-Shell Conjugated Microporous Polymers: A New Strategy for Exploring Color-Tunable and -Controllable Light Emissions. *Chem. Commun.* **2013**, *49*, 1591–1593.
- (50) Cheng, G.; Bonillo, B.; Sprick, R. S.; Adams, D. J.; Hasell, T.; Cooper, A. I. Conjugated Polymers of Intrinsic Microporosity (C-PIMs). *Adv. Funct. Mater.* **2014**, *24*, 5219–5224.
- (51) Xu, F.; Chen, X.; Tang, Z.; Wu, D.; Fu, R.; Jiang, D. Redox-Active Conjugated Microporous Polymers: A New Organic Platform for Highly Efficient Energy Storage. *Chem. Commun.* **2014**, *50*, 4788–4790.
- (52) Sprick, R. S.; Jiang, J.-X.; Bonillo, B.; Ren, S.; Ratvijitvech, T.; Guiglion, P.; Zwijnenburg, M. A.; Adams, D. J.; Cooper, A. I. Tunable Organic Photocatalysts for Visible-Light-Driven Hydrogen Evolution. *J. Am. Chem. Soc.* **2015**, *137*, 3265–3270.
- (53) Wang, L.; Wan, Y.; Ding, Y.; Wu, S.; Zhang, Y.; Zhang, X.; Zhang, G.; Xiong, Y.; Wu, X.; Yang, J.; et al. Conjugated Microporous

Polymer Nanosheets for Overall Water Splitting Using Visible Light. *Adv. Mater.* **2017**, *29*, 1702428.

(54) Jin, E.; Asada, M.; Xu, Q.; Dalapati, S.; Addicoat, M. A.; Brady, M. A.; Xu, H.; Nakamura, T.; Heine, T.; Chen, Q.; et al. Two-Dimensional  $sp^2$  Carbon-Conjugated Covalent Organic Frameworks. *Science* **2017**, *357*, 673–676.

(55) Liang, B.; Wang, H.; Shi, X.; Shen, B.; He, X.; Ghazi, Z. A.; Khan, N. A.; Sin, H.; Khattak, A. M.; Li, L.; et al. Microporous Membranes Comprising Conjugated Polymers with Rigid Backbones Enable Ultrafast Organic-Solvent Nanofiltration. *Nat. Chem.* **2018**, *10*, 961–967.

(56) Chen, J.; Yan, W.; Townsend, E. J.; Feng, J.; Pan, L.; Del Angel Hernandez, V.; Faul, C. F. J. Tunable Surface Area, Porosity, and Function in Conjugated Microporous Polymers. *Angew. Chem., Int. Ed.* **2019**, *58*, 11715–11719.

(57) Farha, O. K.; Özgür Yazaydın, A.; Eryazici, I.; Malliakas, C. D.; Hauser, B. G.; Kanatzidis, M. G.; Nguyen, S. T.; Snurr, R. Q.; Hupp, J. T. De Novo Synthesis of a Metal–Organic Framework Material Featuring Ultrahigh Surface Area and Gas Storage Capacities. *Nat. Chem.* **2010**, *2*, 944–948.

(58) Farha, O. K.; Eryazici, I.; Jeong, N. C.; Hauser, B. G.; Wilmer, C. E.; Sarjeant, A. A.; Snurr, R. Q.; Nguyen, S. T.; Yazaydın, A. Ö.; Hupp, J. T. Metal–Organic Framework Materials with Ultrahigh Surface Areas: Is the Sky the Limit? *J. Am. Chem. Soc.* **2012**, *134*, 15016–15021.

(59) Yuan, D.; Zhao, D.; Sun, D.; Zhou, H.-C. An Isoreticular Series of Metal–Organic Frameworks with Dendritic Hexacarboxylate Ligands and Exceptionally High Gas-Uptake Capacity. *Angew. Chem., Int. Ed.* **2010**, *49*, 5357–5361.

(60) Jiang, J.-X.; Su, F.; Trewin, A.; Wood, C. D.; Niu, H.; Jones, J. T. A.; Khimyak, Y. Z.; Cooper, A. I. Synthetic Control of the Pore Dimension and Surface Area in Conjugated Microporous Polymer and Copolymer Networks. *J. Am. Chem. Soc.* **2008**, *130*, 7710–7720.

(61) Trewin, A.; Cooper, A. I. Porous Organic Polymers: Distinction from Disorder? *Angew. Chem., Int. Ed.* **2010**, *49*, 1533–1535.

(62) Yuan, D.; Lu, W.; Zhao, D.; Zhou, H.-C. Highly Stable Porous Polymer Networks with Exceptionally High Gas-Uptake Capacities. *Adv. Mater.* **2011**, *23*, 3723–3725.

(63) Ren, S.; Dawson, R.; Adams, D. J.; Cooper, A. I. Low Band-Gap Benzothiadiazole Conjugated Microporous Polymers. *Polym. Chem.* **2013**, *4*, 5585–5590.

(64) Zwiijnenburg, M. A.; Cheng, G.; McDonald, T. O.; Jelfs, K. E.; Jiang, J.-X.; Ren, S.; Hasell, T.; Blanc, F.; Cooper, A. I.; Adams, D. J. Shedding Light on Structure–Property Relationships for Conjugated Microporous Polymers: The Importance of Rings and Strain. *Macromolecules* **2013**, *46*, 7696–7704.

(65) Yanagida, S.; Kabumoto, A.; Mizumoto, K.; Pac, C.; Yoshino, K. Poly(p-Phenylene)-Catalysed Photoreduction of Water to Hydrogen. *J. Chem. Soc., Chem. Commun.* **1985**, 474–475.

(66) Wang, X.; Maeda, K.; Thomas, A.; Takanabe, K.; Xin, G.; Carlsson, J. M.; Domen, K.; Antonietti, M. A Metal-Free Polymeric Photocatalyst for Hydrogen Production from Water under Visible Light. *Nat. Mater.* **2009**, *8*, 76–80.

(67) Jiang, J.-X.; Laybourn, A.; Clowes, R.; Khimyak, Y. Z.; Bacsa, J.; Higgins, S. J.; Adams, D. J.; Cooper, A. I. High Surface Area Contorted Conjugated Microporous Polymers Based on Spiro-Bipropylenedioxythiophene. *Macromolecules* **2010**, *43*, 7577–7582.

(68) Chen, Q.; Wang, J.-X.; Wang, Q.; Bian, N.; Li, Z.-H.; Yan, C.-G.; Han, B.-H. Spiro(Fluorene-9,9'-Xanthene)-Based Porous Organic Polymers: Preparation, Porosity, and Exceptional Hydrogen Uptake at Low Pressure. *Macromolecules* **2011**, *44*, 7987–7993.

(69) Kiskan, B.; Weber, J. Versatile Postmodification of Conjugated Microporous Polymers Using Thiol-Yne Chemistry. *ACS Macro Lett.* **2012**, *1*, 37–40.

(70) Ratvijitvech, T.; Dawson, R.; Laybourn, A.; Khimyak, Y. Z.; Adams, D. J.; Cooper, A. I. Post-Synthetic Modification of Conjugated Microporous Polymers. *Polymer* **2014**, *55*, 321–325.

(71) Doucet, H.; Hierso, J.-C. Palladium-Based Catalytic Systems for the Synthesis of Conjugated Enynes by Sonogashira Reactions and Related Alkynylations. *Angew. Chem., Int. Ed.* **2007**, *46*, 834–871.

(72) Trunk, M.; Herrmann, A.; Bildirir, H.; Yassin, A.; Schmidt, J.; Thomas, A. Copper-Free Sonogashira Coupling for High-Surface-Area Conjugated Microporous Poly(Aryleneethynylene) Networks. *Chem. - Eur. J.* **2016**, *22*, 7179–7183.

(73) Dawson, R.; Laybourn, A.; Khimyak, Y. Z.; Adams, D. J.; Cooper, A. I. High Surface Area Conjugated Microporous Polymers: The Importance of Reaction Solvent Choice. *Macromolecules* **2010**, *43*, 8524–8530.

(74) Thorand, S.; Krause, N. Improved Procedures for the Palladium-Catalyzed Coupling of Terminal Alkynes with Aryl Bromides (Sonogashira Coupling). *J. Org. Chem.* **1998**, *63*, 8551–8553.

(75) Miyaura, N.; Yamada, K.; Suzuki, A. A New Stereospecific Cross-Coupling by the Palladium-Catalyzed Reaction of 1-Alkenylboranes with 1-Alkenyl or 1-Alkynyl Halides. *Tetrahedron Lett.* **1979**, *20*, 3437–3440.

(76) Miyaura, N.; Suzuki, A. Stereoselective Synthesis of Arylated (E)-Alkenes by the Reaction of Alk-1-Enylboranes with Aryl Halides in the Presence of Palladium Catalyst. *J. Chem. Soc., Chem. Commun.* **1979**, 866–867.

(77) Liu, Q.; Tang, Z.; Wu, M.; Zhou, Z. Design, Preparation and Application of Conjugated Microporous Polymers. *Polym. Int.* **2014**, *63*, 381–392.

(78) Schmidt, J.; Werner, M.; Thomas, A. Conjugated Microporous Polymer Networks Via Yamamoto Polymerization. *Macromolecules* **2009**, *42*, 4426–4429.

(79) Sun, L.; Liang, Z.; Yu, J.; Xu, R. Luminescent Microporous Organic Polymers Containing the 1,3,5-Tri(4-Ethenylphenyl)Benzene Unit Constructed by Heck Coupling Reaction. *Polym. Chem.* **2013**, *4*, 1932–1938.

(80) Sun, L.; Zou, Y.; Liang, Z.; Yu, J.; Xu, R. A One-Pot Synthetic Strategy Via Tandem Suzuki-Heck Reactions for the Construction of Luminescent Microporous Organic Polymers. *Polym. Chem.* **2014**, *5*, 471–478.

(81) Yuan, S.; Dorney, B.; White, D.; Kirklın, S.; Zapol, P.; Yu, L.; Liu, D.-J. Microporous Polyphenylenes with Tunable Pore Size for Hydrogen Storage. *Chem. Commun.* **2010**, 46, 4547–4549.

(82) Hao, L.; Luo, B.; Li, X.; Jin, M.; Fang, Y.; Tang, Z.; Jia, Y.; Liang, M.; Thomas, A.; Yang, J.; et al. Terephthalonitrile-Derived Nitrogen-Rich Networks for High Performance Supercapacitors. *Energy Environ. Sci.* **2012**, *5*, 9747–9751.

(83) Wang, K.; Yang, L.-M.; Wang, X.; Guo, L.; Cheng, G.; Zhang, C.; Jin, S.; Tan, B.; Cooper, A. Covalent Triazine Frameworks Via a Low-Temperature Polycondensation Approach. *Angew. Chem., Int. Ed.* **2017**, *56*, 14149–14153.

(84) Yu, S.-Y.; Mahmood, J.; Noh, H.-J.; Seo, J.-M.; Jung, S.-M.; Shin, S.-H.; Im, Y.-K.; Jeon, I.-Y.; Baek, J.-B. Direct Synthesis of a Covalent Triazine-Based Framework from Aromatic Amides. *Angew. Chem., Int. Ed.* **2018**, *57*, 8438–8442.

(85) Buyukcakir, O.; Yuksel, R.; Jiang, Y.; Lee, S. H.; Seong, W. K.; Chen, X.; Ruoff, R. S. Synthesis of Porous Covalent Quinazoline Networks (CQNs) and Their Gas Sorption Properties. *Angew. Chem., Int. Ed.* **2019**, *58*, 872–876.

(86) Stille, J. K.; Mainen, E. Ladder Polyquinoxalines. *J. Polym. Sci., Part B: Polym. Lett.* **1966**, *4*, 39–41.

(87) Stille, J. K.; Mainen, E. L. Thermally Stable Ladder Polyquinoxalines. *Macromolecules* **1968**, *1*, 36–42.

(88) Marco, A. B.; Cortizo-Lacalle, D.; Perez-Miqueo, I.; Valenti, G.; Boni, A.; Plas, J.; Strutyński, K.; De Feyter, S.; Paolucci, F.; Montes, M.; et al. Twisted Aromatic Frameworks: Readily Exfoliable and Solution-Processable Two-Dimensional Conjugated Microporous Polymers. *Angew. Chem., Int. Ed.* **2017**, *56*, 6946–6951.

(89) Pandey, P.; Katsoulidis, A. P.; Eryazici, I.; Wu, Y.; Kanatzidis, M. G.; Nguyen, S. T. Imine-Linked Microporous Polymer Organic Frameworks. *Chem. Mater.* **2010**, *22*, 4974–4979.



- (90) Rabbani, M. G.; Sekizkardes, A. K.; El-Kadri, O. M.; Kaafarani, B. R.; El-Kaderi, H. M. Pyrene-Directed Growth of Nanoporous Benzimidazole-Linked Nanofibers and Their Application to Selective CO<sub>2</sub> Capture and Separation. *J. Mater. Chem.* **2012**, *22*, 25409–25417.
- (91) Xu, C.; Hedin, N. Synthesis of Microporous Organic Polymers with High CO<sub>2</sub>-over-N<sub>2</sub> Selectivity and CO<sub>2</sub> Adsorption. *J. Mater. Chem. A* **2013**, *1*, 3406–3414.
- (92) Rabbani, M. G.; El-Kaderi, H. M. Template-Free Synthesis of a Highly Porous Benzimidazole-Linked Polymer for CO<sub>2</sub> Capture and H<sub>2</sub> Storage. *Chem. Mater.* **2011**, *23*, 1650–1653.
- (93) Biswal, B. P.; Becker, D.; Chandrasekhar, N.; Seenath, J. S.; Paasch, S.; Machill, S.; Hennersdorf, F.; Brunner, E.; Weigand, J. J.; Berger, R.; et al. Exploration of Thiazolo[5,4-D]Thiazole Linkages in Conjugated Porous Organic Polymers for Chemoselective Molecular Sieving. *Chem. - Eur. J.* **2018**, *24*, 10868–10875.
- (94) Zhu, X.; Tian, C.; Jin, T.; Wang, J.; Mahurin, S. M.; Mei, W.; Xiong, Y.; Hu, J.; Feng, X.; Liu, H.; et al. Thiazolothiazole-Linked Porous Organic Polymers. *Chem. Commun.* **2014**, *50*, 15055–15058.
- (95) Pennella, F.; Banks, R. L.; Bailey, G. C. Disproportionation of Alkynes. *Chem. Commun.* **1968**, 1548–1549.
- (96) Lu, G.; Yang, H.; Zhu, Y.; Huggins, T.; Ren, Z. J.; Liu, Z.; Zhang, W. Synthesis of a Conjugated Porous Co(II) Porphyrinylene-Ethynylene Framework through Alkyne Metathesis and Its Catalytic Activity Study. *J. Mater. Chem. A* **2015**, *3*, 4954–4959.
- (97) Li, B.; Guan, Z.; Yang, X.; Wang, W. D.; Wang, W.; Hussain, I.; Song, K.; Tan, B.; Li, T. Multifunctional Microporous Organic Polymers. *J. Mater. Chem. A* **2014**, *2*, 11930–11939.
- (98) Zhang, Y.; A, S.; Zou, Y.; Luo, X.; Li, Z.; Xia, H.; Liu, X.; Mu, Y. Gas Uptake, Molecular Sensing and Organocatalytic Performances of a Multifunctional Carbazole-Based Conjugated Microporous Polymer. *J. Mater. Chem. A* **2014**, *2*, 13422–13430.
- (99) Vingiello, F. A.; Yanez, J.; Campbell, J. A. New Approach to the Synthesis of Dibenzo[*a,l*] Pyrenes. *J. Org. Chem.* **1971**, *36*, 2053–2056.
- (100) Liao, Y.; Wang, H.; Zhu, M.; Thomas, A. Efficient Supercapacitor Energy Storage Using Conjugated Microporous Polymer Networks Synthesized from Buchwald–Hartwig Coupling. *Adv. Mater.* **2018**, *30*, 1705710.
- (101) Liao, Y.; Weber, J.; Faul, C. F. J. Conjugated Microporous Polytriphenylamine Networks. *Chem. Commun.* **2014**, *50*, 8002–8005.
- (102) Gu, C.; Chen, Y.; Zhang, Z.; Xue, S.; Sun, S.; Zhang, K.; Zhong, C.; Zhang, H.; Pan, Y.; Lv, Y.; et al. Electrochemical Route to Fabricate Film-Like Conjugated Microporous Polymers and Application for Organic Electronics. *Adv. Mater.* **2013**, *25*, 3443–3448.
- (103) Gu, C.; Huang, N.; Gao, J.; Xu, F.; Xu, Y.; Jiang, D. Controlled Synthesis of Conjugated Microporous Polymer Films: Versatile Platforms for Highly Sensitive and Label-Free Chemo- and Biosensing. *Angew. Chem., Int. Ed.* **2014**, *53*, 4850–4855.
- (104) Zhang, H.; Zhang, Y.; Gu, C.; Ma, Y. Electropolymerized Conjugated Microporous Poly(Zinc-Porphyrin) Films as Potential Electrode Materials in Supercapacitors. *Adv. Energy Mater.* **2015**, *5*, 1402175.
- (105) Gu, C.; Huang, N.; Chen, Y.; Qin, L.; Xu, H.; Zhang, S.; Li, F.; Ma, Y.; Jiang, D.  $\Pi$ -Conjugated Microporous Polymer Films: Designed Synthesis, Conducting Properties, and Photoenergy Conversions. *Angew. Chem., Int. Ed.* **2015**, *54*, 13594–13598.
- (106) Germain, J.; Frechet, J. M. J.; Svec, F. Hypercrosslinked Polyanilines with Nanoporous Structure and High Surface Area: Potential Adsorbents for Hydrogen Storage. *J. Mater. Chem.* **2007**, *17*, 4989–4997.
- (107) Germain, J.; Frechet, J. M. J.; Svec, F. Nanoporous, Hypercrosslinked Polypyrroles: Effect of Crosslinking Moiety on Pore Size and Selective Gas Adsorption. *Chem. Commun.* **2009**, 1526–1528.
- (108) Zhang, W.; Li, C.; Yuan, Y.-P.; Qiu, L.-G.; Xie, A.-J.; Shen, Y.-H.; Zhu, J.-F. Highly Energy- and Time-Efficient Synthesis of Porous Triazine-Based Framework: Microwave-Enhanced Ionothermal Polymerization and Hydrogen Uptake. *J. Mater. Chem.* **2010**, *20*, 6413–6415.
- (109) Peng, Y.; Huang, M.; Hu, Y.; Li, G.; Xia, L. Microwave-Assisted Synthesis of Porphyrin Conjugated Microporous Polymers for Microextraction of Volatile Organic Acids in Tobaccos. *J. Chromatogr., A* **2019**, *1594*, 45–53.
- (110) Chai, S.; Hu, N.; Han, Y.; Zhang, X.; Yang, Z.; Wei, L.; Wang, L.; Wei, H. The Microwave-Assisted Solvothermal Synthesis of a Novel B-Ketoenamine-Linked Conjugated Microporous Polymer for Supercapacitors. *RSC Adv.* **2016**, *6*, 49425–49428.
- (111) Troschke, E.; Grätz, S.; Lübken, T.; Borchardt, L. Mechanochemical Friedel–Crafts Alkylation—A Sustainable Pathway Towards Porous Organic Polymers. *Angew. Chem., Int. Ed.* **2017**, *56*, 6859–6863.
- (112) Yuan, K.; Guo-Wang, P.; Hu, T.; Shi, L.; Zeng, R.; Forster, M.; Pichler, T.; Chen, Y.; Scherf, U. Nanofibrous and Graphene-Templated Conjugated Microporous Polymer Materials for Flexible Chemosensors and Supercapacitors. *Chem. Mater.* **2015**, *27*, 7403–7411.
- (113) Zhao, Y.; Yao, K. X.; Teng, B.; Zhang, T.; Han, Y. A Perfluorinated Covalent Triazine-Based Framework for Highly Selective and Water-Tolerant CO<sub>2</sub> Capture. *Energy Environ. Sci.* **2013**, *6*, 3684–3692.
- (114) Lindemann, P.; Tsotsalas, M.; Shishatskiy, S.; Abetz, V.; Krolla-Sidenstein, P.; Azucena, C.; Monnereau, L.; Beyer, A.; Götzhäuser, A.; Mugnaini, V.; et al. Preparation of Freestanding Conjugated Microporous Polymer Nanomembranes for Gas Separation. *Chem. Mater.* **2014**, *26*, 7189–7193.
- (115) Talapaneni, S. N.; Kim, D.; Barin, G.; Buyukcakir, O.; Je, S. H.; Coskun, A. Pillar[5]Arene Based Conjugated Microporous Polymers for Propane/Methane Separation through Host–Guest Complexation. *Chem. Mater.* **2016**, *28*, 4460–4466.
- (116) Dawson, R.; Laybourn, A.; Clowes, R.; Khimyak, Y. Z.; Adams, D. J.; Cooper, A. I. Functionalized Conjugated Microporous Polymers. *Macromolecules* **2009**, *42*, 8809–8816.
- (117) Rao, K. V.; Mohapatra, S.; Maji, T. K.; George, S. J. Guest-Responsive Reversible Swelling and Enhanced Fluorescence in a Super-Absorbent, Dynamic Microporous Polymer. *Chem. - Eur. J.* **2012**, *18*, 4505–4509.
- (118) Wang, X.-S.; Liu, J.; Bonefont, J. M.; Yuan, D.-Q.; Thallapally, P. K.; Ma, S. A Porous Covalent Porphyrin Framework with Exceptional Uptake Capacity of Saturated Hydrocarbons for Oil Spill Cleanup. *Chem. Commun.* **2013**, *49*, 1533–1535.
- (119) Venkata Rao, K.; Haldar, R.; Maji, T. K.; George, S. J. Dynamic, Conjugated Microporous Polymers: Visible Light Harvesting Via Guest-Responsive Reversible Swelling. *Phys. Chem. Chem. Phys.* **2016**, *18*, 156–163.
- (120) Xie, Y.; Wang, T.-T.; Liu, X.-H.; Zou, K.; Deng, W.-Q. Capture and Conversion of CO<sub>2</sub> at Ambient Conditions by a Conjugated Microporous Polymer. *Nat. Commun.* **2013**, *4*, 1960.
- (121) Wu, Z.-S.; Chen, L.; Liu, J.; Parvez, K.; Liang, H.; Shu, J.; Sachdev, H.; Graf, R.; Feng, X.; Müllen, K. High-Performance Electrocatalysts for Oxygen Reduction Derived from Cobalt Porphyrin-Based Conjugated Mesoporous Polymers. *Adv. Mater.* **2014**, *26*, 1450–1455.
- (122) Cui, S.; Qian, M.; Liu, X.; Sun, Z.; Du, P. A Copper Porphyrin-Based Conjugated Mesoporous Polymer-Derived Bifunctional Electrocatalyst for Hydrogen and Oxygen Evolution. *ChemSusChem* **2016**, *9*, 2365–2373.
- (123) He, Y.; Gehrig, D.; Zhang, F.; Lu, C.; Zhang, C.; Cai, M.; Wang, Y.; Laquai, F.; Zhuang, X.; Feng, X. Highly Efficient Electrocatalysts for Oxygen Reduction Reaction Based on 1d Ternary Doped Porous Carbons Derived from Carbon Nanotube Directed Conjugated Microporous Polymers. *Adv. Funct. Mater.* **2016**, *26*, 8255–8265.
- (124) Jiang, J.-X.; Li, Y.; Wu, X.; Xiao, J.; Adams, D. J.; Cooper, A. I. Conjugated Microporous Polymers with Rose Bengal Dye for Highly Efficient Heterogeneous Organo-Photocatalysis. *Macromolecules* **2013**, *46*, 8779–8783.

- (125) Kang, N.; Park, J. H.; Ko, K. C.; Chun, J.; Kim, E.; Shin, H.-W.; Lee, S. M.; Kim, H. J.; Ahn, T. K.; Lee, J. Y.; et al. Tandem Synthesis of Photoactive Benzodifuran Moieties in the Formation of Microporous Organic Networks. *Angew. Chem., Int. Ed.* **2013**, *52*, 6228–6232.
- (126) Zhang, K.; Kopetzki, D.; Seeberger, P. H.; Antonietti, M.; Vilela, F. Surface Area Control and Photocatalytic Activity of Conjugated Microporous Poly(Benzothiadiazole) Networks. *Angew. Chem., Int. Ed.* **2013**, *52*, 1432–1436.
- (127) Wang, Z. J.; Ghasimi, S.; Landfester, K.; Zhang, K. A. I. Highly Porous Conjugated Polymers for Selective Oxidation of Organic Sulfides under Visible Light. *Chem. Commun.* **2014**, *50*, 8177–8180.
- (128) Wang, Z. J.; Ghasimi, S.; Landfester, K.; Zhang, K. A. I. Photocatalytic Suzuki Coupling Reaction Using Conjugated Microporous Polymer with Immobilized Palladium Nanoparticles under Visible Light. *Chem. Mater.* **2015**, *27*, 1921–1924.
- (129) Liras, M.; Iglesias, M.; Sánchez, F. Conjugated Microporous Polymers Incorporating Bodipy Moieties as Light-Emitting Materials and Recyclable Visible-Light Photocatalysts. *Macromolecules* **2016**, *49*, 1666–1673.
- (130) Wang, Z. J.; Ghasimi, S.; Landfester, K.; Zhang, K. A. I. Bandgap Engineering of Conjugated Nanoporous Poly-Benzobisthiadiazoles Via Copolymerization for Enhanced Photocatalytic 1,2,3,4-Tetrahydroquinoline Synthesis under Visible Light. *Adv. Synth. Catal.* **2016**, *358*, 2576–2582.
- (131) Wang, C.-A.; Li, Y.-W.; Cheng, X.-L.; Zhang, J.-P.; Han, Y.-F. Eosin Y Dye-Based Porous Organic Polymers for Highly Efficient Heterogeneous Photocatalytic Dehydrogenative Coupling Reaction. *RSC Adv.* **2017**, *7*, 408–414.
- (132) Xu, Y.; Chen, L.; Guo, Z.; Nagai, A.; Jiang, D. Light-Emitting Conjugated Polymers with Microporous Network Architecture: Interweaving Scaffold Promotes Electronic Conjugation, Facilitates Exciton Migration, and Improves Luminescence. *J. Am. Chem. Soc.* **2011**, *133*, 17622–17625.
- (133) Liu, X.; Zhang, Y.; Li, H.; A, S.; Xia, H.; Mu, Y. Triarylboron-Based Fluorescent Conjugated Microporous Polymers. *RSC Adv.* **2013**, *3*, 21267–21270.
- (134) Zhang, P.; Wu, K.; Guo, J.; Wang, C. From Hyperbranched Polymer to Nanoscale CMP (NCMP): Improved Microscopic Porosity, Enhanced Light Harvesting, and Enabled Solution Processing into White-Emitting Dye@Ncmp Films. *ACS Macro Lett.* **2014**, *3*, 1139–1144.
- (135) Bonillo, B.; Sprick, R. S.; Cooper, A. I. Tuning Photophysical Properties in Conjugated Microporous Polymers by Comonomer Doping Strategies. *Chem. Mater.* **2016**, *28*, 3469–3480.
- (136) Novotney, J. L.; Dichtel, W. R. Conjugated Porous Polymers for TNT Vapor Detection. *ACS Macro Lett.* **2013**, *2*, 423–426.
- (137) Li, Z.; Li, H.; Xia, H.; Ding, X.; Luo, X.; Liu, X.; Mu, Y. Triarylboron-Linked Conjugated Microporous Polymers: Sensing and Removal of Fluoride Ions. *Chem. - Eur. J.* **2015**, *21*, 17355–17362.
- (138) Geng, T.-M.; Zhu, H.; Song, W.; Zhu, F.; Wang, Y. Conjugated Microporous Polymer-Based Carbazole Derivatives as Fluorescence Chemosensors for Picric Acid. *J. Mater. Sci.* **2016**, *51*, 4104–4114.
- (139) Zhuang, X.; Zhang, F.; Wu, D.; Forler, N.; Liang, H.; Wagner, M.; Gehrig, D.; Hansen, M. R.; Laquai, F.; Feng, X. Two-Dimensional Sandwich-Type, Graphene-Based Conjugated Microporous Polymers. *Angew. Chem., Int. Ed.* **2013**, *52*, 9668–9672.
- (140) Zhang, Q.; Ge, S.; Wang, X.; Sun, H.; Zhu, Z.; Liang, W.; Li, A. Novel MnO/Conjugated Microporous Polymer Derived-Porous Hard Carbon Nanocomposite for Superior Lithium Storage. *RSC Adv.* **2014**, *4*, 41649–41653.
- (141) Zhang, S.; Huang, W.; Hu, P.; Huang, C.; Shang, C.; Zhang, C.; Yang, R.; Cui, G. Conjugated Microporous Polymers with Excellent Electrochemical Performance for Lithium and Sodium Storage. *J. Mater. Chem. A* **2015**, *3*, 1896–1901.
- (142) Chai, S.; Hu, N.; Han, Y.; Zhang, X.; Yang, Z.; Wei, L.; Wang, L.; Wei, H. The Microwave-Assisted Solvothermal Synthesis of a Novel [Small Beta]-Ketoenamine-Linked Conjugated Microporous Polymer for Supercapacitors. *RSC Adv.* **2016**, *6*, 49425–49428.
- (143) Lee, J.-S. M.; Wu, T.-H.; Alston, B. M.; Briggs, M. E.; Hasell, T.; Hu, C.-C.; Cooper, A. I. Porosity-Engineered Carbons for Supercapacitive Energy Storage Using Conjugated Microporous Polymer Precursors. *J. Mater. Chem. A* **2016**, *4*, 7665–7673.
- (144) Zhang, Q.; Dai, Q.; Li, M.; Wang, X.; Li, A. Incorporation of MnO Nanoparticles inside Porous Carbon Nanotubes Originated from Conjugated Microporous Polymers for Lithium Storage. *J. Mater. Chem. A* **2016**, *4*, 19132–19139.
- (145) Li, X.-C.; Zhang, Y.; Wang, C.-Y.; Wan, Y.; Lai, W.-Y.; Pang, H.; Huang, W. Redox-Active Triazatruxene-Based Conjugated Microporous Polymers for High-Performance Supercapacitors. *Chem. Sci.* **2017**, *8*, 2959–2965.
- (146) Zhang, C.; He, Y.; Mu, P.; Wang, X.; He, Q.; Chen, Y.; Zeng, J.; Wang, F.; Xu, Y.; Jiang, J.-X. Toward High Performance Thiophene-Containing Conjugated Microporous Polymer Anodes for Lithium-Ion Batteries through Structure Design. *Adv. Funct. Mater.* **2018**, *28*, 1705432.
- (147) Bhunia, S.; Dey, N.; Pradhan, A.; Bhattacharya, S. A Conjugated Microporous Polymer Based Visual Sensing Platform for Aminoglycoside Antibiotics in Water. *Chem. Commun.* **2018**, *54*, 7495–7498.
- (148) Rengaraj, A.; Puthiaraj, P.; Haldorai, Y.; Heo, N. S.; Hwang, S.-K.; Han, Y.-K.; Kwon, S.; Ahn, W.-S.; Huh, Y. S. Porous Covalent Triazine Polymer as a Potential Nanocargo for Cancer Therapy and Imaging. *ACS Appl. Mater. Interfaces* **2016**, *8*, 8947–8955.
- (149) Hynek, J.; Rathouský, J.; Demel, J.; Lang, K. Design of Porphyrin-Based Conjugated Microporous Polymers with Enhanced Singlet Oxygen Productivity. *RSC Adv.* **2016**, *6*, 44279–44287.
- (150) Ding, X.; Han, B.-H. Metallophthalocyanine-Based Conjugated Microporous Polymers as Highly Efficient Photosensitizers for Singlet Oxygen Generation. *Angew. Chem., Int. Ed.* **2015**, *54*, 6536–6539.
- (151) Ma, B. C.; Ghasimi, S.; Landfester, K.; Zhang, K. A. I. Enhanced Visible Light Promoted Antibacterial Efficiency of Conjugated Microporous Polymer Nanoparticles Via Molecular Doping. *J. Mater. Chem. B* **2016**, *4*, 5112–5118.
- (152) Li, Z.; Feng, X.; Gao, S.; Jin, Y.; Zhao, W.; Liu, H.; Yang, X.; Hu, S.; Cheng, K.; Zhang, J. Porous Organic Polymer-Coated Band-Aids for Phototherapy of Bacteria-Induced Wound Infection. *ACS Applied Bio Materials* **2019**, *2*, 613–618.
- (153) Tan, J.; Wan, J.; Guo, J.; Wang, C. Self-Sacrificial Template-Induced Modulation of Conjugated Microporous Polymer Microcapsules and Shape-Dependent Enhanced Photothermal Efficiency for Ablation of Cancer Cells. *Chem. Commun.* **2015**, *51*, 17394–17397.
- (154) Vyas, V. S.; Haase, F.; Stegbauer, L.; Savasci, G.; Podjaski, F.; Ochsenfeld, C.; Lotsch, B. V. A Tunable Azine Covalent Organic Framework Platform for Visible Light-Induced Hydrogen Generation. *Nat. Commun.* **2015**, *6*, 8508.
- (155) Bhunia, A.; Esquivel, D.; Dey, S.; Fernandez-Teran, R.; Goto, Y.; Inagaki, S.; Van Der Voort, P.; Janiak, C. A Photoluminescent Covalent Triazine Framework: CO<sub>2</sub> Adsorption, Light-Driven Hydrogen Evolution and Sensing of Nitroaromatics. *J. Mater. Chem. A* **2016**, *4*, 13450–13457.
- (156) Li, L.; Cai, Z.; Wu, Q.; Lo, W.-Y.; Zhang, N.; Chen, L. X.; Yu, L. Rational Design of Porous Conjugated Polymers and Roles of Residual Palladium for Photocatalytic Hydrogen Production. *J. Am. Chem. Soc.* **2016**, *138*, 7681–7686.
- (157) Li, L.; Lo, W.-y.; Cai, Z.; Zhang, N.; Yu, L. Donor–Acceptor Porous Conjugated Polymers for Photocatalytic Hydrogen Production: The Importance of Acceptor Comonomer. *Macromolecules* **2016**, *49*, 6903–6909.
- (158) Sprick, R. S.; Bonillo, B.; Sachs, M.; Clowes, R.; Durrant, J. R.; Adams, D. J.; Cooper, A. I. Extended Conjugated Microporous Polymers for Photocatalytic Hydrogen Evolution from Water. *Chem. Commun.* **2016**, *52*, 10008–10011.
- (159) Yang, C.; Ma, B. C.; Zhang, L.; Lin, S.; Ghasimi, S.; Landfester, K.; Zhang, K. A. I.; Wang, X. Molecular Engineering of



Conjugated Polybenzothiadiazoles for Enhanced Hydrogen Production by Photosynthesis. *Angew. Chem., Int. Ed.* **2016**, *55*, 9202–9206.

(160) Sprick, R. S.; Bai, Y.; Guilbert, A. A. Y.; Zbiri, M.; Aitchison, C. M.; Wilbraham, L.; Yan, Y.; Woods, D. J.; Zwijnenburg, M. A.; Cooper, A. I. Photocatalytic Hydrogen Evolution from Water Using Fluorene and Dibenzothiophene Sulfone Conjugated Microporous and Linear Polymers. *Chem. Mater.* **2019**, *31*, 305–313.

(161) Dawson, R.; Cooper, A. I.; Adams, D. J. Nanoporous Organic Polymer Networks. *Prog. Polym. Sci.* **2012**, *37*, 530–563.

(162) Dawson, R.; Stockel, E.; Holst, J. R.; Adams, D. J.; Cooper, A. I. Microporous Organic Polymers for Carbon Dioxide Capture. *Energy Environ. Sci.* **2011**, *4*, 4239–4245.

(163) Dawson, R.; Adams, D. J.; Cooper, A. I. Chemical Tuning of CO<sub>2</sub> Sorption in Robust Nanoporous Organic Polymers. *Chem. Sci.* **2011**, *2*, 1173–1177.

(164) Chen, L.; Yang, Y.; Guo, Z.; Jiang, D. Highly Efficient Activation of Molecular Oxygen with Nanoporous Metalloporphyrin Frameworks in Heterogeneous Systems. *Adv. Mater.* **2011**, *23*, 3149–3154.

(165) Li, H.; Tang, P.; Zhao, Y.; Liu, S.-X.; Aeschi, Y.; Deng, L.; Braun, J.; Zhao, B.; Liu, Y.; Tan, S.; et al. Benzodifuran-Containing Well-Defined  $\Pi$ -Conjugated Polymers for Photovoltaic Cells. *J. Polym. Sci., Part A: Polym. Chem.* **2012**, *50*, 2935–2943.

(166) Huang, W.; Ma, B. C.; Lu, H.; Li, R.; Wang, L.; Landfester, K.; Zhang, K. A. I. Visible-Light-Promoted Selective Oxidation of Alcohols Using a Covalent Triazine Framework. *ACS Catal.* **2017**, *7*, 5438–5442.

(167) Huang, W.; Byun, J.; Rörich, I.; Ramanan, C.; Blom, P. W. M.; Lu, H.; Wang, D.; Caire da Silva, L.; Li, R.; Wang, L.; et al. Asymmetric Covalent Triazine Framework for Enhanced Visible-Light Photoredox Catalysis Via Energy Transfer Cascade. *Angew. Chem., Int. Ed.* **2018**, *57*, 8316–8320.

(168) Hudson, Z. M.; Wang, S. Impact of Donor–Acceptor Geometry and Metal Chelation on Photophysical Properties and Applications of Triarylboranes. *Acc. Chem. Res.* **2009**, *42*, 1584–1596.

(169) Hu, C.-C.; Wang, C.-C. Effects of Electrolytes and Electrochemical Pretreatments on the Capacitive Characteristics of Activated Carbon Fabrics for Supercapacitors. *J. Power Sources* **2004**, *125*, 299–308.

(170) Li, Z.; Yang, Y.-W. Creation and Bioapplications of Porous Organic Polymer Materials. *J. Mater. Chem. B* **2017**, *5*, 9278–9290.

(171) Zhang, H.; Li, G.; Liao, C.; Cai, Y.; Jiang, G. Bio-Related Applications of Porous Organic Frameworks (Pofs). *J. Mater. Chem. B* **2019**, *7*, 2398–2420.

(172) Kudo, A.; Miseki, Y. Heterogeneous Photocatalyst Materials for Water Splitting. *Chem. Soc. Rev.* **2009**, *38*, 253–278.

(173) Chen, X.; Shen, S.; Guo, L.; Mao, S. S. Semiconductor-Based Photocatalytic Hydrogen Generation. *Chem. Rev.* **2010**, *110*, 6503–6570.

(174) Wang, X.; Maeda, K.; Thomas, A.; Takanabe, K.; Xin, G.; Carlsson, J. M.; Domen, K.; Antonietti, M. A Metal-Free Polymeric Photocatalyst for Hydrogen Production from Water under Visible Light. *Nat. Mater.* **2009**, *8*, 76–80.

(175) Park, J. H.; Ko, K. C.; Park, N.; Shin, H.-W.; Kim, E.; Kang, N.; Hong, K. J.; Lee, S. M.; Kim, H. J.; Ahn, T. K.; et al. Microporous Organic Nanorods with Electronic Push-Pull Skeletons for Visible Light-Induced Hydrogen Evolution from Water. *J. Mater. Chem. A* **2014**, *2*, 7656–7661.

(176) Kosco, J.; Sachs, M.; Godin, R.; Kirkus, M.; Francas, L.; Bidwell, M.; Qureshi, M.; Anjum, D.; Durrant, J. R.; McCulloch, I. The Effect of Residual Palladium Catalyst Contamination on the Photocatalytic Hydrogen Evolution Activity of Conjugated Polymers. *Adv. Energy Mater.* **2018**, *8*, 1802181.

(177) Stegbauer, L.; Schwinghammer, K.; Lotsch, B. V. A Hydrazone-Based Covalent Organic Framework for Photocatalytic Hydrogen Production. *Chem. Sci.* **2014**, *5*, 2789–2793.

(178) Mothika, V. S.; Sutar, P.; Verma, P.; Das, S.; Pati, S. K.; Maji, T. K. Regulating Charge-Transfer in Conjugated Microporous

Polymers for Photocatalytic Hydrogen Evolution. *Chem. - Eur. J.* **2019**, *25*, 3867–3874.

(179) Meier, C. B.; Sprick, R. S.; Monti, A.; Guiglion, P.; Lee, J.-S. M.; Zwijnenburg, M. A.; Cooper, A. I. Structure-Property Relationships for Covalent Triazine-Based Frameworks: The Effect of Spacer Length on Photocatalytic Hydrogen Evolution from Water. *Polymer* **2017**, *126*, 283–290.

(180) Meier, C. B.; Clowes, R.; Berardo, E.; Jelfs, K. E.; Zwijnenburg, M. A.; Sprick, R. S.; Cooper, A. I. Structurally Diverse Covalent Triazine-Based Framework Materials for Photocatalytic Hydrogen Evolution from Water. *Chem. Mater.* **2019**, *31*, 8830–8838.

(181) Liu, M.; Huang, Q.; Wang, S.; Li, Z.; Li, B.; Jin, S.; Tan, B. Crystalline Covalent Triazine Frameworks by in Situ Oxidation of Alcohols to Aldehyde Monomers. *Angew. Chem., Int. Ed.* **2018**, *57*, 11968–11972.

(182) Huang, W.; He, Q.; Hu, Y.; Li, Y. Molecular Heterostructures of Covalent Triazine Frameworks for Enhanced Photocatalytic Hydrogen Production. *Angew. Chem., Int. Ed.* **2019**, *58*, 8676–8680.

(183) Wang, Z.; Yang, X.; Yang, T.; Zhao, Y.; Wang, F.; Chen, Y.; Zeng, J. H.; Yan, C.; Huang, F.; Jiang, J.-X. Dibenzothiophene Dioxide Based Conjugated Microporous Polymers for Visible-Light-Driven Hydrogen Production. *ACS Catal.* **2018**, *8*, 8590–8596.

(184) Goto, Y.; Hisatomi, T.; Wang, Q.; Higashi, T.; Ishikiriya, K.; Maeda, T.; Sakata, Y.; Okunaka, S.; Tokudome, H.; Katayama, M.; et al. A Particulate Photocatalyst Water-Splitting Panel for Large-Scale Solar Hydrogen Generation. *Joule* **2018**, *2*, 509–520.

(185) Sprick, R. S.; Bonillo, B.; Clowes, R.; Guiglion, P.; Brownbill, N. J.; Slater, B. J.; Blanc, F.; Zwijnenburg, M. A.; Adams, D. J.; Cooper, A. I. Visible-Light-Driven Hydrogen Evolution Using Planarized Conjugated Polymer Photocatalysts. *Angew. Chem., Int. Ed.* **2016**, *55*, 1792–1796.

(186) Xiang, Y.; Wang, X.; Rao, L.; Wang, P.; Huang, D.; Ding, X.; Zhang, X.; Wang, S.; Chen, H.; Zhu, Y. Conjugated Polymers with Sequential Fluorination for Enhanced Photocatalytic H<sub>2</sub> Evolution Via Proton-Coupled Electron Transfer. *ACS Energy Lett.* **2018**, *3*, 2544–2549.

(187) Wang, X.; Chen, L.; Chong, S. Y.; Little, M. A.; Wu, Y.; Zhu, W.-H.; Clowes, R.; Yan, Y.; Zwijnenburg, M. A.; Sprick, R. S.; et al. Sulfone-Containing Covalent Organic Frameworks for Photocatalytic Hydrogen Evolution from Water. *Nat. Chem.* **2018**, *10*, 1180–1189.

(188) Giri, N.; Del Pópolo, M. G.; Melaugh, G.; Greenaway, R. L.; Rätzke, K.; Koschine, T.; Pison, L.; Gomes, M. F. C.; Cooper, A. I.; James, S. L. Liquids with Permanent Porosity. *Nature* **2015**, *527*, 216.

(189) Slater, A. G.; Cooper, A. I. Function-Led Design of New Porous Materials. *Science* **2015**, *348*, aaa8075.

(190) Dalapati, S.; Jin, S.; Gao, J.; Xu, Y.; Nagai, A.; Jiang, D. An Azine-Linked Covalent Organic Framework. *J. Am. Chem. Soc.* **2013**, *135*, 17310–17313.

(191) Banerjee, T.; Gottschling, K.; Savasci, G.; Ochsenfeld, C.; Lotsch, B. V. H<sub>2</sub> Evolution with Covalent Organic Framework Photocatalysts. *ACS Energy Lett.* **2018**, *3*, 400–409.

(192) Babu, H. V.; Bai, M. G. M.; Rajeswara Rao, M. Functional  $\Pi$ -Conjugated Two-Dimensional Covalent Organic Frameworks. *ACS Appl. Mater. Interfaces* **2019**, *11*, 11029–11060.

(193) Ding, S.-Y.; Gao, J.; Wang, Q.; Zhang, Y.; Song, W.-G.; Su, C.-Y.; Wang, W. Construction of Covalent Organic Framework for Catalysis: Pd/COF-LZU1 in Suzuki–Miyaura Coupling Reaction. *J. Am. Chem. Soc.* **2011**, *133*, 19816–19822.

(194) Rao, M. R.; Fang, Y.; De Feyter, S.; Perepichka, D. F. Conjugated Covalent Organic Frameworks Via Michael Addition–Elimination. *J. Am. Chem. Soc.* **2017**, *139*, 2421–2427.

(195) Meng, Z.; Aykanat, A.; Mirica, K. A. Proton Conduction in 2d Aza-Fused Covalent Organic Frameworks. *Chem. Mater.* **2019**, *31*, 819–825.

(196) Guo, J.; Xu, Y.; Jin, S.; Chen, L.; Kaji, T.; Honsho, Y.; Addicoat, M. A.; Kim, J.; Saeki, A.; Ihee, H.; et al. Conjugated Organic Framework with Three-Dimensionally Ordered Stable Structure and Delocalized  $\Pi$  Clouds. *Nat. Commun.* **2013**, *4*, 2736.

- (197) Zhao, Y.; Liu, H.; Wu, C.; Zhang, Z.; Pan, Q.; Hu, F.; Wang, R.; Li, P.; Huang, X.; Li, Z. Fully Conjugated Two-Dimensional  $sp^2$ -Carbon Covalent Organic Frameworks as Artificial Photosystem I with High Efficiency. *Angew. Chem., Int. Ed.* **2019**, *58*, 5376–5381.
- (198) Jin, E.; Li, J.; Geng, K.; Jiang, Q.; Xu, H.; Xu, Q.; Jiang, D. Designed Synthesis of Stable Light-Emitting Two-Dimensional  $sp^2$  Carbon-Conjugated Covalent Organic Frameworks. *Nat. Commun.* **2018**, *9*, 4143.
- (199) Sick, T.; Hufnagel, A. G.; Kampmann, J.; Kondofersky, I.; Calik, M.; Rotter, J. M.; Evans, A.; Döblinger, M.; Herbert, S.; Peters, K.; et al. Oriented Films of Conjugated 2d Covalent Organic Frameworks as Photocathodes for Water Splitting. *J. Am. Chem. Soc.* **2018**, *140*, 2085–2092.
- (200) Albacete, P.; Martínez, J. I.; Li, X.; López-Moreno, A.; Mena-Hernando, S. a.; Platero-Prats, A. E.; Montoro, C.; Loh, K. P.; Pérez, E. M.; Zamora, F. Layer-Stacking-Driven Fluorescence in a Two-Dimensional Imine-Linked Covalent Organic Framework. *J. Am. Chem. Soc.* **2018**, *140*, 12922–12929.
- (201) Albacete, P.; López-Moreno, A.; Mena-Hernando, S.; Platero-Prats, A. E.; Pérez, E. M.; Zamora, F. Chemical Sensing of Water Contaminants by a Colloid of a Fluorescent Imine-Linked Covalent Organic Framework. *Chem. Commun.* **2019**, *55*, 1382–1385.
- (202) Beaudoin, D.; Maris, T.; Wuest, J. D. Constructing Monocrystalline Covalent Organic Networks by Polymerization. *Nat. Chem.* **2013**, *5*, 830–834.
- (203) Zhang, Y.-B.; Su, J.; Furukawa, H.; Yun, Y.; Gándara, F.; Duong, A.; Zou, X.; Yaghi, O. M. Single-Crystal Structure of a Covalent Organic Framework. *J. Am. Chem. Soc.* **2013**, *135*, 16336–16339.
- (204) Li, H.; Chavez, A. D.; Li, H.; Li, H.; Dichtel, W. R.; Bredas, J.-L. Nucleation and Growth of Covalent Organic Frameworks from Solution: The Example of COF-5. *J. Am. Chem. Soc.* **2017**, *139*, 16310–16318.
- (205) Evans, A. M.; Parent, L. R.; Flanders, N. C.; Bisbey, R. P.; Vitaku, E.; Kirschner, M. S.; Schaller, R. D.; Chen, L. X.; Gianneschi, N. C.; Dichtel, W. R. Seeded Growth of Single-Crystal Two-Dimensional Covalent Organic Frameworks. *Science* **2018**, *361*, 52–57.
- (206) Evans, A. M.; Castano, I.; Brumberg, A.; Parent, L. R.; Corcos, A. R.; Li, R. L.; Flanders, N. C.; Gosztola, D. J.; Gianneschi, N. C.; Schaller, R. D.; et al. Emissive Single-Crystalline Boroxine-Linked Colloidal Covalent Organic Frameworks. *J. Am. Chem. Soc.* **2019**, *141*, 19728–19735.
- (207) Chandra, S.; Kandambeth, S.; Biswal, B. P.; Lukose, B.; Kunjir, S. M.; Chaudhary, M.; Babarao, R.; Heine, T.; Banerjee, R. Chemically Stable Multilayered Covalent Organic Nanosheets from Covalent Organic Frameworks Via Mechanical Delamination. *J. Am. Chem. Soc.* **2013**, *135*, 17853–17861.
- (208) Biswal, B. P.; Kandambeth, S.; Chandra, S.; Shinde, D. B.; Bera, S.; Karak, S.; Garai, B.; Kharul, U. K.; Banerjee, R. Pore Surface Engineering in Porous, Chemically Stable Covalent Organic Frameworks for Water Adsorption. *J. Mater. Chem. A* **2015**, *3*, 23664–23669.
- (209) Halder, A.; Karak, S.; Addicoat, M.; Bera, S.; Chakraborty, A.; Kunjattu, S. H.; Pachfule, P.; Heine, T.; Banerjee, R. Ultrastable Imine-Based Covalent Organic Frameworks for Sulfuric Acid Recovery: An Effect of Interlayer Hydrogen Bonding. *Angew. Chem., Int. Ed.* **2018**, *57*, 5797–5802.
- (210) Wei, P.-F.; Qi, M.-Z.; Wang, Z.-P.; Ding, S.-Y.; Yu, W.; Liu, Q.; Wang, L.-K.; Wang, H.-Z.; An, W.-K.; Wang, W. Benzoxazole-Linked Ultrastable Covalent Organic Frameworks for Photocatalysis. *J. Am. Chem. Soc.* **2018**, *140*, 4623–4631.
- (211) Guan, X.; Li, H.; Ma, Y.; Xue, M.; Fang, Q.; Yan, Y.; Valtchev, V.; Qiu, S. Chemically Stable Polyarylether-Based Covalent Organic Frameworks. *Nat. Chem.* **2019**, *11*, 587.
- (212) Deng, H.; Doonan, C. J.; Furukawa, H.; Ferreira, R. B.; Towne, J.; Knobler, C. B.; Wang, B.; Yaghi, O. M. Multiple Functional Groups of Varying Ratios in Metal-Organic Frameworks. *Science* **2010**, *327*, 846–850.
- (213) Bai, Y.; Wilbraham, L.; Slater, B. J.; Zwijnenburg, M. A.; Sprick, R. S.; Cooper, A. I. Accelerated Discovery of Organic Polymer Photocatalysts for Hydrogen Evolution from Water through the Integration of Experiment and Theory. *J. Am. Chem. Soc.* **2019**, *141*, 9063–9071.
- (214) Sanchez-Lengeling, B.; Aspuru-Guzik, A. Inverse Molecular Design Using Machine Learning: Generative Models for Matter Engineering. *Science* **2018**, *361*, 360–365.
- (215) Prier, C. K.; Rankic, D. A.; MacMillan, D. W. C. Visible Light Photoredox Catalysis with Transition Metal Complexes: Applications in Organic Synthesis. *Chem. Rev.* **2013**, *113*, 5322–5363.
- (216) Brabec, C. J.; Gowrisanker, S.; Halls, J. J. M.; Laird, D.; Jia, S.; Williams, S. P. Polymer–Fullerene Bulk-Heterojunction Solar Cells. *Adv. Mater.* **2010**, *22*, 3839–3856.
- (217) Chen, J.; Cao, Y. Development of Novel Conjugated Donor Polymers for High-Efficiency Bulk-Heterojunction Photovoltaic Devices. *Acc. Chem. Res.* **2009**, *42*, 1709–1718.
- (218) Yip, H.-L.; Jen, A. K. Y. Recent Advances in Solution-Processed Interfacial Materials for Efficient and Stable Polymer Solar Cells. *Energy Environ. Sci.* **2012**, *5*, 5994–6011.
- (219) Huang, B.; Zhao, P.; Dai, Y.; Deng, S.; Hu, A. Size-Controlled Synthesis of Soluble-Conjugated Microporous Polymer Nanoparticles through Sonogashira Polycondensation in Confined Nanoreactors. *J. Polym. Sci., Part A: Polym. Chem.* **2016**, *54*, 2285–2290.
- (220) Xu, L.; Li, Y. Responsive Guest Encapsulation of Dynamic Conjugated Microporous Polymers. *Sci. Rep.* **2016**, *6*, 28784.
- (221) Gu, C.; Huang, N.; Chen, Y.; Qin, L.; Xu, H.; Zhang, S.; Li, F.; Ma, Y.; Jiang, D.  $\pi$ -Conjugated Microporous Polymer Films: Designed Synthesis, Conducting Properties, and Photoenergy Conversions. *Angew. Chem.* **2015**, *127*, 13798–13802.
- (222) Dogru, M.; Handloser, M.; Auras, F.; Kunz, T.; Medina, D.; Hartschuh, A.; Knochel, P.; Bein, T. A Photoconductive Thienothiophene-Based Covalent Organic Framework Showing Charge Transfer Towards Included Fullerene. *Angew. Chem., Int. Ed.* **2013**, *52*, 2920–2924.
- (223) Cui, D.; Ebrahimi, M.; Rosei, F.; Macleod, J. M. Control of Fullerene Crystallization from 2d to 3d through Combined Solvent and Template Effects. *J. Am. Chem. Soc.* **2017**, *139*, 16732–16740.
- (224) Bessinger, D.; Ascherl, L.; Auras, F.; Bein, T. Spectrally Switchable Photodetection with near-Infrared-Absorbing Covalent Organic Frameworks. *J. Am. Chem. Soc.* **2017**, *139*, 12035–12042.
- (225) Plas, J.; Ivasenko, O.; Martsinovich, N.; Lackinger, M.; De Feyter, S. Nanopatterning of a Covalent Organic Framework Host–Guest System. *Chem. Commun.* **2016**, *52*, 68–71.
- (226) Jin, S.; Supur, M.; Addicoat, M.; Furukawa, K.; Chen, L.; Nakamura, T.; Fukuzumi, S.; Irle, S.; Jiang, D. Creation of Superheterojunction Polymers Via Direct Polycondensation: Segregated and Bicontinuous Donor–Acceptor  $\pi$ -Columnar Arrays in Covalent Organic Frameworks for Long-Lived Charge Separation. *J. Am. Chem. Soc.* **2015**, *137*, 7817–7827.
- (227) Cui, D.; MacLeod, J. M.; Ebrahimi, M.; Perepichka, D. F.; Rosei, F. Solution and Air Stable Host/Guest Architectures from a Single Layer Covalent Organic Framework. *Chem. Commun.* **2015**, *51*, 16510–16513.
- (228) Medina, D. D.; Werner, V.; Auras, F.; Tautz, R.; Dogru, M.; Schuster, J.; Linke, S.; Döblinger, M.; Feldmann, J.; Knochel, P.; et al. Oriented Thin Films of a Benzodithiophene Covalent Organic Framework. *ACS Nano* **2014**, *8*, 4042–4052.
- (229) Ma, B. C.; Ghasimi, S.; Landfester, K.; Vilela, F.; Zhang, K. A. I. Conjugated Microporous Polymer Nanoparticles with Enhanced Dispersibility and Water Compatibility for Photocatalytic Applications. *J. Mater. Chem. A* **2015**, *3*, 16064–16071.
- (230) Marco, A. B.; Cortizo-Lacalle, D.; Perez-Miqueo, I.; Valenti, G.; Boni, A.; Plas, J.; Strutyński, K.; De Feyter, S.; Paolucci, F.; Montes, M.; et al. Twisted Aromatic Frameworks: Readily Exfoliable and Solution-Processable Two-Dimensional Conjugated Microporous Polymers. *Angew. Chem., Int. Ed.* **2017**, *56*, 6946–6951.
- (231) Zhu, Y.; Chen, X.; Cao, Y.; Peng, W.; Li, Y.; Zhang, G.; Zhang, F.; Fan, X. Reversible Intercalation and Exfoliation of Layered

Covalent Triazine Frameworks for Enhanced Lithium Ion Storage. *Chem. Commun.* **2019**, *55*, 1434–1437.

(232) Zhu, Y.; Qiao, M.; Peng, W.; Li, Y.; Zhang, G.; Zhang, F.; Li, Y.; Fan, X. Rapid Exfoliation of Layered Covalent Triazine-Based Frameworks into N-Doped Quantum Dots for the Selective Detection of Hg<sup>2+</sup> Ions. *J. Mater. Chem. A* **2017**, *5*, 9272–9278.

(233) Jin, E.; Lan, Z.; Jiang, Q.; Geng, K.; Li, G.; Wang, X.; Jiang, D. 2d sp<sup>2</sup> Carbon-Conjugated Covalent Organic Frameworks for Photocatalytic Hydrogen Production from Water. *Chem.* **2019**, *5*, 1632–1647.

(234) Fu, Z.; Wang, X.; Gardner, A.; Wang, X.; Chong, S. Y.; Neri, G.; Cowan, A. J.; Liu, L.; Li, X.; Vogel, A.; et al. A Stable Covalent Organic Framework for Photocatalytic Carbon Dioxide Reduction. *Chem. Sci.* **2020**, *11*, 543–550.

(235) Kornienko, N.; Zhang, J. Z.; Sakimoto, K. K.; Yang, P.; Reisner, E. Interfacing Nature's Catalytic Machinery with Synthetic Materials for Semi-Artificial Photosynthesis. *Nat. Nanotechnol.* **2018**, *13*, 890–899.

(236) Guo, J.; Suástegui, M.; Sakimoto, K. K.; Moody, V. M.; Xiao, G.; Nocera, D. G.; Joshi, N. S. Light-Driven Fine Chemical Production in Yeast Biohybrids. *Science* **2018**, *362*, 813–816.

(237) Cestellos-Blanco, S.; Zhang, H.; Yang, P. Solar-Driven Carbon Dioxide Fixation Using Photosynthetic Semiconductor Bio-Hybrids. *Faraday Discuss.* **2019**, *215*, 54–65.

(238) Zhang, H.; Liu, H.; Tian, Z.; Lu, D.; Yu, Y.; Cestellos-Blanco, S.; Sakimoto, K. K.; Yang, P. Bacteria Photosensitized by Intracellular Gold Nanoclusters for Solar Fuel Production. *Nat. Nanotechnol.* **2018**, *13*, 900–905.

(239) Sakimoto, K. K.; Wong, A. B.; Yang, P. Self-Photosensitization of Nonphotosynthetic Bacteria for Solar-to-Chemical Production. *Science* **2016**, *351*, 74–77.